Low-lying proton intruder state in ^{13}B *via* ^{4}He(^{12}Be,^{13}Bγ) reaction

Shinsuke OTA

January, 2009

ABSTRACT

The proton-single-particle state and proton intruder state in the neutron-rich unstable nucleus ^{13}B are studied by in-beam γ-ray spectroscopy with the proton transfer reaction (α, t) in inverse kinematics. The experiment has been performed at RIPS beam line in RIKEN. The secondary beam of ^{12}Be bombarded a liquid helium target with an incident energy of 50 MeV/nucleon. De-excitation γ rays were detected by a new detector array: Gamma-Ray detector Array with Position and Energy sensitivity (GRAPE). Several γ lines were observed corresponding to the transition from four excited states directly to the ground state. Angular differential cross sections have been deduced up to a scattering angle of 6 degrees in the laboratory frame and analyzed with the DWBA-analysis method. Deduced transferred angular momentum gives a spin and parity assignment of $1/2^+$ to the 4.83-MeV excited state and also possible assignments of the spins of the other excited states. The spectroscopic strength for 4.83-MeV state was deduced as $C^2S = 0.20 \pm 0.02(stat.) \pm 0.1(syst.)$.

The excitation energy, spin and parity, and spectroscopic strength of the 4.83-MeV excited state have been compared with a shell model calculation using SFO interaction, which includes the effect of the tensor force. Any predicted $1/2^+$ state is not consistent with our experimental results. The possible deformation of the nucleus is qualitatively examined based on the large deformation of the ^{12}Be core. The simple expression to the low-lying $1/2^+$ state at 4.83-MeV excitation energy is $(\pi[220]1/2)^1 \otimes ^{12}$Be. The deformation of the nucleus makes the [220]1/2 orbit lower and the whole system gains an energy of $\sim$8 MeV – including the change of the single particle energy and the surface energy in empirical mass formula, which explains the existence of the proton intruder state in ^{13}B. The present study suggests that nuclear deformation is important to the change of the proton shell structure in neutron-rich unstable nuclei.

Contents

List of Tables

List of Figures

Chapter 1

Introduction

1.1 Intruder state in light neutron-rich nuclei

A picture of the shell structure was originally applied to the atomic nuclei so as to explain the discrepancies in the systematics of the binding energies and relative abundances in 1934 by Elsasser [1]. The gross systematics itself was well explained by the liquid drop model; however, the discrepancies were seen when the proton number (Z) or neutron number (N) is 2, 8, 20, 28, 50, 82, or 126, which are now called '*magic number*'. The magic number corresponds to the number of filled nucleons of each type up to the closed shell, in contrast to the number of electrons in atomic closed shell. In order to reproduce the magic number, Mayer [2, 3, 4] and Jensen [5] introduced spin-orbit force into the nuclear shell structure in 1949. The shell model including the effect of spin-orbit force well represents not only the existence of the magic number but also the spins of the ground states, especially of odd-mass nuclei. The spin of a odd-mass nucleus is characterized by the last unpaired one nucleon since identical nucleons in a same orbit are paired to form the spin and parity of 0^+.

Nuclear deformation was introduced into shell structure [6] in 1953. In this picture the nuclear potential in an atomic nucleus is deformed and the resultant shell structure is different from the spherical one. This picture described the large quadruple moments and excitation energies in rare-metal isotopes. Figure 1.1 shows a Nilsson diagram for up to around $N(Z) \leq 50$. At the deformation parameter $\epsilon_2 = 0$, *i.e.* spherical limit, the magic numbers are seen. The positive and negative ϵ_2 values correspond to prolate and oblate deformations, respectively. When ϵ_2 value is non-zero, the degeneracies of the magnetic sub-states are resolved, and some orbits are pushed up while some others are pulled down.

This picture of spherical and deformed shell structure explains the properties of the ground and low-lying excited states in β-stable nuclei very well. However, the situation changed after the exploration of the properties of unstable nuclei far from the β-stability line. One of the most striking phenomena is the disappearance of the nuclear magic number in light neutron-rich nuclei. The magic number $N = 8$ disappears in light neutron-rich

unstable nuclei. The low excitation energies of low-lying 2^+_1 [7] and 0^+_2 [8, 9] states in ^{12}Be suggest a $2\hbar\omega$ configuration in these states. The large deformation of the ground state in ^{12}Be was also indicated by an AMD calculation [10]. Around the $N = 20$ region, an inversion of the orbits in *sd*-shell appears in many neutron-rich unstable nuclei in the so-called 'island of inversion' region [11, 12]. These disappearances of the magic numbers are believed to originate from the change of the single-particle orbits in a nuclear potential. In this situation, the low-lying excited states having many $\hbar\omega$ excitations (or configurations) appear and can account for the disappearance of the magic number.

An attractive phenomena associated with this change of the single-particle orbits is the existence of intruder states. Intruder states are characterized by the last nucleon in the intruder orbit, which comes down from upper shell. Since the parities of neighboring shells are opposite, the parities of the intruder states are atypical. The existence of intruder states in light neutron-rich unstable nuclei is often considered to be evidence for one or more $\hbar\omega$ configurations in the low-lying states around the *psd* shell. The ground state of ^{11}Be is $1/2^+$ which is lower in energy by 0.3 MeV than the $1/2^-$ state [13]. In ^{12}Be, there is a 1^- intruder state at 2.7-MeV excitation energy [14]. The energies of these low-lying, abnormal parity states indicate $1\hbar\omega$ configurations.

Three theoretical interpretations have been proposed for these one or more $\hbar\omega$ configurations in the low-lying states of neutron-rich unstable nuclei: (1) the monopole interaction of the tensor force [15, 16]; (2) the loosely bound nature of some orbitals [17]; (3) nuclear deformation [9, 18, 19]. In Ref. [15, 16], the effective interaction was determined so that the model reproduces the energy levels in light neutron-rich nuclei including intruder states, and the importance of monopole interaction due to the tensor force was pointed out. A schematic picture of monopole interaction is illustrated in Fig. 1.2. In this figure the monopole interaction is produced by the tensor force between a proton in $j_{>,<} = l \pm 1/2$ orbit and a neutron in $j'_{>,<} = l' \pm 1/2$ orbit. The tensor force between the $j_{>(<)}$ and $j'_{<(>)}$ is attractive; on the other hand, the one between $j_{>(<)}$ and $j'_{>(<)}$ is repulsive. The existence of less protons changes the energy of neutron orbital, and the neutron shell gap becomes small. Reference [17] discusses the fact that the $2s_{1/2}$ orbital gains its energy relative to the other orbitals in the *psd* shell due to its loosely bound nature. Figure 1.1 shows an example of the effect of this weakly bound nature. Near the zero binding energy, the $2s_{1/2}$ orbital becomes close to the $1p_{1/2}$ orbital and the gap between them becomes small. The non-zero $\hbar\omega$ configurations can also be intuitively explained by the deformed mean field picture. As seen in the Nilsson diagram (Fig. 1.1), the [220]1/2 orbit becomes rapidly lower, and the [101]1/2 becomes slightly higher, *i.e.* the gap becomes smaller with increasing deformation. Since these models provide the corresponding effects for the change of the neutron shell structure in neutron-rich unstable nuclei, such as ^{11,12}Be from the different point of view, the relative importance of three theory has not been clarified.

These effects are expected to change for the proton shell in light neutron-rich nuclei.

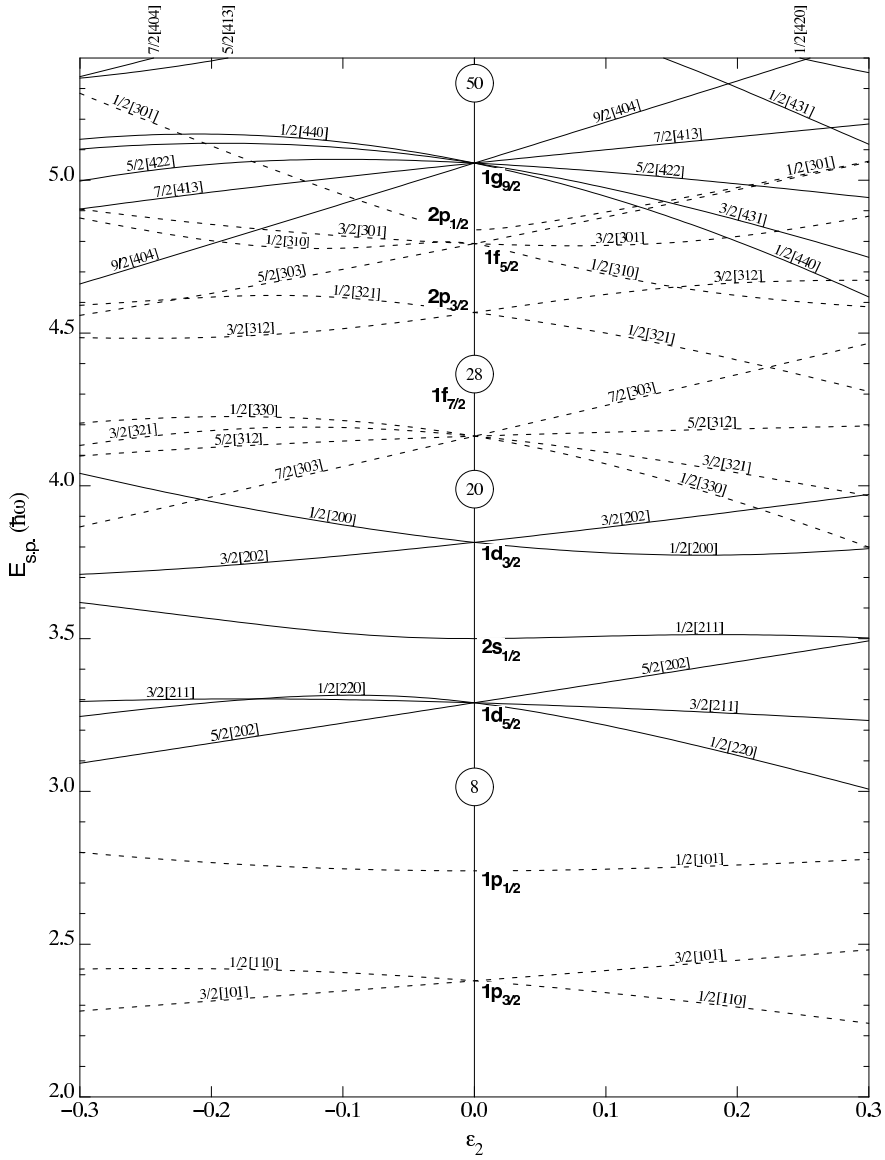

Figure 1.1: Nilsson diagram for $N(Z) \leq 50$ with the deformation parameter ϵ_2. Spherical nuclei are described by $\epsilon_2 = 0$, and prolate and oblate deformation are described by $\epsilon_2 > 0$ and $\epsilon_2 < 0$, respectively. At $\epsilon_2 = 0$ the magic numbers appear.

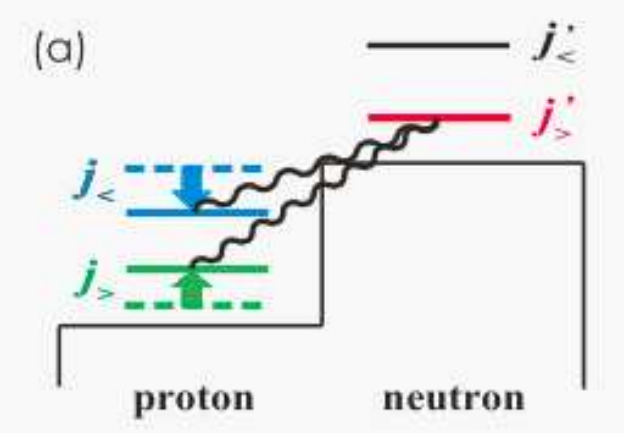

Figure 1.2: Schematic picture of the monopole interaction produced by the tensor force between a proton in $j_{>,<} = l \pm 1/2$ and a neutron in $j'_{>,<} = l' \pm 1/2$, taken from Ref. [16].

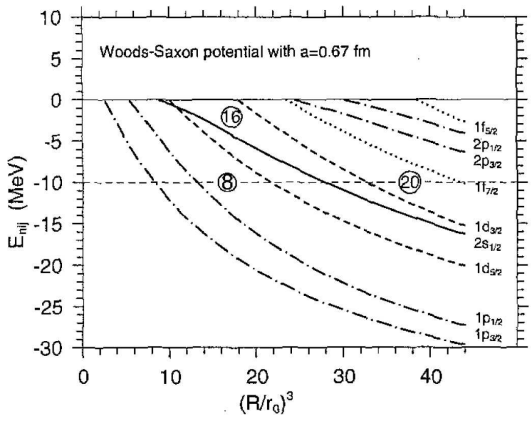

Figure 1.3: The energy of the neutron orbital in the Woods-Saxon potential, taken from Ref.[17]. The x-axis expresses the strength of the potential. When the neutron is weakly bound, the $s_{1/2}$ orbital becomes near to the $p_{1/2}$ orbital.

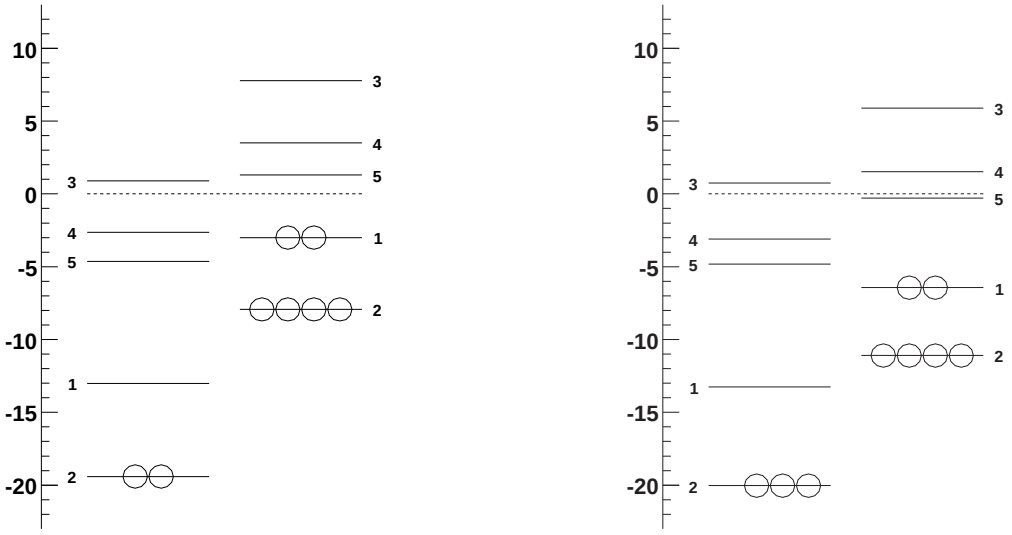

(a) ^{12}Be(g.s) (a) ^{13}B(g.s)

Figure 1.4: Effective single particle energies in the ground states of ^{12}Be (a) and ^{13}B (b), calculated using SFO interaction [15], are shown. Open circles indicate the nucleon in single particle orbitals. The numbers beside single particle orbitals indicate the orbitals in order of $p_{1/2}$, $p_{3/2}$, $d_{3/2}$, $d_{5/2}$, and $s_{1/2}$. Due to the tensor force, one more proton in the orbital 1 ($p_{3/2}$) changes the neutron shell gap between the orbital 2 ($p_{1/2}$) and 5 ($s_{3/2}$).

The effect due to the weakly bound nature is expected to be negligible because protons in neutron-rich nuclei are generally bound in a deep nuclear potential. It is also expected that the effect of the monopole interaction due to the tensor force is small. Figure 1.4 illustrates the occupation numbers in single particle orbitals and effective single particle energies in *psd* shell, for the cases of ^{12}Be and ^{13}B. The number of open circles indicates the occupation number in the corresponding single particle orbit. The effective single particle energies are calculated using the single particle energies and monopole interaction in SFO interaction ("present′" interaction in Ref. [15]). Comparing the single particle energies in their ground states, less occupation of proton $p_{3/2}$ orbit in ^{12}Be makes the gap between the $p_{1/2}$ and $s_{1/2}$ orbits in the neutron shell small, while the proton shell structures are almost identical in both nuclei. Nuclear deformation, however, is still presumed to affect the proton shell structure when the distributions of not only neutrons but also protons deform, as seen in the Nilsson diagram. Proton intruder states in light, neutron-rich nuclei are, therefore, signatures for the importance of deformation as the effect for the change of the single-particle orbital, *i.e.* the change of the shell structure.

1.2 Spectroscopic Studies via Transfer Reaction

In 1950, the direct transfer reactions such as the (d,p), (d,n), $(d,^3\mathrm{He})$, (α,t) and $(\alpha,^3\mathrm{He})$ reactions, opened up spectroscopic studies of the nuclear shell structure. The first spectroscopic study was performed by Butler for the ground and first excited state of ^{17}O nucleus based on the analysis of the angular distribution of (d,p) reaction [20, 21]. After the suggestion by Bethe and Butler [22], many stripping reactions on various nuclei were measured and the property of levels were studied [23, 24, 25, 26, 27]. Although the method of Butler was effective for the light nuclei and could predict the relative cross section, this method overestimated the absolute value of reaction cross section. In Ref. [28], the importance of the distortion of the outgoing wave was pointed out, which Butler's method neglected. At about the same time, the optical model was discussed, and the refraction and absorption in interior of nuclei were taken into account for the reaction cross section [29]. Analysis with distorted wave Born approximation (DWBA) has enabled us quantitative discussions on differential cross sections of direct reactions. A factorization of spectroscopic factor has also been introduced as a basic quantity to compare experimental data with predictions of nuclear models [30].

Spectroscopic studies of the shell structure via direct reactions with unstable nuclei has been opened by the one-nucleon knockout reaction [31] using a fast radioactive beam. In this reaction the ground state property of the incident nucleus was deduced from the longitudinal momentum distribution. From many measurements of this reactions with neutron-rich nuclei, the systematics of the ground state properties were revealed. The transfer reactions of (d,n) reaction on unstable nuclei were performed with deuteron in inverse kinematics [32, 33]. In these (d,n) reactions at incident energies higher than so called intermediate energy of a few tens MeV/nucleon, the reaction cross sections rapidly decrease and the kinetic energies of the recoiled particles were small in inverse kinematics. However, an application of α-induced transfer reaction on neutron-rich, unstable nuclei has been introduced recently [34]. The kinematic matching conditions become loose in this reaction even at intermediate incident energy region due to large negative Q-value of the reaction and to the fact that a proton in α particle is deeply bound and has a high-momentum component. This results in the moderate decreasing of the reaction cross section of the (α,t) reaction even at intermediate energies.

The difference in the energy dependence of the reaction cross sections between the (α,t) and (d,n) reactions can be explained by an estimation of the kinematic matching conditions [35, 36]. The conditions are the conservation of the linear and angular momenta, and the requirement that the transferred nucleon is in the reaction plane. The notations commonly used are listed below:

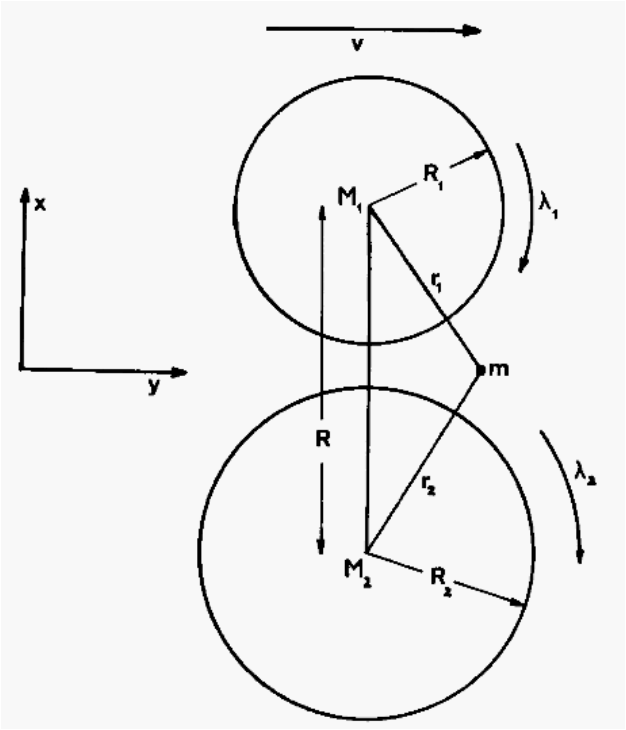

Figure 1.5: Schematic diagram of the transfer process. For notations, see the text. (Quoted from Ref. [36].)

$R_{1(2)}$ Radius of the nucleus 1(2)

$l_{1(2)}$ Orbital angular momentum which the transferred nucleon has in the nucleus 1(2)

$\lambda_{1(2)}$ Magnetic sub-state of orbital angular momentum which the transferred nucleon has in the nucleus 1(2)

m Mass of the transferred nucleon

v Relative velocity of the two nuclei in the region of transfer.

The schematic diagram of the transfer process is shown Fig. 1.5. A nucleon is transferred from nucleus 1 to nucleus 2.

Conservation of linear momentum: The momentum of a transferred nucleon should be almost conserved along y-axis and this conservation law is expressed as:

$$\Delta k = k_0 - \frac{\lambda_1}{R_1} - \frac{\lambda_2}{R_2} \approx 0, \tag{1.1}$$

where k_0 is a relative wave number $mv/\hbar$. For the more realistic case, a transition probability becomes large when $\Delta k_0 \leq \delta k = 2\pi/(R_1 + R_2)$.

Reaction	J^π	Q (MeV)	l_2	λ_2	$\Delta k/\delta k$	$\Delta L/\delta L$
^{12}Be$(d,n)^{13}$B	$1/2^+$	9.579	0	0	1.2	0.1
	$5/2^+$	9.579	2	2	0.4	1.7
^{12}Be$(\alpha,t)^{13}$B	$1/2^+$	-8.01	0	0	1.1	0.7
	$5/2^+$	-8.01	2	2	0.6	0.2

Table 1.1: Matching conditions estimated for the proton transfer reactions ^{12}Be$(d,n)^{13}$B and ^{12}Be$(\alpha,t)^{13}$B at 50 MeV/nucleon. For detail see the text.

Conservation of angular momentum: The angular momentum of the two interacting nuclei should be conserved as below,

$$\Delta L = \lambda_2 - \lambda_1 + \frac{1}{2}k_0(R_1 - R_2) + \frac{Q}{\hbar v}(R_1 + R_2), \tag{1.2}$$

where Q is the difference in the binding energies of the incident and outgoing particles, called the Q-value. The first term represents the difference of the angular momenta of the transferred nucleon before and after transfer. The other terms represent the change of the relative angular momentum due to the change of reduced mass, velocity of transferred nucleon, and distance (or $R_1 + R_2$) between the two nuclei. For a more realistic case, $\Delta L \leq \delta L = \sqrt{\gamma_1(R_1 + R_2)}$, where γ_1 is related to the binding energy ϵ_1 of the initial state by $\gamma_1 = 2m\epsilon_1/\hbar^2$.

Requirement for location of the transferred nucleon: The transition probability is large when the transferred nucleon is near the reaction plane. This is described by,

$$l_1 + \lambda_1 = \quad \text{even}, \qquad l_2 + \lambda_2 = \quad \text{even}, \tag{1.3}$$

where $l_{1,2}$ is the orbital angular momentum of the transferred nucleon in the nucleus 1(2).

We estimated the conditions of ^{12}Be(α,t) and ^{12}Be(d,p) reactions, listed in Table 1.1. The incident energy is 50 MeV/nucleon, which corresponds to $v/c \sim 0.315$ for both the reactions. The nuclear radii for this estimation are 2.116 fm for d [37], 1.671 fm for α [37], and 2.939 fm for ^{13}B calculated from $1.25 \times \sqrt[3]{A}$, respectively. Since the criteria for linear and angular momenta matching are given by $\Delta k/\delta k \leq 1$ and $\Delta L/\delta L \leq 1$, respectively, the (α,t) reaction has better kinematics condition than the (d,n) reaction for populating proton-single particle states. The better kinematical conditions of the (α,t) reaction are caused by the large negative Q-value of the reaction and the fact that a proton in an α particle is deeply bound and has a high momentum component as stated previously. Therefore, we have chosen the (α,t) transfer reaction for the in-beam γ-ray spectroscopy in inverse kinematics to investigate proton single particle states.

1.3 Previous Works on ^{13}B

The light, neutron-rich unstable nucleus ^{13}B has been experimentally studied through various measurement such as β-decay measurements [38, 39], ^{7}Li-induced reactions [40, 41], two neutron transfer reaction of (t,p) reactions [42, 43], neutron knockout reaction [44], β-delayed neutron measurement [45, 46], measurements of nuclear moments [47, 48, 49], multi-nucleon transfer reaction [50] and lifetime measurements of the excited states [51]. The ground state properties such as spin and parity were deduced from the measurement of β-decay of ^{13}B. A spin and parity of $3/2^-$ has been assigned to the ground state. The nuclear moments of the ground state, such as dipole and quadruple moment, were measured precisely in this decade and were compared with the result of a spherical shell model calculation [52]. The shell model calculation reproduces the measured nuclear moments and indicates a spherical shape for the ground state. The wave function of the ground state is reported in Ref. [53], where the spectroscopic factor of proton stripping reaction on ^{12}Be to the ground state of the ^{13}B nucleus and the configuration such as $(\nu sd)^2$ and $(\nu 1p)^2$ in the ground state are evaluated combining the measurement of delayed neutron emitting β decay of ^{14}B. It is found that the ^{13}B nucleus has a 20% admixture of $(\nu sd)^2$ in its ground state although the number of neutron in ^{13}B is a magic number ($N = 8$).

There are six known excited states below the neutron threshold of 4.87 MeV in ^{13}B found through the (t, p) reactions and Lithium-induced reactions. Although the parities of several excited states were determined by analysing the angular distribution of (t, p) reactions[42, 43], the spins have not been uniquely determined. One of the difficulty in the spin and parity assignment to the excited states in ^{13}B is the lack of bound ^{13}Be nuclei. Then the β decay of ^{13}Be to ^{13}B cannot be applied. In spite of this difficulty the information of the excited states have been extracted and the possible spins have been suggested through the experimental studies such as lifetime measurement of the excited states [51], spectroscopic study using knockout reaction [44], and measurement of multi-nucleon transfer reaction [50]. However, the spin of any excited state has been uniquely determined.

The aim of the present study is, by assigning spins to such excited states, to investigate the proton single particle state, and especially intruder state in the neutron-rich nuclei, and subsequently discuss the effects in three theoretical models on the change of the shell structure described in Sec. 1.1. For this purpose the in-beam γ-ray spectroscopy has been performed using the proton transfer reaction onto the largely deformed, neutron-rich nuclei ^{12}Be.

Chapter 2 describes the experimental setup including the details of the accelerator facility, beam monitors and counters, detector for reaction products and a newly developed γ-ray detector array: GRAPE. Chapter 3 describes the analysis procedure: the particle identification of incident and outgoing particles; the reconstruction of the γ-ray energies in particle-rest frame; and the deduction of the populations and differential cross sections by

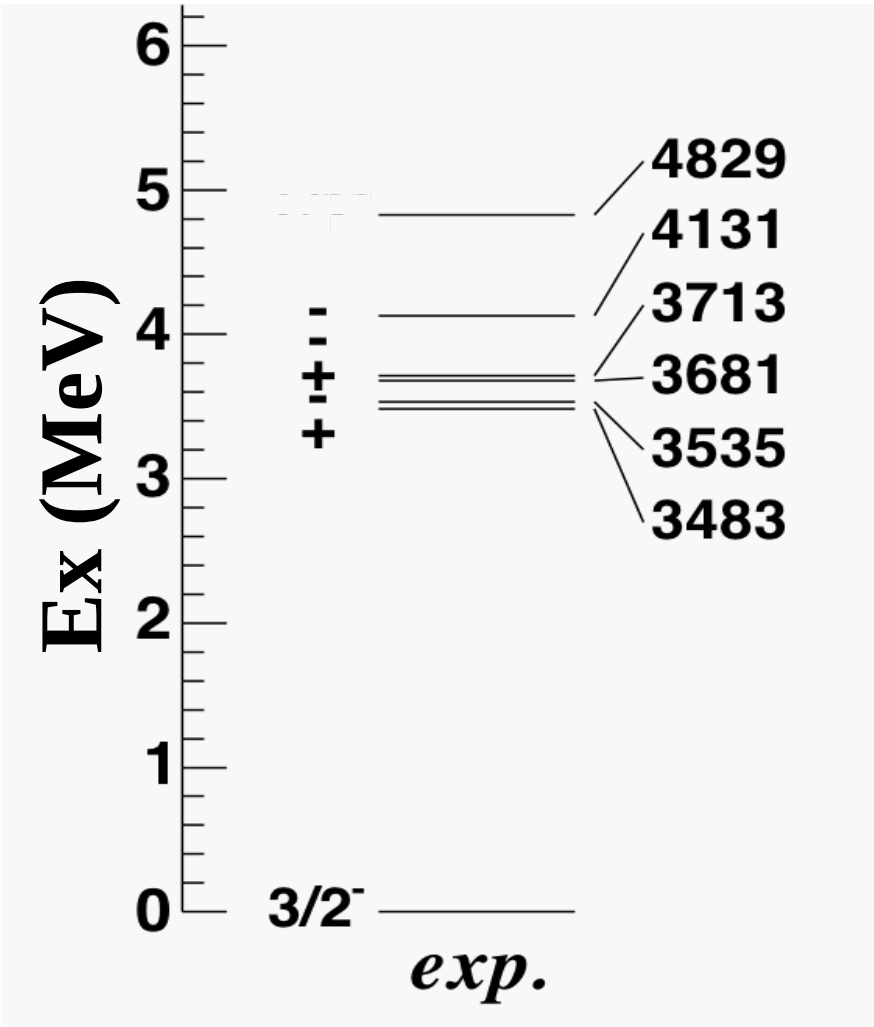

Figure 1.6: The level structure in ^{13}B deduced from experimental studies. The excited states below 5-MeV excitation energy are drawn with adopted spin and parities.

the decomposition of the γ-ray energy spectrum. The DWBA analysis of the angular differential cross sections also is described. The experimental results are described in Chapter 4. The γ-ray energy spectrum coincident with ^{13}B is shown with its energy decomposition. The deduced populations and angular differential cross sections with the result of DWBA analysis are also described. Discussion of the spin and parity assignment, and the property of single-particle state and intruder state are described in Chapter 5. Conclusion of the thesis are given in Chapter 6.

Chapter 2

Experiment

2.1 Overview

We performed an experiment of in-beam γ-ray spectroscopy of ^{13}B. The main object of this experiment is to clarify the property of the proton shell structure in $N = 8$, light, neutron-rich, unstable nucleus ^{13}B via the proton transfer reaction using a ^{12}Be beam with a liquid helium target. In order to identify the excited states and to assign the spin and parity, the de-excitation γ-ray and the angular distribution of ^{13}B were measured in coincidence.

The experiment was performed at RIKEN Accelerator Research Facility (RARF). A schematic view of the experimental setup is shown in Fig. 2.1. A ^{12}Be (secondary) beam was produced by using the fragmentation reaction of a ^{18}O (primary) beam and separated using RIKEN Projectile Fragment Separator (RIPS). The incident particles were identified on an event-by-event basis using the measured time-of-flight and the energy deposition. The time-of-flight, over a path length of 5.4 m, and the energy deposition were measured using two plastic scintillators located at the last two foci of the RIPS. The intensity and the purity of the ^{12}Be beam were typically 2×10^5 counts per second and 90%, respectively.

The 50 AMeV ^{12}Be beam bombarded a secondary target of liquid helium[54] located at the final focus of RIPS. A liquid helium target was chosen because of its statistical advantage (see Sec. 1.2) in terms of the experimental yields. The helium was condensed by a cryogenic refrigerator and kept below 4 K during the experiment. A target thickness of 143$\pm$5 mg/cm^2 was estimated from the velocity difference between outgoing particles measured with and without the liquid helium. The position and direction of the incident particles on the secondary target were deduced from the trajectory information of two parallel plate avalanche counters [55] located 30-cm apart from each other before the final focus. The outgoing particles were detected by a plastic scintillator hodoscope 3.5-m downstream from the secondary target with a 1×1 m^2 active area and an angular acceptance of up to 8 degrees in the laboratory frame. The plastic scintillator hodoscope consisted of 5-mm thick ΔE and 60-mm thick E layers. The ΔE layer was divided into 13 plastic scintillator bars vertically and the

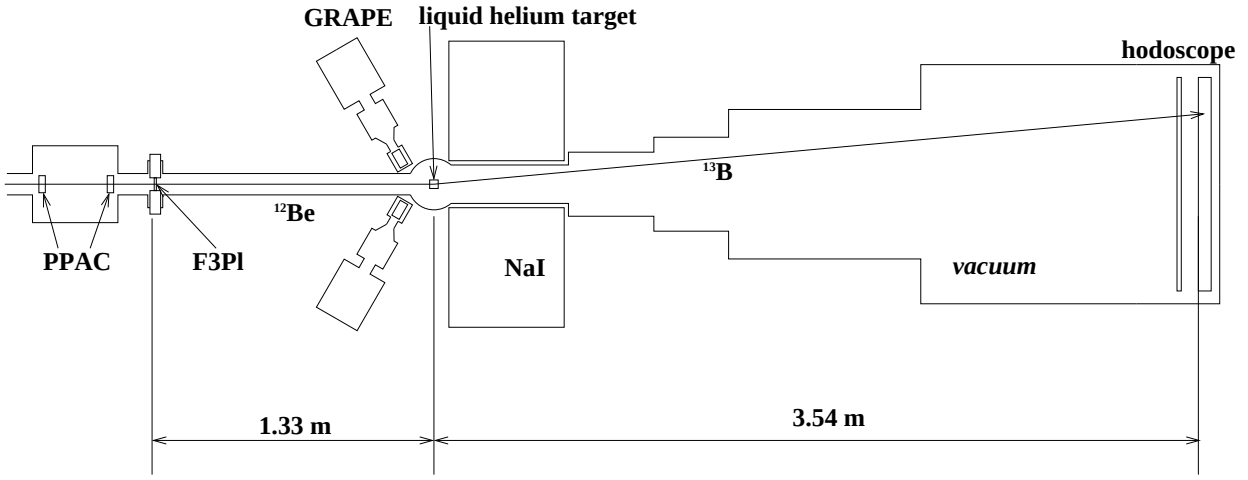

Figure 2.1: A schematic view of the experimental setup in the experimental area. The secondary beam of ^{12}Be comes from the left. Two PPACs are located before the last focus F3 in order to monitor the position and direction of the beam particles. A plastic scintillation counter is located to measure the time-of-flight of the incident particles and outgoing particles in combination with a plastic scintillation counter located at the second focus and a plastic scintillator hodoscope located at the end of the beam line. A liquid helium target is set on the beam axis. GRAPE was located at 140° respected to the beam axis. The outgoing particles stops in the plastic scintillator hodoscope. The inside of beam pipe is kept vacuum.

E layer into 16 plastic scintillator bars horizontally. The outgoing particles were identified on an event-by-event basis using the measured time-of-flight and the energy deposited in the ΔE and E layers. The mass distribution for $Z = 5$ particles was determined to be $\sim$0.25 atomic mass unit (one standard deviation). The time-of-flight between the secondary target and the hodoscope was deduced from the time information of the plastic scintillators located upstream from the secondary target and the plastic scintillator hodoscope. Position information for the outgoing particles was deduced from the time difference between the output signals from the two photomultiplier tubes attached to both ends of each scintillator bar and was used to determine the scattering angle. The angular resolution of the scattering angle in the laboratory frame was 0.5-degrees (one standard deviation).

The de-excitation γ rays were detected by an array of germanium detectors: Gamma-Ray detector Array with Position and Energy sensitivities (GRAPE)[56]. This consisted of 6 germanium detectors located at 140° with respect to the beam axis. Each detector contains two cylindrical crystals 6 cm in diameter and 2 cm thick, with a common anode between them. The cathode attached to each crystal is segmented into a 3×3 matrix. GRAPE provides position information of the γ-ray interaction point, which is extracted from a pulse shape analysis of the signal from the cathode [56, 57]. The intrinsic energy resolution and

the full energy peak efficiency were typically 2.7 keV (FWHM) and 0.4%, respectively, for 1332-keV γ rays from a standard ^{60}Co source. The energy resolution after correcting for the Doppler shift was deduced to be 1.3% (FWHM) for 2.1-MeV γ rays, corresponding to the decay of the first 2^+ state of ^{12}Be moving with 30% the velocity of light. The excited states of ^{13}B populated in the reaction were identified by measuring the energy of the de-excitation γ rays.

The trigger for the data acquisition required that all the signals from the plastic scintillation counter at F3, the hodoscope and the GRAPE were coincident.

In Sec. 2.2, the production of the secondary beam is descried with a summary of RIPS beam line. The details of the detector systems such as the counter and tracker for the incident particles, the plastic scintillator array for the outgoing particles, and the γ-ray detector array are described in Sec. 2.3, 2.3.3, and 2.4, respectively. The secondary target is described in Sec. 2.5. The electronic circuit, data acquisition system and analyzed data set are summarized in Sec. 2.6.

2.2 RI Beam Production

2.2.1 Projectile Fragment Separator: RIPS

The layout of the RIKEN Accelerator Research Facility is shown in Fig. 2.2. To produce an RI beam, a heavy-ion primary beam is accelerated by the ring cyclotron $K = 540$ up to several tens to 135 MeV/nucleon and is transported to a production target in the D room. A layout of RIPS [58] is shown in Fig. 2.3. The RIPS beam line consists of two dipole magnets D1-D2, twelve quadrupole magnets Q1-Q12, and four sextupole magnets SX1-SX4. There are four focal point interest, denoted F0, F1, F2, and F3, respectively. The production target is mounted at F0 in the D room. A dispersive focal plane F1 and a achromatic focus F2 are used for the isotope separation, while the final focal plane F3 is used as the target position for the experiment. The experimental devices of the F3 chamber are installed for measuring the secondary beam. The secondary target to populate reaction products is usually placed around F3.

The isotope separation of reaction fragments is achieved as detailed presently. Various nuclei are produced in projectile fragmentation reactions of a primary beam on a production target at F0. The reaction fragments are emitted in a small forward cone with almost the same velocity as the projectile beam. The magnetic rigidity, $B\rho \propto p/Q$, of the secondary beams can be selected by a slit at the momentum dispersive focal plane F1, where the p and Q stand for the momentum and the charge state of fragment, respectively. In the case of light nuclei ($A < 80$), the fragments are fully stripped so that the charge of the fragment equals the atomic number, $Q = Z$. In the stage from F0 to F1, isotopes are thus selected roughly by their A/Z values, since the fragments have almost the same velocity. In order

to improve the purity of the secondary beam of interest, a wedge-shaped energy degrader, made of aluminum, is installed at F1. After passing through the degrader, the magnetic rigidities of the beam particles are modified due to the energy loss, which depends on Z and the velocity of the isotopes. The modified rigidity is analyzed by the D2 magnet and selected by a slit at the first achromatic focus F2. In the next stage from F1 to F2, the beams are selected by a different function of A and Z. This function is approximately proportional to $A^{2.5}/Z^{1.5}$ of the isotopes. The isotope separation at RIPS is thus achieved by combining the A/Z selection at F1 and $A^{2.5/Z^{1.5}}$ selection at F2. Finally, the selected isotope and cocktail beam are transported to the final achromatic focal plane F3, where a detector setup is placed.

2.2.2 Parameters of ^{12}Be Beam

A secondary ^{12}Be beam was produced by a projectile fragmentation of a 100 AMeV ^{18}O beam on a beryllium primary target with a thickness of 1.85 g/cm^2, and separated by using RIPS. The primary beam of ^{18}O was chosen by the intensity of the primary beam itself (available up to 1 pμA) and the one of the secondary beam. The ^{18}O nucleus is empirically known to be good for the production of the light neutron-rich unstable nuclei below $Z = 8$. The primary target of ^9Be was also known to be good for the production of the neutron-rich unstable nuclei.

The rate of 2 $\times$ 10^5 Hz was reached for the secondary beam. Although the more intense beam was available, higher intensity induces too many pile up events. The momentum window $\Delta p/p$ was set to $\pm$ 1% by using a slit at the first momentum dispersive focal plane, which was narrow enough to discriminate the ^{12}Be from contaminant particles by setting the time window on the time distribution (see section 3.3.1). At the first achromatic focus (the second focus), the window from $-$10mm to 0mm was set to separate the ^{12}Be. The energy of the secondary beam was calculated from the $B\rho(D2)$ value, however, it needed a correction since the window was asymmetric, *i.e.*, the extracted beam didn't traverse the center of F2, since the beam axis was slightly mismatched to the optical axis in the present experiment. The correction factor was calculated from the momentum dispersion at the F2 of 37mm/%. The energy was higher by 0.135% than that obtained from the $B\rho_{D2}$ value. The energy was 49.90 AMeV after the last focus F3 with consideration for the energy deposited in the material between F2 and F3. The purity of ^{12}Be was $\sim$90%. The detailed parameters of RIPS optimized for the production of ^{12}Be are listed in Table 2.1.

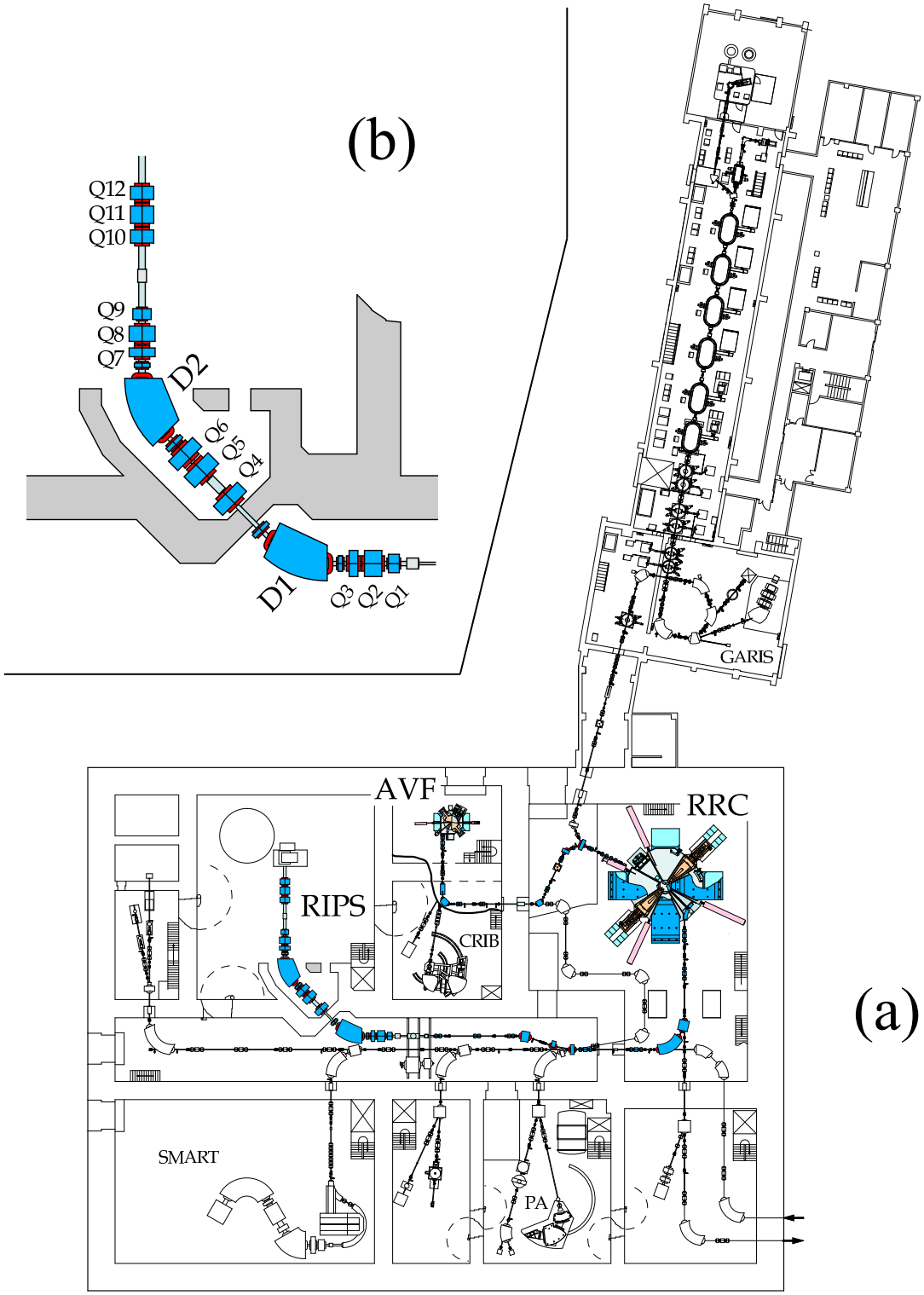

Figure 2.2: (a) Layout of the RIKEN Accelerator Facility. A primary beam is accelerated by AVF cyclotron and RIKEN ring cyclotron (RRC). (b) A enlargement of RIPS in the figure (a).

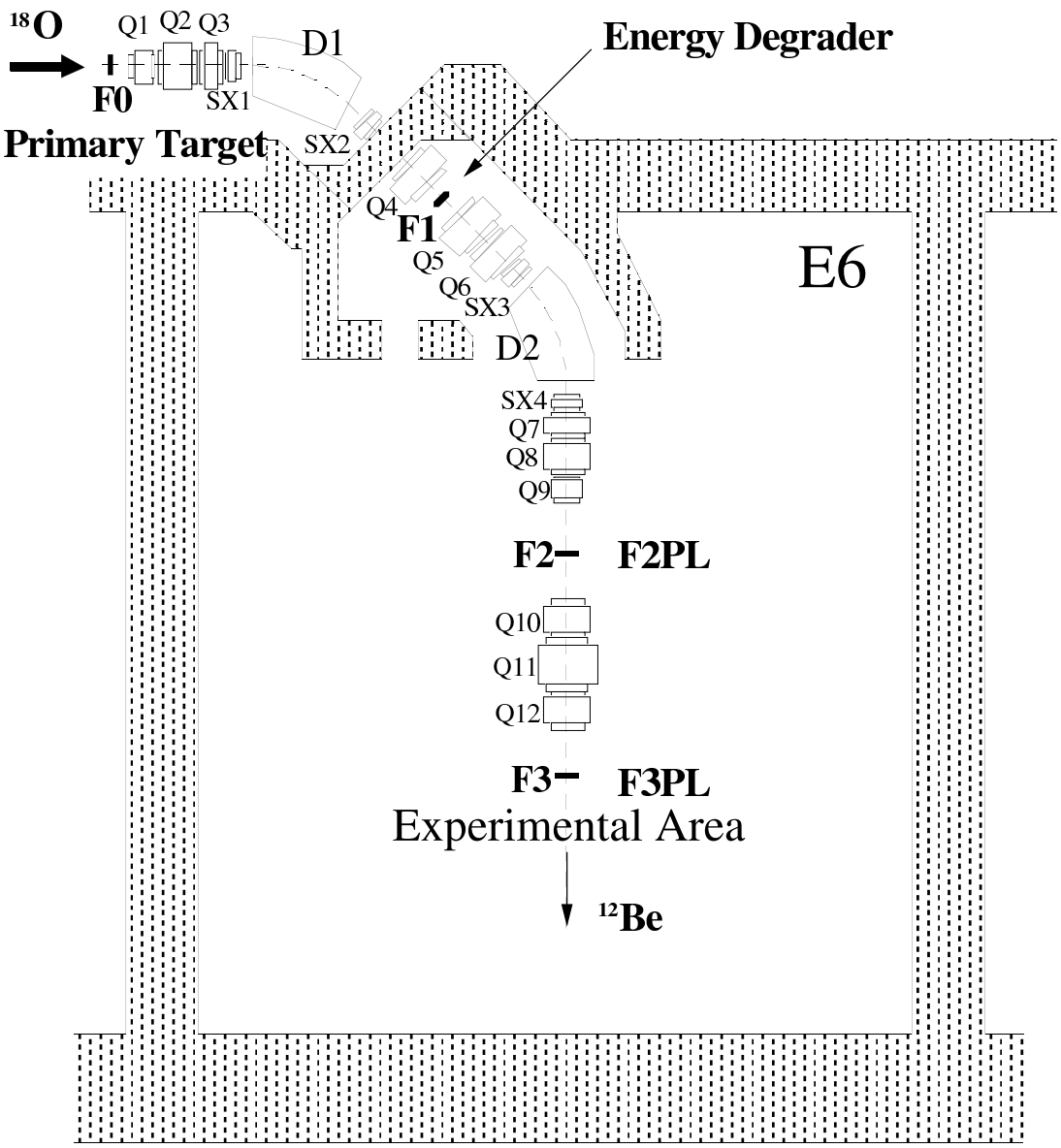

Figure 2.3: Layout of the RIKEN Projectile Fragment Separator, RIPS. The primary projectile fragmentation reaction occurred at F0. Projectile-like fragments are analyzed and selected in two stages of F0-F1 and F2-F3 to produce and select radioactive beam particles of desired nuclei. The final focus of F3 is provided for the experimental setup.

Primary Beam	Energy	Intensity
^{18}O	100 AMeV	100 pnA
Primary Target	Thickness	F1 Al Degrader
^{9}Be	1.85 g/cm^2	1099 mg/cm^2
D1 Field	D2 Field	F1 Slit
3.525 Tm	3.150 Tm	$\pm$1 %
F2 Slit		
-10mm +0mm		
Secondary Beam	Energy@F3	Intensity
^{12}Be	50 A MeV	200 kcps

Table 2.1: Parameters of RIPS to product secondary ^{12}Be beam via the projectile fragmentation reaction. See the text for details.

2.3 Detectors for Incident and Outgoing Particles

2.3.1 Plastic Scintillators

Two plastic scintillators 0.5 mm-thick with 7×7-cm^2 active are were placed at two foci, F2 and F3, of RIPS (F2PL and F3PL, respectively) in order to deduce the velocity of the incident particles and to identify incident particles on event-by-event basis through the measurement of energy deposition (ΔE) and time-of-flight (TOF). The flight length between F2PL and F3PL were 5.4 m. Two 2-inch photomultiplier tubes (PMT's) were attached to the both side of each plastic scintillator in order to reduce the ambiguity of timing and ΔE depending on the hit position of particles. The timing information were obtained as the arithmetic mean of two timing signals from the two PMTs. The ΔE information were obtained as the geometric mean of two pulse height signals from the two PMTs. The time difference between the F2PL and F3PL was used as the TOF information for the incident beam velocity and the particle identification. The ^{12}Be beam was identified and discriminated from contaminants by using the ΔE-TOF method.

2.3.2 Parallel Plate Avalanche Counters

Two delay-line type Parallel Plate Avalanche Counters (PPACs) [55] were placed at 185- and 155-cm upstream of the secondary target in order to monitor the position and direction of secondary beam. The expanded view of a PPAC is shown in Fig. 2.4. The active area of each PPAC was 100×100 mm^2, and the effective length of the delay line was 100 mm. The PPAC was filled typically 8.6-Torr C_3F_8 gas and supplied +910-V voltage to the anode

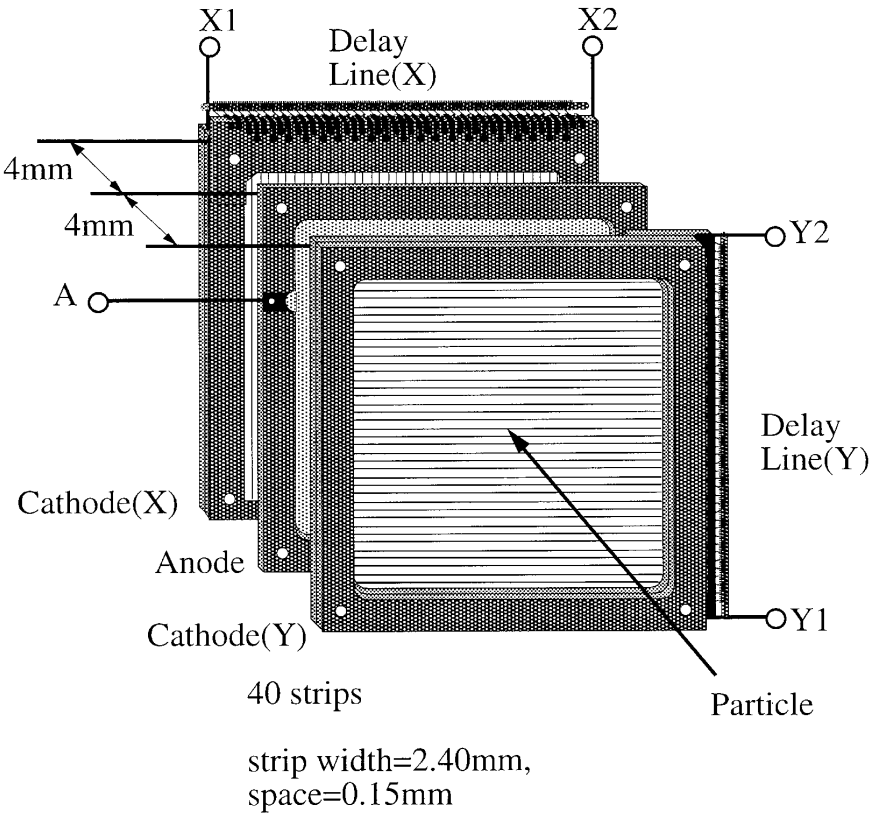

Figure 2.4: Exploded view of the delay line parallel plate avalanche counter(PPAC), taken figure from Ref. [55].

plane. The high voltage was optimized to maximize the detection efficiency. The hit position on PPAC was obtained from the time difference between two timings of the signals from the both ends of the delay line. The typical transition time of the signal was 0.8 ns/mm and the sum of transition time of two signals was to be a constant, *e.g.*, 80 ns for the effective length of the delay line. This condition was used to reject multi-hit events. The position of the incident particles on the secondary target was determined by extrapolating the hit positions obtained the two PPACs. The typical position resolution on the PPAC was 0.5 mm (FWHM), and the resolution of the extrapolated position on the secondary target was 4.3 mm. The corresponding angular resolution was 3.4 mrad. The details of the resolutions are described in section 3.3.2.

2.3.3 Plastic Scintillator Hodoscope

A plastic scintillator hodoscope was placed at the end of beam line in order to identify the outgoing particle and to determine their velocity and scattering angle. The hodoscope

was installed in the vacuum chamber in order to decrease the energy losses and multiple scatterings of outgoing charged particles along the flight path. Figure 2.5 shows a schematic view of the hodoscope. The hodoscope itself consisted of three layers, ΔE, E, and E'. However, the first two of them were used since the outgoing particles deposited all the kinematic energy and stopped in the E layer. The used layers were 5 mm-thick ΔE and 60 mm-thick E layers. The hodoscope had 1×1 m^2 active area and was located 3.5-m downstream of the secondary target with its symmetry axis along the beam line. The ΔE layer was divided horizontally into 13, and the E layer was divided vertically into 16 scintillator bars, respectively. The widths of the scintillator bars at the central part in each layer were narrower to improve the balance of the counting rate among the scintillator bars, and they were 40 mm and 38 mm for the ΔE and E layers, respectively. The widths at the other part were 100 mm and 75 mm, respectively. The timing of the particle arrival was deduced from the sum of two timings of the PMT signals without the ambiguity due to the hit position. The velocity after the secondary target was deduced in combination with the F2PL and F3PL. The energy deposited was deduced from the multiplication of the charge integration of the PMT signals without the ambiguity due to the hit position. The hit position along the vertical and horizon axis were deduced from the time difference between the two timings of the PMT signals in the ΔE and E layers, respectively. The time resolutions were typically 121 ps and 106 ps and the position resolutions were 19.5 mm and 17.1 mm for ΔE and E layers, respectively. The angular resolution was 0.5 degrees to the secondary target in laboratory frame and the corresponding one in center-of-mass frame was 2.4 degrees.

2.4 Detectors for γ Rays : GRAPE

An array of germanium detectors, called "GRAPE" (**G**amma-**R**ay detector **A**rray with **P**osition and Energy sensitivity), has been developed aiming at the precise determination of the γ-ray interaction position and the resulting precise Doppler-shift correction for the γ rays emitted from fast moving ($\beta \sim 0.3$) nuclei. The position resolution after pulse shape analysis was obtained to be less than 3 mm while the thickness of the germanium crystal was 2 cm. The energy resolution after Doppler correction was 1.3% (FWHM) for the γ ray emitted from the fast moving ^{12}Be, so far. In this section, the structure of the GRAPE (in section 2.4.1), the principle of the pulse shape analysis (in section 2.4.2), and the consideration of the location (in section 2.4.3) were described. The electronic circuits for the GRAPE are described in section 2.4.4

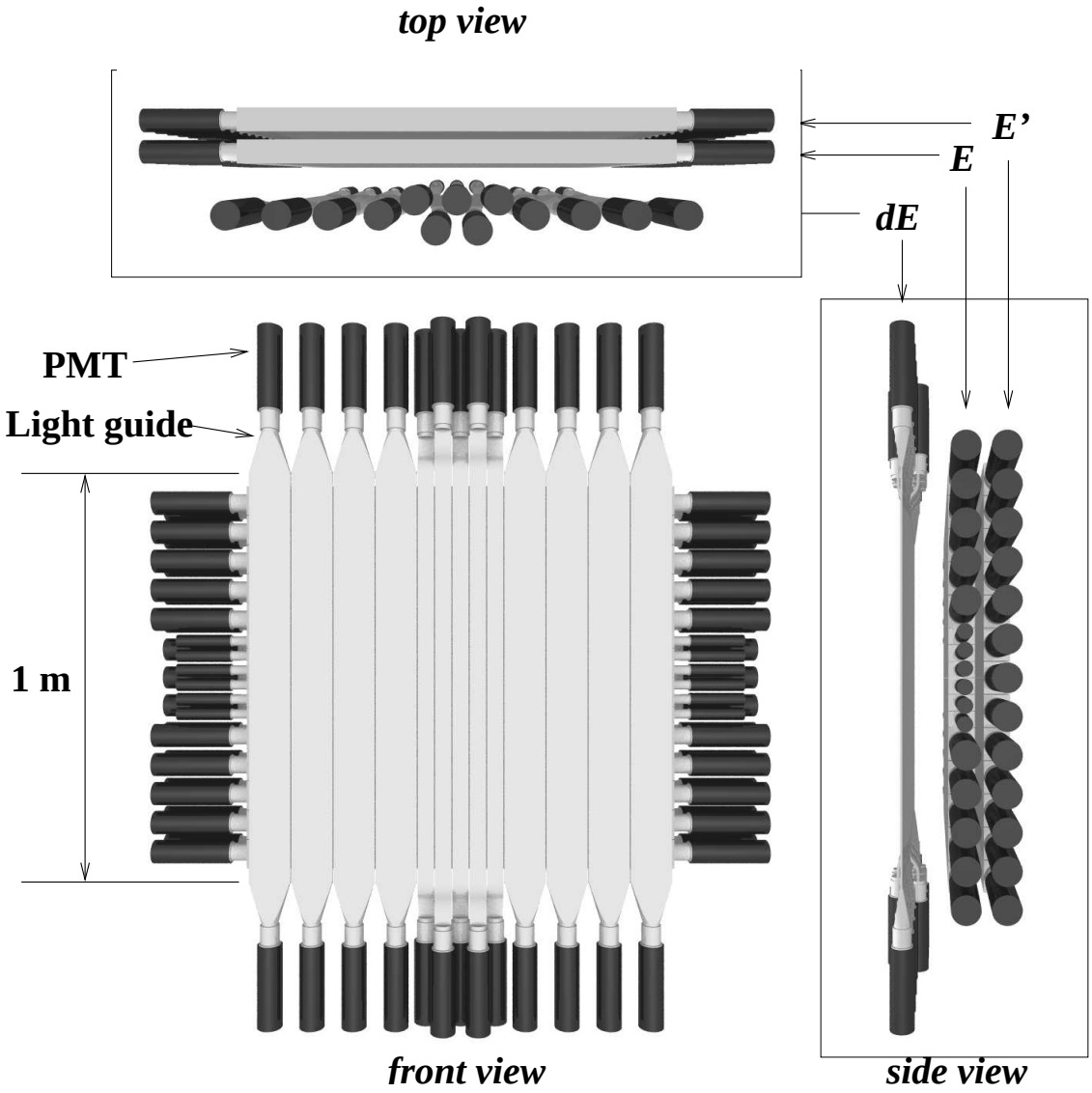

Figure 2.5: Schematic view of plastic scintillator hodoscope with front, side and top views. The hodoscope consisted of three layers of ΔE, E, $E^{'}$, the two of them were used. The ΔE and E layers were 5-mm and 60-mm thick and were divided into 13 and 16 bars, respectively. Two PMTs were attached at the both ends of each bar. The timing, charge, and position information were extracted from the signals of hodoscope.

2.4.1 Structure of GRAPE

Figure 2.6 shows a schematic view of the inner structure of the planar γ-ray detector used in the GRAPE. Each detector contains two cylindrical crystals of 2-cm thickness and 7-cm in diameter. The crystal surrounded by a cooler ring. The ring was made from aluminum in order to avoid the attenuation of γ rays from the surface of the cylindrical crystal. The anode between the two crystals was energized with a positive voltage of typically 2500 V. The cathode at the other end of each crystal was divided into 3 $\times$ 3 electrode segments and a 5-mm wide guard ring. The guard ring makes the electronic field uniform even in the edge region of the cathode. The resulting effective volume of germanium crystal was 2-cm thick and 6 cm in diameter. The signal from each cathode was pre-amplified independently and every nine signal from the crystal was summed up to reconstruct the net-charge signal. The number of signals from one crystal was twenty and the total number from the GRAPE was 120 in the present experiment. These signals were processed to obtain the charge, timing and position information. The detail of the signal processing is described in the section 2.6. To obtain the charge information, we can choose two ways; the add back of each digitized signals from the cathode segments (digital sum) and the add back of two net-charge signals (analog sum). The advantage of the digital sum is the better resolution than that of the analog sum while the advantage of the analog sum is the better efficiency than that of the digital sum. The detail of deduction of the γ-ray energy is described in section 3.5.1. The basic idea of the position extraction and the analysis using it are described in section 2.4.2 and 3.5.3.

The typical energy resolution is 2.5 keV (FWHM) and the full-energy-peak efficiency taking the solid angle into account is 0.4%, respectively, for 1332 keV γ ray emitted from ^{60}Co standard source located at the secondary target position.

2.4.2 Basic Concept for Extraction of γ-ray Interaction Position

The interaction position of γ ray was extracted based on a pulse-shape analysis of charge pulses from segmented cathodes. Figure 2.7(a) shows a schematic of pulse shapes from the cathodes. There are two cases of hit patten as denoted by black dots in the first row of the figure. In the left column the electron-hole pair is created near the cathodes and in the right column it is created near the anode. The letters A, B and C denote the different segments. In the second and third rows, dotted curves show the contributions of the electron (e) and hole (h), while the solid curves show the pulse shape to be observed. It is assumed for simplification that the drift velocities of the electron and hole are constant and same. The shapes of the sum of the signals from cathodes A, B and C are identical (shown in the second row) for the two cases; however, the contributions of the electron and hole are different. On the other hand, the shapes from B (the fourth row) differ between the two cases because the polarity of the induced signals in its neighbor segments (the third row) also differ. It is

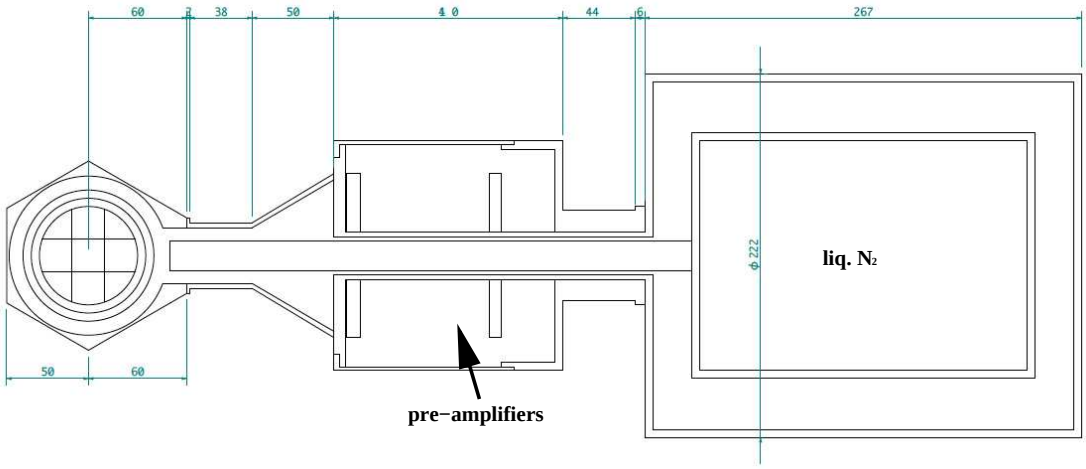

(a) A drawing of a GRAPE detector

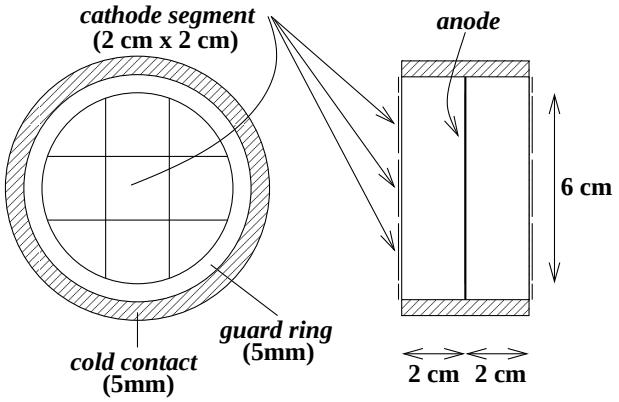

(b) Schematic view of a crystal in a GRAPE detector

Figure 2.6: (a) A drawing of a GRAPE detector. (b) Schematic view of planar type germanium detector used in GRAPE. Two crystals were in a chassis with an anode between them. The size of each crystal was 2 cm thick and 7 cm in diameter. The anode was energized typically with a positive voltage of 2500 V. The cathode was divided into 3×3 segments and surrounded by a guard ring.

found through the simulations of the pulse shapes that the depth of the γ-ray interaction point is characterized by two zero-cross timings picked up after $(CR)^2(RC)^4$ shaping of the net-charge (T_{sum}) and the hit segment (T_{seg}) signals.

The simulated correlations are shown in Fig. 2.7(b). Assuming the rotational invariance, the correlations are divided into three groups, *i.e.*, center, side and corner, as indicated in the figure. Each dotted line corresponds to a certain point in the cathode plane and each closed circle corresponds the depth at that point. The depths are divided into four groups and colored for easy viewing. As seen in the figure, the correlations are well discriminated from each other, although those in the region around 6 mm are overlapping.

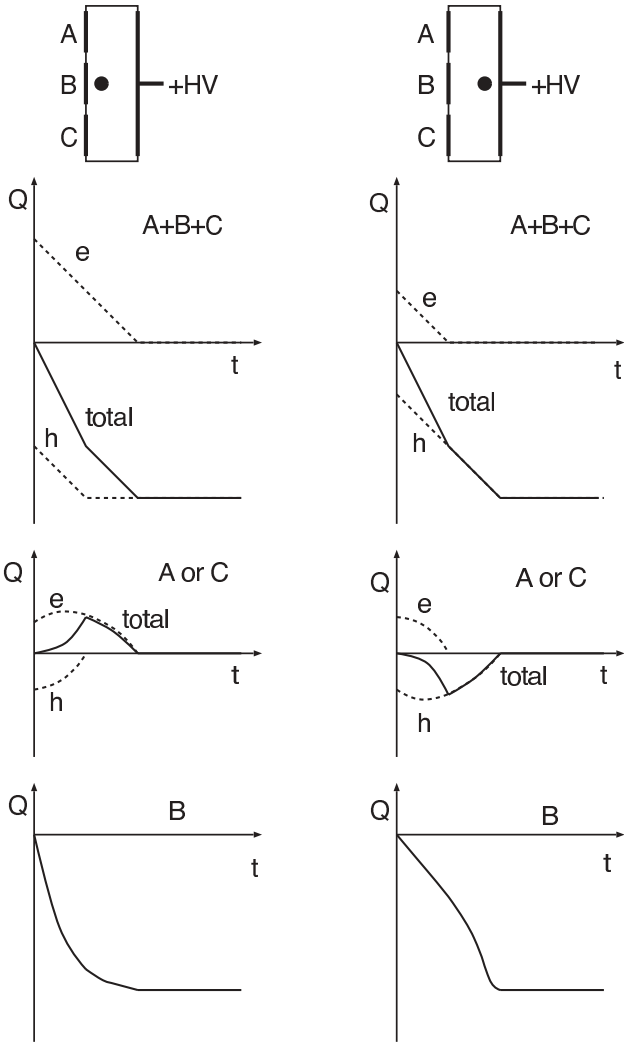

Figure 2.7: Schematic pulse shape from a segmented planar detector. Black dots in the top row denote the positions where an electron-hole pair is created in the example. The second and fourth rows show the pulse shapes, which are used for the pulse-shape analysis and the third row shows the induced pulse shapes which are essential for the difference of the pulse shapes in the fourth row. (taken from ref. [56]).

For utilizing this method, three kind of circuits are developed: analog adders for the sum of the nine cathode signals, $(CR)^2 - (RC)^4$ shaping amplifiers, and discriminators for picking off the zero-cross timings.

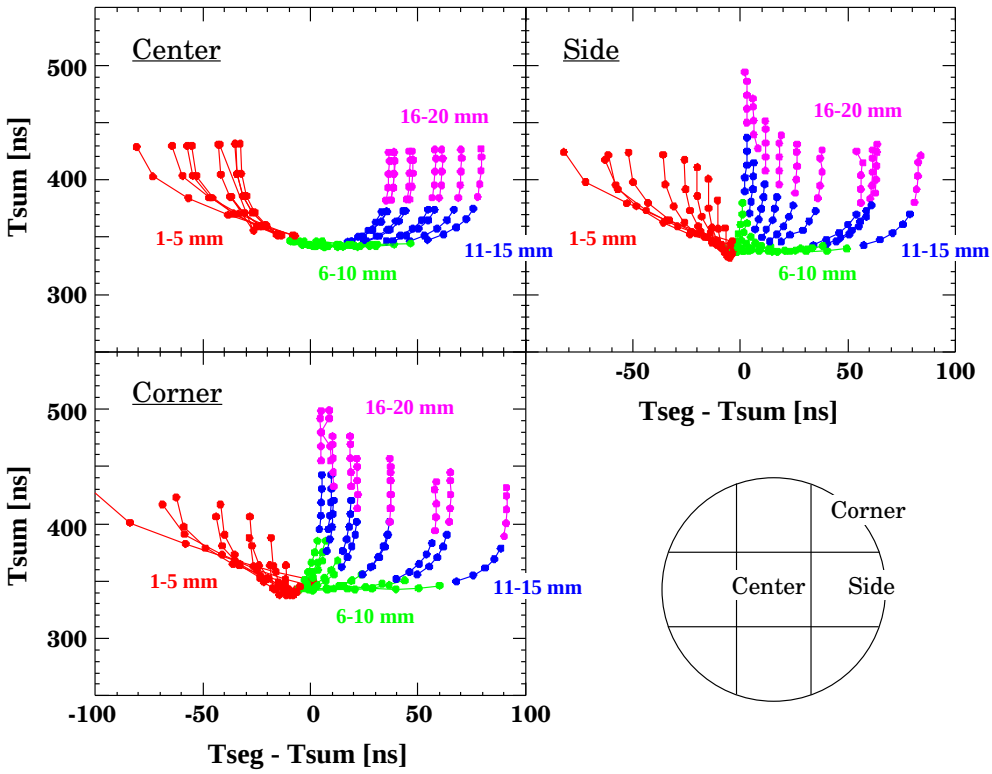

Figure 2.8: Zero-cross timing correlations between the summed cathode signal and hit cathode signal subtracted by summed signal. Each connected line corresponds to the set of zero-cross timing correlations at a certain point in the cathode plane.

2.4.3 Consideration on the positioning of GRAPE

In order to reduce Doppler broadening, the position of GRAPE are considered. For Doppler correction, γ-ray emission angle and the velocity of the outgoing particle are needed. The emission angle is calculated in combination with the γ-ray detection point, the stopped position of the outgoing position in hodoscope and the γ-ray emission position in the secondary target. The emission position, which is same as the position where a reaction occurs in most cases, is should be on the line extrapolated using the extrapolated momentum vector of an incident particle. In the extrapolation, the reaction is assumed to occur at the center of the secondary target along the beam axis, since the position along the beam axis cannot be determined due to the limitation of the setup. Because of this assumption, the ambiguities of the emission angle and the velocity persist in the Doppler correction. However, it is found that the effect of these ambiguities vanish when the γ-ray detector is located at a certain position, described below.

The measured energy is affected by the Doppler shift and represented as,

$$E_{lab} = E_{cm}/\gamma_u(1 - \beta_u \cos\theta_u), \tag{2.1}$$

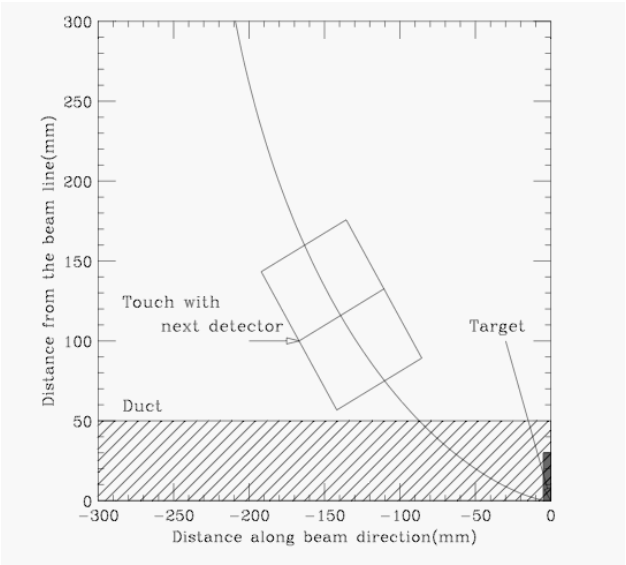

Figure 2.9: A result of the search for the position of the GRAPE. The curve shows the positions of the detector where the Doppler broadening due to the ambiguity of the reaction position along the beam axis. The position of the GRAPE is determined as close to the secondary target as possible.

where $E_{cm(lab)}$ are the energy of the γ-ray in the center-of-mass frame (the laboratory frame), β is velocity in units of light speed, and θ is the emission angle in the laboratory frame. The subscript $u(d)$ means that the reaction occurs at the upstream (downstream) end of the secondary target. On the other hand, now, the reaction is assumed to occur at the center of the secondary target. Then, the angle and the velocity are calculated to be θ_c and β_c, respectively, differing θ_u and β_u. The conditions which realizes the smallest ambiguities are

$$\gamma_u(1 - \beta_u \cos\theta_u) = \gamma_c(1 - \beta_c \cos\theta_c), \tag{2.2}$$

$$\gamma_d(1 - \beta_d \cos\theta_d) = \gamma_c(1 - \beta_c \cos\theta_c), \tag{2.3}$$

and they are found to be satisfied when the detectors are located at large (backward) angles. These conditions for any point in the secondary target are satisfied when the detector are located at the position satisfied the conditions listed above. Figure 2.9 shows the result of the search for the optimum detector positions. When the detector is located at the optimum position on the curve, the conditions described above are satisfied and the effect due to the ambiguity of the reaction position along the beam axis becomes small. The position of the detectors should be as close to the secondary target as possible from the vantage point of the detection efficiency. In a realistic way, the finite size of the detectors determine the position on this curve, and GRAPE is placed at 140° to the beam axis, about 180 mm apart from the secondary target.

2.4.4 Signal Processing for GRAPE

Figure 2.10 shows a schematic flow of the signal processing for GRAPE. Each detector within GRAPE has two crystals inside it and nine segmented cathodes for each crystals. This section describes the signal processing used for GRAPE focusing on one crystal for simplicity. The outputs from the nine cathodes are first processed by individual pre-amplifiers. The pre-amplified signals are summed up to reproduce a net-charge pulse by a analog adder, called the sum amplifier. Since the gains of pre-amplifiers are not same, the gain for each signal must be tuned so that the pulse height of each signal for a given energy deposition is same as the others. We tuned the gains of totally 108 channels manually. The pulse height of each signal, however, is not exactly same. A more precise correction is needed in offline analysis (see Sec. 3.5.1). All ten signals, *i.e.* nine cathode signals and one net-charge signal, are transferred to the flow **A**. Each signal is divided into two signals in order to obtain charge and pulse-shape information. To obtain the charge information, the signal is integrated and shaped into a Gaussian pulse, and the pulse height is digitized by a peak-sensitive ADC (V785 VME module). The pulse-shape information is deduced as the zero-cross timing of the $(CR)^2 - (RC)^4$-shaped pulse. The timing is digitized by a TDC, (V775 VME module). The timing of the γ-ray emission is approximately replaced by the detection timing since the the difference among the detection timings is at maximum 500 ps. The detection timing is extracted from the net-charge pulse with fast shaping and amplitude-rise-time compensation (ARC) method (**B**). The ARC is realized by using the CFD with small delay time of 50 ns. The detection timing is digitized by a TDC (C006 CAMAC module). The detection timing from each crystal is also used as a trigger indicated by Ge-i trigger, where i is the ordinal number of the crystal. A trigger signal *GRAPE* is made when at least one γ ray was detected in the GRAPE.

The details of the data acquisition from the VME and CAMAC modules is described in section 2.6.

2.5 Secondary Target

The secondary target of helium was liquidized to be thick enough to perform the present measurement with a low intensity RI beam. The helium target is cooled below a boiling point of 4.2 K at 1 atm. The typical density of the liquid helium at 1 atm and 4 K is 125 mg/cm^3, which is 700 times larger than that of the gas. Due to the higher target density of the liquid helium compared to the gaseous, more target nuclei allows for better reaction statistics. Figure 2.11(a) shows the schematic view of the liquid helium target system used in the present experiment. The system consisted of a cryogenic refrigerator, a target cell and two stages of thermal-conductive materials between the two. The first stage cools down to 60 K and also cools down the heat radiation shield covering the second stage and target

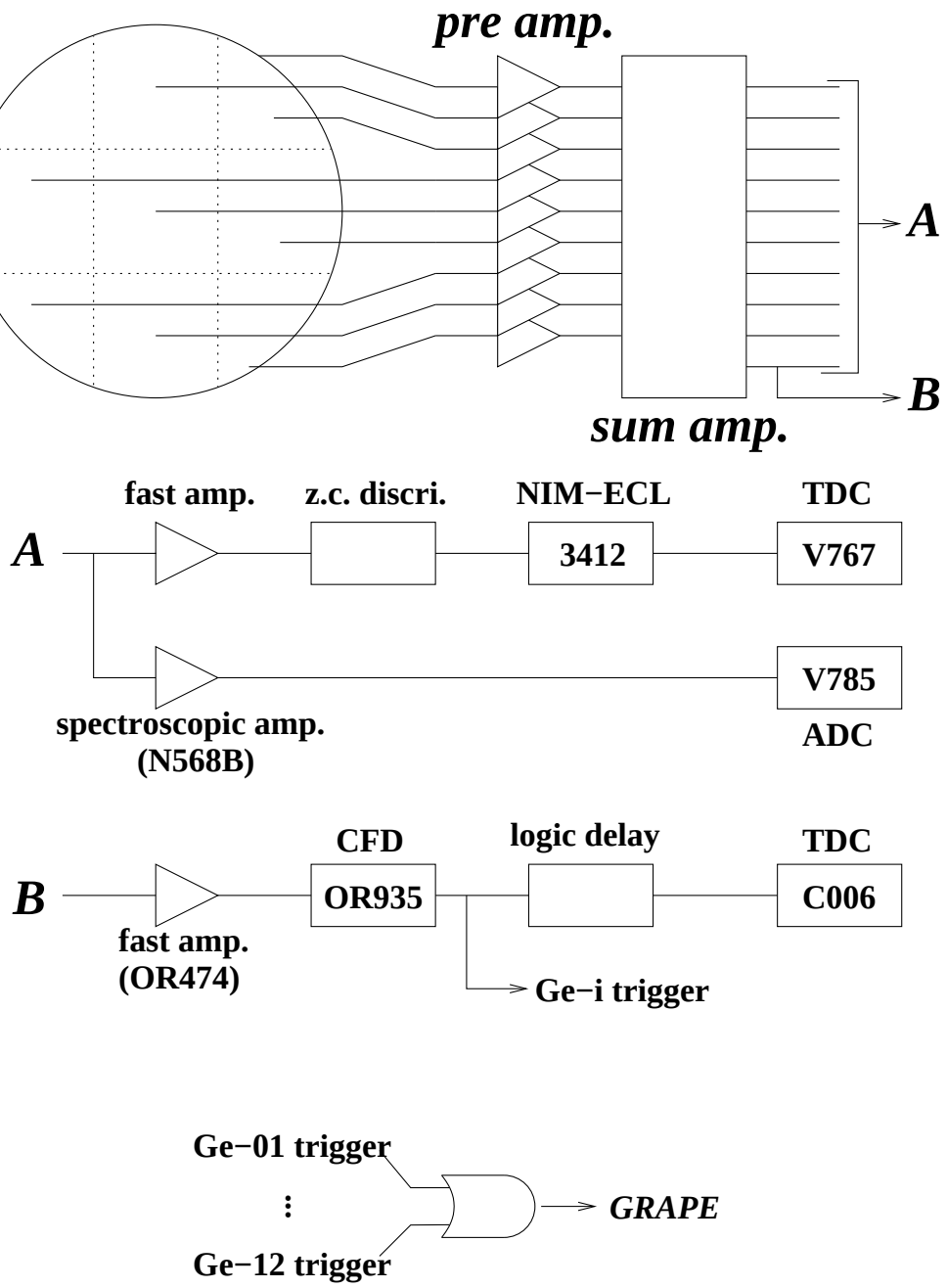

Figure 2.10: Schematic view of the electronic circuits for the signal processing of the GRAPE.

cell. The shield had the window covered with 6-μm thick Havar foils. The second stage cools down to 4 K and also cools down the target cell and the helium filled therein. The front view and cross section of the target cell are shown in Fig. 2.11(b). The target cell had windows of 24-mm diameter at the entrance and exit. The windows were covered with Havar foils same as the shield. At the bottom of the target cell a thermometer was installed to monitor the temperature of the helium. The temperature and pressure remained stable at around 4 K and 1 atm. The target thickness was extracted to be 143$\pm$5 mg/cm^2 from the velocity difference of outgoing particles in the experimental data sets (w/ Liq.He and w/o Liq. He).

2.6 Signal Processing and Data Acquisition

The signals from the detectors generated in the reactions induced by the secondary beam were processed by electronic circuits and taken by a general purpose computer on an event-by-event basis. Section 2.6.1 describes the process of the signals from each detector, section 2.6.2 describes the data acquisition system consisting of several general purpose computers, and Sec. 2.6.3 summarizes the data set for the analysis.

2.6.1 Signal Processing and Trigger Condition

The signals from each detector were process by electronic circuits to deduce the charge, timing and/or multiplicity information. The signal processing for GRAPE has been described in Sec. 2.4.4. In this section, the signal processings for the plastic scintillation counter for the beam monitor, PPACs and hodoscope, and the trigger for the data acquisition are described.

Figure 2.12 shows the circuit diagram for the signal processing of the plastic scintillation counters. The diagram applies to the two plastic scintillation counters at F2 and F3 excluding the circuit for the trigger signals. The signal from the PMT attached to the plastics scintillation counter was divided into two signals. One signal was delayed and digitized by a charge-sensitive analog-to-digital converter (QDC) to deduce the energy deposited in the plastic scintillators. The other signal was connected to a leading-edge discriminator, which output the logic signal when the amplitude of the signal was higher than the threshold. The logic signal was used for the stop signal of the time-to-digital converter (TDC) and the trigger for the data acquisition.

The logical *AND* of two logic signals from the PMTs attached to the left (L) and right (R) sides of plastic scintillation counter was prepared as *BEAM* signal and the timing of this signal was decided by that of the left PMT (PL-L). The *BEAM* signal was used for the logical *AND* with the signals from the other detectors to identify that the reaction was induced by the secondary reaction. The *BEAM* signal was thinned out by four orders of magnitude making *DSBEAM* signal as a trigger to check the beam profiles during the experiment. The

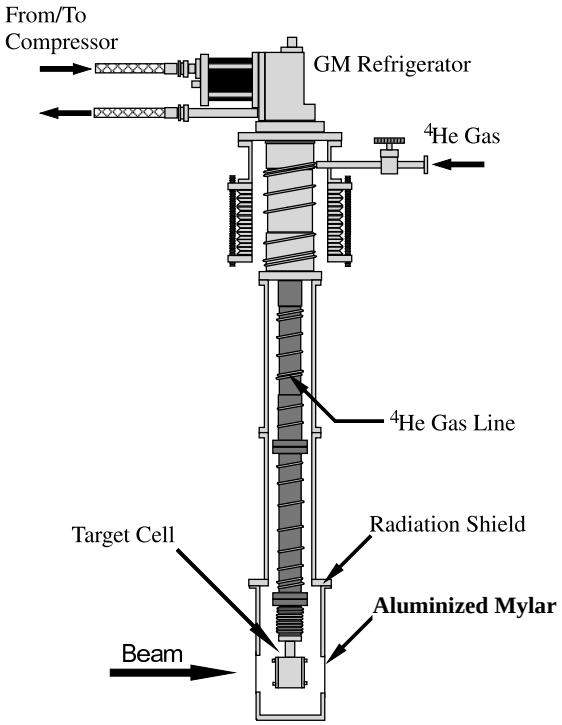

(a) Schematic view of the liquid helium target system

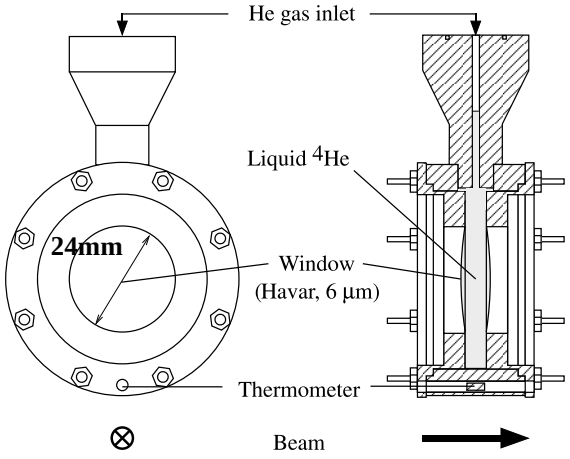

(b) Schematic view of the target cell

Figure 2.11: Schematic view of the liquid target system and target cell.

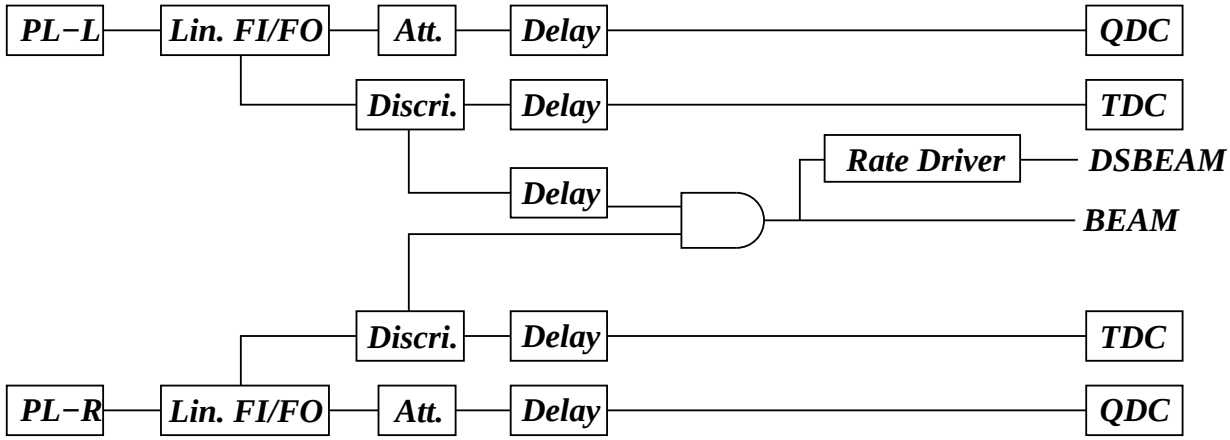

Figure 2.12: Electronic circuit diagram for beam counter. The signal from a PMT was divided into signals for charge and timing information. Both signals were delayed and digitized by CAMAC modules. Logical *AND* of two timings from the PMTs attached to the left (L) and right (R) side of the plastic scintillator was made for the BEAM signal. The time was determined by the timing of PL-L. The BEAM signal was thinned out to make a DSBEAM signal, that was a factor of 10^{-4} compared to the rate of the BEAM signal. The circuits for the plastic scintillators at F2 and F3 were same, except for the circuit for the trigger.

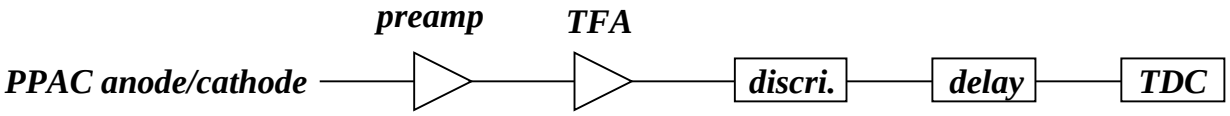

Figure 2.13: Electronic circuit diagram for the PPACs. The signals from the cathodes and anode of a PPAC were pre-amplified and the timing was picked off by a TFA. The timing signals were generated by leading-edge discriminators and digitized by TDCs.

pileup after a signal was killed by the precursory signal and the signal itself was register to the event data in order to kill the data triggered by the precursory signal.

Figure 2.13 shows the electronic circuit diagram for PPAC. The signals from the cathodes and anode, in total five signals per PPAC, were amplified by the pre-amplifiers located as close to the PPAC as possible in order to improve the signal-to-noise ratio. The timing of pre-amplified signals was picked up by the timing-filtering amplifiers (TFA), and the timing signals were picked off by discriminators and digitized by TDCs.

The electronic circuit diagram for outgoing reaction products is shown in Fig. 2.14. Two signals were extracted from the photomultiplier tubes attached to the both ends of each plastic scintillation bar. One signal was attenuated and delayed to be in the integration window of Fast Encoding and Reading Analog-to-digital converter (FERA) module, in order

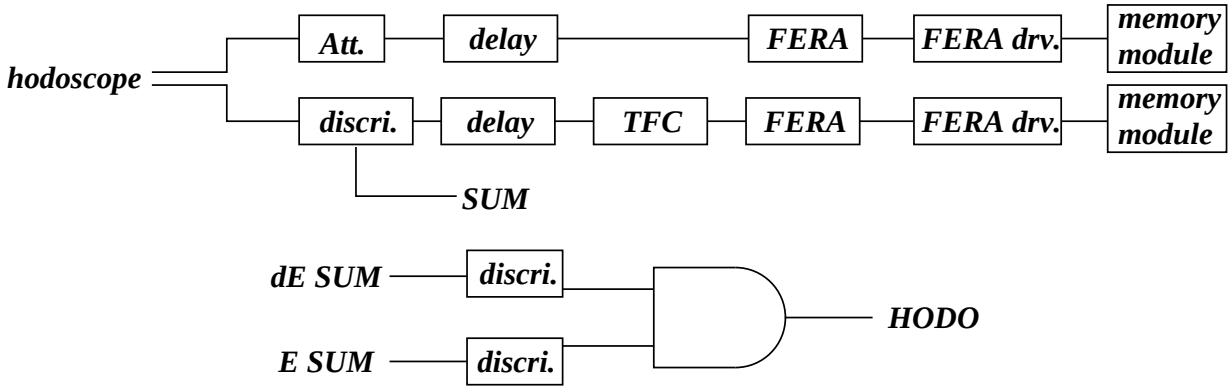

Figure 2.14: Electronic circuit diagram for the hodoscope. Two signals are extracted from each photomultiplier tube attached to both ends of each plastic scintillation bar. One signal is integrated and digitized by FERA module to deduce the energy deposition in each bar, and the timing of the other is picked off by the discriminator and digitized by a TFC-FERA combination. The signals are summed, and the multiplicity in each bar is extracted from the discrimination of them. The multiplicity signal is used for the requirement of the reaction product.

to deduce the energy deposited in each bar. The digitized data was read into a memory module via FERA bus managed by a driver module (FERA driver). The other signal was discriminated and delayed. The time difference from the trigger timing was converted to the corresponding charge by time-to-charge converter (TFC) module. The converted charge was integrated by FERA module and the digitized data was stored into the other memory module.

The timing signals from the bars in ΔE- and E-layers were summed and the multiplicity in each layer was obtained by discriminating the height of the summed signal. At least two hits, *i.e.* both signals from a single scintillation bar, in each layer was required. Although the multiplicity signal was logical *OR* rather than the signal consisting of logical *AND* processing, the multiplicity signal was used as the requirement of at least one scintillation bar firing since both signals from two PMTs were coincident and the signal-to-noise ratio was good enough in the energy region of interest corresponding to the energy deposited by the ^{12}Be or ^{13}B nuclei.

The trigger for the data acquisition consisted of two signals. One is the *DSBEAM* signal, described above for monitoring the beam profile during the experiment. The other is a logical *AND* between the *BEAM*, *GRAPE*, and *HODO* signals (*COIN*) to require the nuclear reaction accompanied by de-excitation γ rays. The timing of the trigger was determined by the *BEAM* signal. Typical rates of the *COIN* and *DSBEAM* trigger were 10^3 and 2×10^2 Hz, respectively.

2.6.2 Data Acquisition System

The digitized data were read out and stored into data storage by a data acquisition (DAQ) system, "babarl DAQ", consisting of two general purpose computers connected over Ethernet. Each computer concentrated on a specified function to reduce the dead time of the system. One computer (*collector*) read out the data from CAMAC and VME modules and sent the data to the other one (*recorder*). Then the *recorder* wrote the data to the magnetic tape storage. Furthermore, the *collector* had two buffers to store the data in an effective manner, *i.e.* when one buffer was full, the data stored in the other, to reduce the dead time of the system due to the delay by the overhead of the network communication. The operating system of the *collector* was a real-time Linux system to guarantee that the response time was within a specified duration, *e.g.* 50 μs for the present DAQ system. The *collector* checked the CAMAC LAM signal every 50 μs to start acquisition. The order of the reading of the modules was scheduled so as to read the data after the end of conversion.

2.6.3 Data Sets

Experimental data were taken under several different conditions as summarized in Table 2.2. The principle data for single-proton transfer reaction were taken with the liquid ^{4}He target. Data with empty target cell runs were taken to estimate the contribution from scattering with non-α materials.

Sets of data were obtained for each conditions by applying both the *BEAM* and *COIN* trigger conditions. Also data for the detector calibration were taken using beam of ^{12,13,14}B and ^{12}Be.

Beam	target/source	trigger
^{12}Be 50 AMeV	liquid helium	$COIN \oplus DSBEAM$
^{12}Be 50 AMeV	target cell w/o helium	$DSBEAM$
^{12}Be 50 AMeV	none	$DSBEAM$
^{12}B 50 AMeV	none	$DSBEAM$
^{13}B 40 AMeV	none	$DSBEAM$
^{14}B 50 AMeV	none	$DSBEAM$
^{15}B 60 AMeV	none	$DSBEAM$
^{16}B 50 AMeV	none	$DSBEAM$
none	^{60}Co	$GRAPE$
none	^{137}Cs	$GRAPE$
none	^{152}Eu	$GRAPE$
none	none	$GRAPE$

Table 2.2: List of the data set for the analysis. The set is divided into four groups by the type of measurement: the measurement of the transfer reaction, target thickness, the timing calibration of beam-line counters, and the energy calibration of GRAPE.

Chapter 3

Data analysis

3.1 Overview

The goal of the analysis is to deduce the transferred angular momentum in the proton transfer reaction and to determine the spin and spectroscopic strength of each excited state in ^{13}B The analysis consists of three parts, as explained below.

1. Selection of ^{4}He(^{12}Be,^{13}B) reaction channel
In the first part of this chapter, the analysis procedure to select the reaction channels and to find 'good' (^{12}Be,^{13}B) events will be described. The timing measured with TDC modules is calibrated and the walk of the timing originating from the pulse shape and height is corrected. In order to select the reaction channel, the incident and outgoing particles are identified on an event-by-event basis. The incident particles are identified using the timing information measured with F2PL and F3PL, and the energy deposition measured with F3PL. The outgoing particles are identified using the timing information measured with F2PL, F3PL and hodoscope, and the energy deposited in the ΔE and E layer of the hodoscope. The trajectory of the incident particle was deduced by using the PPACs located at F3. The timing information of the PPACs is also used for the single hit event selection to eliminate pileup events.

2. Deduction of the γ-ray yield and the angular distribution
In the second part, the analysis procedure to obtain the Doppler-shift corrected γ-ray energy spectrum, the γ-ray yields and the angular differential cross section to each excited state is described. The pulse height information measured with V785 ADC modules is calibrated using the experimental data taken with standard sources. The Doppler shift of the γ-ray energy is corrected by the combination of the γ-ray detection position deduced from pulse-shape analysis with the the scattering angle and velocity of the outgoing particle deduced using the method detailed in the previous part. The resultant γ-ray energy spectrum is decomposed to response functions and backgrounds to obtain the γ-ray yield for each

population of the excited state. The angular differential cross sections are deduced from the decomposition analysis of the γ-ray energy spectrum in combination with the angular information of the outgoing particles.

3. Deduction of the transferred angular momentum and spectroscopic strength for each excited state
In the last part, the analysis of the angular differential cross sections using distorted wave Born approximation will be described. The transferred angular momentum and the spectroscopic strength are deduced from the DWBA analysis using the phenomenological optical potentials and the optical potential obtained based on the single-folding model.

3.2 Time calibrations

In this section, a common procedure used for the calibration of the timing information measured with TDC modules is described. All the channels of TDC modules are calibrated using a time calibration module. The time calibration module generates start and stop signal. The stop signal is randomly generated in a certain period, which is set to 20 ns in the present study. Figure 3.1 shows a typical example of the time calibration, which is for the timing signal of RF. In Fig. 3.1(a) and (b), the obtained time spectrum and the result of fitting, respectively, are shown. A set of the mean values of peaks in Fig. 3.1(a) is fitted with a linear function. In Fig. 3.1(c), differences of the experimental data from the linear function are shown. As shown in this figure, the differences become larger in the lower and upper channel region, which is the so called 'integral non-linearity'. To correcting the integral non-linearity, the data set is fitted with a spline curve rather than the linear function. The curves in Fig. 3.1(c) indicates the deviation of the spline from the linear function. The curve well reproduces the deviation of the experimental data, so the spline is chosen as a calibration function for the present calibrations.

3.2.1 Walk correction for the plastic scintillators and Germanium detectors

The walk effect [59] in the timing information of F2PL and F3PL should be corrected in order to achieve intrinsic timing resolutions. The leading edge timing of a pulse shape $V(t)$ is approximated by a parabolic function of time t as follows,

$$V(t) = A(t - t_0)^2, \tag{3.1}$$

where t_0 and A are the time of initial rise, *i.e.* the detection timing, and the pulse height of the signals, respectively. From this equation, the measured timing t is obtained as follows,

$$t = t_0 + \frac{sqrtV(t)}{\sqrt{A}}. \tag{3.2}$$

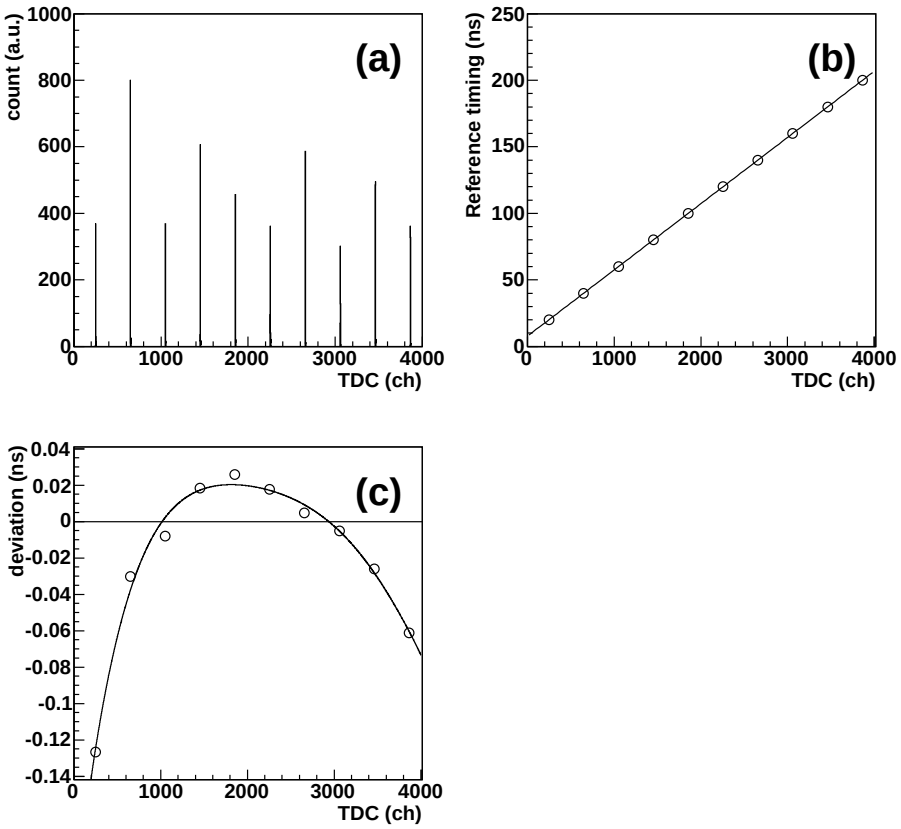

Figure 3.1: Typical example of time calibration using a time calibration module. This is the case of the TDC for the time signal of RF. Figure (a) shows a time spectrum obtained the time calibrator with the time period 20 ns. Figure (b) shows a result of the fitting a linear function to the spectrum. Figure (c) shows deviations from the linear function. Curve shows deviations of the spline fitted to the experimental spectrum from the linear function. See text for details.

The second term represents the difference from the timing when the particles reach at the detector. Since the threshold has been set to V_{thres} the correction term depends on only the pulse height. Finally the walk-corrected timing T can be obtained by subtracting the walk effect from the calibrated TDC value T_{TDC},

$$t = t_{TDC} - \frac{\sqrt{V_{thres}}}{\sqrt{A}}. \tag{3.3}$$

The parameter of V_{thres} is obtained by fitting the eq. 3.3 to the experimental data.

The timing signal of the plastic scintillator hodoscope and Germanium detectors are also affected by walk. For these detectors, the empirical equation similar to Eq. (3.3) was used:

$$T = T_{TDC} - \frac{\sqrt{V_{thres}}}{A^b}, \tag{3.4}$$

where b is a multiplier factor for the pulse height A. The parameters of V_{thres} and b were determined by fitting these equation to the experimental data set. For the hodoscope, the parameters are obtained by fitting the eq. 3.4 to the data set with the calibration beams of ^{12,13,14}B. The timing resolutions of ΔE- and E-layers of hodoscope and GRAPE after the time walk correction were 121 ps, 106 ps, and ∼5 ns in one standard deviation

3.3 Analysis of incident particle

This section describes analysis procedure for the incident particles. The incident particle is identified by using the information on the energy deposition (ΔE) and the time-of-flight (TOF) measured with two plastic scintillators, F2PL and F3PL. The direction and position of incident particle on the target was measured by two PPAC's.

3.3.1 Identification of incident particles

The ^{12}Be particles were discriminated from beam contaminants on an event-by-event basis by means of the TOF-ΔE method. The TOF is measured along the flight path of 5.4 m between F2PL and F3PL. The resolution of the TOF was deduced to be 117±1 ps (one standard deviation) by using beam calibration run of ^{13}B beam of 50 AMeV with 0.2 % momentum uncertainty. Figure 3.2 shows a two dimensional plot of TOF vs. the energy deposited in the log scale. In the figure, the rectangular region corresponding to the ^{12}Be beam used for the present analysis, is also shown. The region includes 2 % of the contaminant ^{9}Li; however, the contaminant is unimportant since the probability of the fusion reaction at 50 AMeV is negligible small. The events in the region above the 300 ch of ΔE was pile up events. From the other contaminants, the ^{12}Be beam was discriminated clearly. The ratio of secondary beam ^{12}Be in the gate to the total was 80%.

3.3.2 Beam profile

As described in Sect. 2.3.2, each PPAC(A and B) had two cathodes, which provided vertical and horizontal position information. Each cathode had two electrodes at both ends of the delay line. The position information, e.g. X for horizontal position, was deduced from the timing information from the two electrodes, as

$$X = c \times (T_1 - T_2 + T_{offset}) + X_{offset}(\mathrm{mm}), \tag{3.5}$$

where $T_{1,2}$ are the timing information. A conversion factor from time difference to the length c is typically about 0.63 mm/ns, and was measured precisely when the PPACs were fabricated. T_{offset} and X_{offset} are constants for the corrections. The former is the correction for the difference of cable lengths inside detector, which is inherent to each PPAC, and was

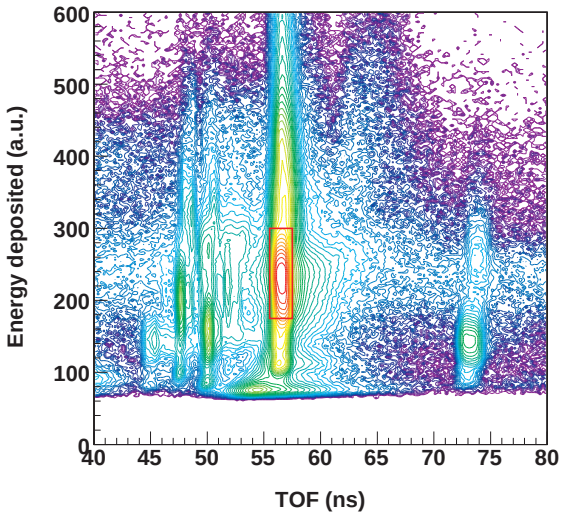

Figure 3.2: A two dimensional plot of the TOF and energy deposited for the identification of incident particles. A box indicates the selected region for ^{12}Be.

measured in advance when the PPAC was produced. The latter includes two corrections: one for the difference of cable lengths outside detector and the other for the detector geometry. This correction was deduced by using experimental data from runs without the target.

Single-hit event selection

In order to avoid incorrect extraction of the position, the selection of single-hit events was performed. In the single-hit event, a sum of two timing (T_1 and T_2) should be constant corresponding to the length of the delay line. By using this feature, we selected a certain period of ($T_1 + T_2$) for each cathode of all the PPAC's to exclude multi-hit events. The sums of ($T_1 + T_2$) are shown in Fig. 3.3, which were obtained for PPACa horizontal cathode (a) and vertical cathode (b) with the ^{12}Be beam. A peak observed in each spectrum corresponds to single hit events, while the events having a smaller timing sum show up as multi-hit events. The data processing windows adopted as corresponding to single-hit events are also indicated in Fig. 3.3. The widths correspond to the $\pm 4\sigma$-region were obtained by fitting a Gaussian function to the peak areas.

Detection and Tracking Efficiency

Detection efficiency of PPAC's were estimated by analyzing the experimental data of ^{12}Be beam trigger, $DSBEAM$. Single-hit events for both X and Y cathodes of each PPAC were selected. The efficiencies of PPAC's are extracted from the number of counts of X and Y as

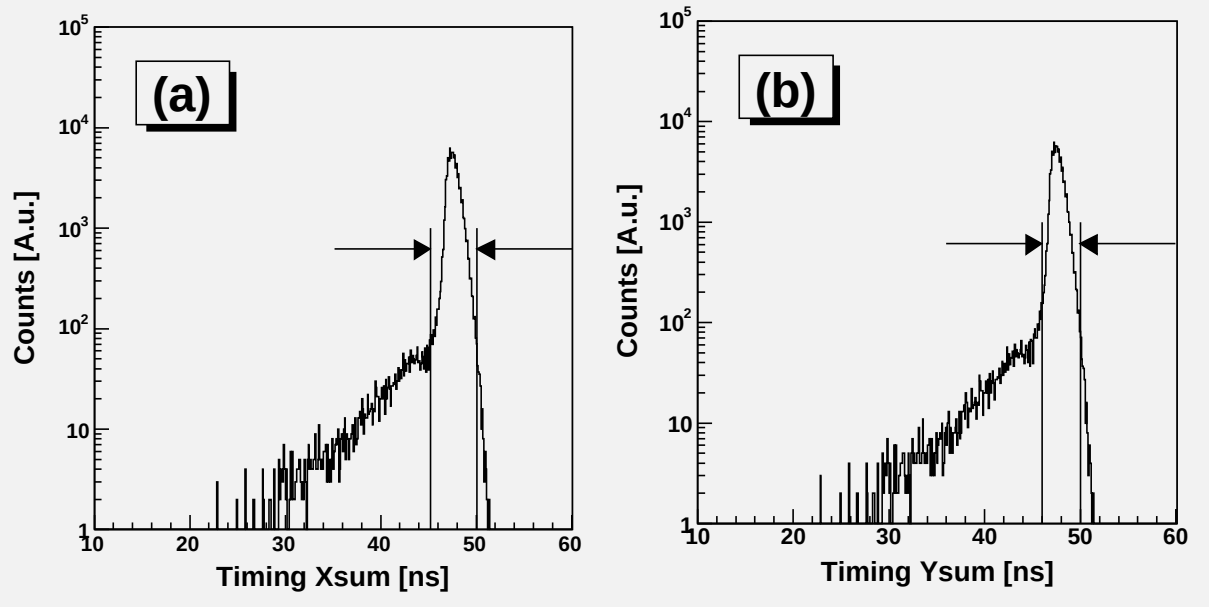

Figure 3.3: Spectra of the average of timing $((T_1+T_2)/2)$ of both electrodes attached to X and Y cathode of F3PPACa. Single hit event constitute a peak around 45–50 ns, while multi hit events exhibit smaller sum. The selected single hit events are indicated by the arrows in the figure.

below[55]:

$$\eta_X = \frac{N_X}{N_{^{12}\mathrm{Be}}} \tag{3.6}$$

$$\eta_Y = \frac{N_Y}{N_{^{12}\mathrm{Be}}} \tag{3.7}$$

$$\epsilon = \frac{N_X \otimes N_Y}{N_{^{12}\mathrm{Be}}}, \tag{3.8}$$

where $\eta_{X(Y)}$ and ϵ denote the detection efficiency of $X(Y)$ cathode and the detection efficiency of one PPAC, respectively. N_X, N_Y and $N_X \otimes N_Y$ denote the number of counts of X cathode, Y cathode and coincidences of them for ^{12}Be beam, whose number of counts is denoted as $N_{^{12}Be}$. The obtained efficiencies are listed in Table 3.1. Tracking efficiency of PPAC's was also extracted to be 75% under the condition that all cathodes of two PPAC's registered a single hit.

Position and Angular resolutions

A scattering angle of an ejectile and an emission angle for a γ-ray were provided by position information of PPAC's and plastic scintillator hodoscope. Thus, the position resolution

	F3PPACa	F3PPACb
$\eta_X(\%)$	92.6	92.5
$\eta_Y(\%)$	92.9	93.0
$\epsilon(\%)$	86.3	86.2

Table 3.1: The detection efficiencies of PPAC's.

determines the angular resolution of incident and scattering angles and γ-ray energy. We evaluate the intrinsic position resolution of PPAC, and the position resolution at the target place.

Considering the propagation of errors, the position resolution was deduced as below:

$$
\begin{aligned}
T_{diff} &\equiv \frac{T_{X1} - T_{X2}}{2} && (3.9)\\
T_X &\equiv \frac{T_{X1} + T_{X2}}{2} && (3.10)\\
(\delta T_{diff})^2 &= \frac{(\delta T_{X1})^2 + (\delta T_{X2})^2}{2} && (3.11)\\
&= (\delta T_X)^2 && (3.12)\\
\delta X &= c \times 2\delta T_{diff} && (3.13)\\
&= c \times 2\delta T_X, && (3.14)
\end{aligned}
$$

where the T_{X1} and T_{X2} are the timings from the both end of the delay line X. The resolution of $T_{X(Y)}$ was deduced from a set of equations below,

$$
\begin{aligned}
\delta T_{F2-F3} &= \sqrt{(\delta F2T)^2 + (\delta F3T)^2 + (\delta TOF_{F2-F3})^2} && (3.15)\\
\delta T_{F2-F3a} &= \sqrt{(\delta F2T)^2 + (\delta F3aT)^2 + (\delta TOF_{F2-F3a})^2} && (3.16)\\
\delta T_{F2-F3b} &= \sqrt{(\delta F2T)^2 + (\delta F3bT)^2 + (\delta TOF_{F2-F3b})^2} && (3.17)\\
\delta T_{F3-F3a} &= \sqrt{(\delta F3T)^2 + (\delta F3aT)^2 + (\delta TOF_{F3-F3a})^2} && (3.18)\\
\delta T_{F3-F3b} &= \sqrt{(\delta F3T)^2 + (\delta F3bT)^2 + (\delta TOF_{F3-F3b})^2} && (3.19)\\
\delta T_{F3a-F3b} &= \sqrt{(\delta F3aT)^2 + (\delta F3bT)^2 + (\delta TOF_{F3a-F3b})^2} && (3.20)\\
\delta T_{F3a(b)_{X(Y)}-F3a(b)} &= \sqrt{(\delta F3a(b)T_{X(Y)})^2 + (\delta F3a(b))^2}, && (3.21)
\end{aligned}
$$

where $F2$, $F3$, and $F3a(b)$ represent F2PL, F3PL, and F3PPACa(b), respectively. $F2T$ is the timing of F2PL and so are $F3T$ and $F3a(b)T$. The values of δTOF_i are calculated with an assumption of the uniform distribution of $\Delta p/p = 0.2\%$, taking account for the energy loss in materials plated in the beam line. The set of equations is redundant so that 3 different solutions for $\delta F2T$, $\delta F3T$ and $\delta F3a(b)T$ were obtained. An average of 3 solutions was taken as the timing resolution. The obtained values are listed Table 3.2. The resolution of

	$\delta F2T$	$\delta F3T$	$\delta F3aT$	$\delta F3bT$
σ(ps)	65.3	98.8	276	281

Table 3.2: The list of time resolutions of plastic scintillators and anodes in PPAC's.

	F3PPACa	F3PPACb	
δX (mm)	0.97	0.53	(FWHM)
δY (mm)	0.85	0.54	(FWHM)

Table 3.3: The list of timing and position resolutions of cathodes in PPAC's.

TOF(F2-F3), calculated to be 118 ps (σ) by using the values listed in Table 3.2, is consistent with the values obtained in analysis on the plastic scintillators (3.3.1). The time and position resolution of each cathode were obtained by combining the obtained time resolution of the anode and Eq. (3.21).

The position resolution at the target was calculated as below:

$$X_{tgt} = \frac{l+L}{l} X_{F3PPACb} - \frac{L}{l} X_{F3PPACa} \tag{3.22}$$

$$(\delta X_{tgt})^2 = \left(\frac{l+L}{l}\right)^2 (\delta X_{F3PPACb})^2 + \left(\frac{L}{l}\right)^2 (\delta X_{F3PPACa})^2, \tag{3.23}$$

where l is the distance between F3PPACa and F3PPACb and L is the distance between F3PPACb and the secondary target. The deduced horizontal and vertical position resolution was 7.3 mm (FWHM) and 4.3 mm (FWHM), respectively.

The angular resolution for incident beam particles was calculated as below:

$$X' = \arctan\left(\frac{X_b - X_a}{l}\right) \tag{3.24}$$

$$(\delta X')^2 = \left(\frac{1}{l(1+\{(X_b-X_a)/l\}^2)}\right)^2 \left\{(\delta X_b)^2 + (\delta X_a)^2\right\}, \tag{3.25}$$

where X' is the incident angle, X_a and X_b are the position on F3PPACa and F3PPACb, respectively, and l is the distance between F3PPACa and F3PPACb. The deduced horizontal and vertical angular resolution were 3.7 mrad (FWHM) and 3.4 mrad (FWHM) at forward angle.

Emittance of incident beam particles

Positions measured by one pair of PPAC, F3PPACa and -b, were employed to deduce the angles and positions of incident beam particles on the secondary target on an event by event

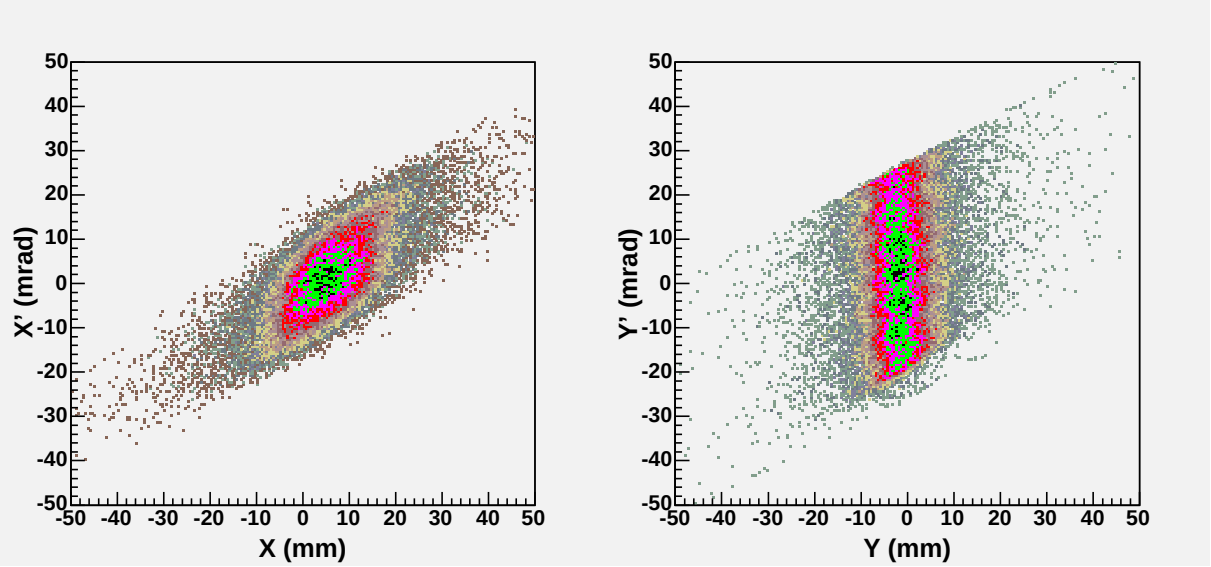

Figure 3.4: Beam spot size and incident angles of the ^{12}Be beam at the secondary target for the horizontal (left) and vertical (right) directions. The plot was made by extrapolation of the position information obtained by PPAC's.

basis. The angle of the incident particle is defined in Eq. (3.24). Figure 3.4 shows two dimensional plots between the positions and angles of the incident particles at the secondary target position. The plots show a rather incomplete focus of the beam in the vertical direction compared with the horizontal focus. In this experiment, the final focal plane was changed downstream by about 1 m compared with the standard F3 position so that the vertical focus was poor. Some of the beam particles which are out of the effective areas of PPACs have not been measured due to the poor focus, and thus the resultant emittance seems to be cut, as shown in the right of Fig. 3.4. Nevertheless, the spot size 8.5 $\times$ 5.7 mm^2 in r.m.s was sufficiently small compared to the target size of 24 mm-diameter.

The angular spread of the beam was 8.3 mrad and 13.17 mrad in r.m.s. for horizontal and vertical directions, respectively. These values are smaller than the angular acceptance of the plastic scintillator hodoscope placed after the target.

3.3.3 Target position

Position of the secondary target in the plain perpendicular to the beam axis was confirmed by using a defocused beam. Figure 3.5(a) shows the scatter plot for the position distribution at the secondary target with the condition of the hodoscope firing, which is extrapolated using the position measured with PPACs. Since the length of the target cell was long enough to stop the incident particles, the intensities at the position corresponding to the target cell are very few. The position distribution normalized by the unbiased position distribution of

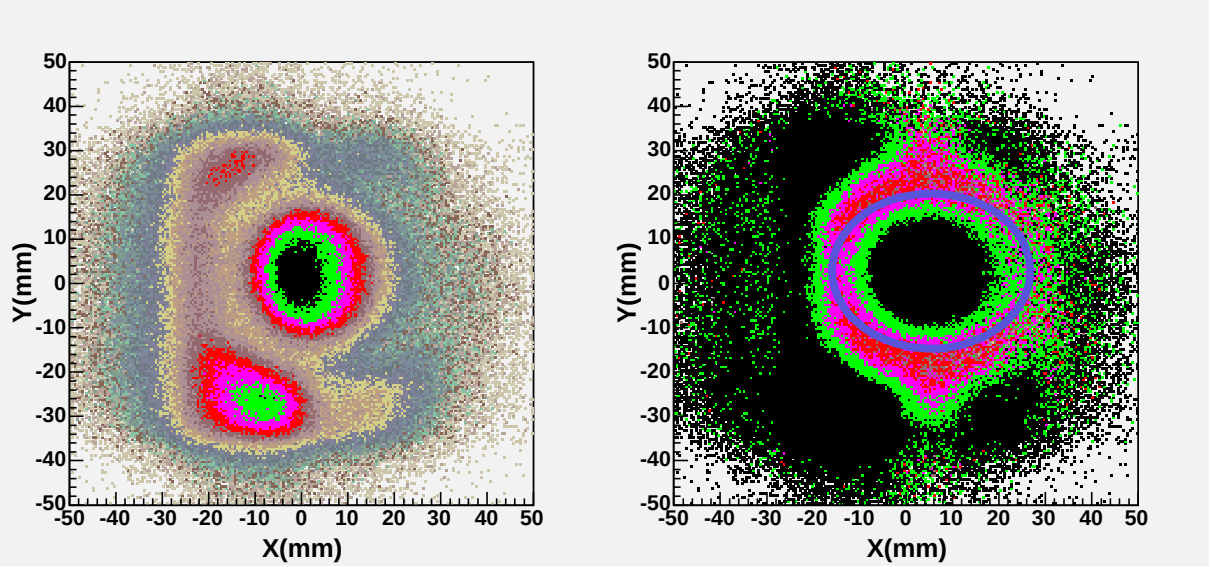

Figure 3.5: Position distribution of the defocused beam at the secondary target plane under the condition that the particles arrived at plastic scintillator hodoscope. The left one shows a raw distribution and right one shows the normalized one. An ellipse indicates the selected region for ^{12}Be which bombarded the liquid helium target.

the incident beam is shown in Fig. 3.5(b). The shape of the target cell is clearly seen in the figure. The position of the secondary target was deduced by fitting Gaussian function to the projection of the distribution. The position of the secondary target was checked twice, at the beginning of the anterior half and the last half of the experiment.

3.3.4 Transmission

The transmission of the beam from the F3PL to the hodoscope was estimated from the comparison of the number of counts of the particles which hit two PPACs and bombarded the liquid helium target for the events taken under $DSBEAM$ trigger. The bombarded region was defined as below:

$$\frac{(X-\bar{X})^2}{(R+3\sigma_X)^2}+\frac{(Y-\bar{Y})^2}{(R+3\sigma_Y)^2}\leq 1, \tag{3.26}$$

where $X(Y)$ and $\sigma_{X(Y)}$ denote the extrapolated position and its resolution at the secondary target, R denotes the radius of the window of the secondary target, $\bar{X}(\bar{Y})$ denotes the position of the secondary target, described in Sec. 3.3.3. The selected region for the particles bombarding the secondary target is indicated by an ellipse in Fig. 3.5. The incident particles which bombarded the helium target rather than the target cell, were 94% of the total incident particles.

3.4 Analysis of Outgoing Particles

This section describes analysis procedure for the outgoing particles. In this experiment, not only ^{13}B, which was physical interest, but also other various nuclei were made via reactions on the secondary target. We need to identify the outgoing particles to investigate the nature of ^{13}B and to distinguish non-^{13}B events. The identification of the outgoing particles were performed by combination of the ΔE-E-TOF information, which were provided by the plastic scintillator hodoscope.

The scattering angle was deduced from the position of the outgoing particle at the hodoscope, in combination with the position information of PPACs. The position of the outgoing particle was measured with the hodoscope.

For the Doppler correction, velocity (β) of an outgoing particle was extracted from the timing information of the hodoscope in combination with the time-of-flight between F2 and F3, measured with plastic scintillators at F2 and F3 (see Sec. 2.3).

In the analysis, the number of the outgoing particles detected in the hodoscope is limited to be one in order to select a two-body reaction.

3.4.1 Identification of Atomic Number

The atomic number Z of the outgoing particle was identified by using a combination of the energy loss in the ΔE plastic scintillator bar and the TOF between the secondary target and the E plastic scintillator bar. The ΔE depends on Z and the velocity β of a reaction product and the relation can be written as

$$\Delta E \propto \frac{Z^2}{\beta^2}. \tag{3.27}$$

The TOF is proportional to β, therefore Z can be determined by combination of the ΔE and TOF information. Figure 3.6(a) shows a typical correlation between ΔE and TOF. For an easy selection, Z was calculated by using the information of ΔE and TOF as below.

$$Z \propto \Delta E \cdot \beta. \tag{3.28}$$

The distribution of Z is shown in Fig. 3.6(b). The boron isotopes ($Z = 5$) are clearly discriminated from the other isotopes. The window from $Z = 4.5$ to $Z = 5.5$ is chosen for the analysis of the proton transfer reaction.

3.4.2 Identification of Mass Number

The mass number A of the outgoing particle was identified by using a combination of the energy loss in the E plastic scintillator bar and the TOF between the secondary target and the E plastic scintillator bar. The outgoing particle stops in the E bar, hence the E is close

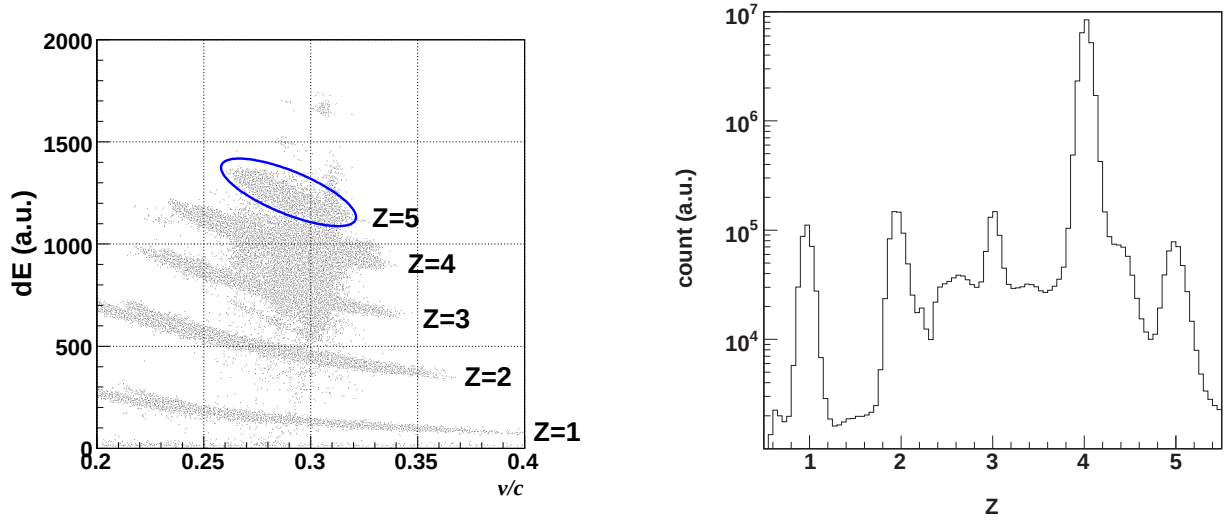

(a) velocity vs energy deposition (b) atomic number distribution

Figure 3.6: (a) Correlation between velocity and energy deposition in ΔE plastic scintillators of outgoing particles. The velocity is extracted from the TOF between the F2 and F3 and the one between the F3 and plastic scintillator hodoscope. (b) Atomic number distribution of outgoing particles is deduced from the correlation between the velocity and energy deposition by using Eq. (3.28).

to kinetic energy. The relation between the velocity β, the A, and the kinetic energy, *i.e.* E is approximately to be,

$$E \propto A\beta^2. \tag{3.29}$$

The TOF is proportional to β, therefore A can be determined by combination of the E and TOF information. Figure 3.6(a) shows a typical correlation between E and TOF for the atomic number region from $Z = 4.5$ to $Z = 5.5$[1], corresponding to boron isotopes. For an easy selection, A was projected along the direction indicated in Fig. 3.6(a). The obtained distribution of A is shown in Fig. 3.7(b). A peak corresponding to ^{13}B ($A = 13$) is clearly discriminated from the neighbor peak. Assuming the Gaussian distribution for each A peak, a typical resolution was 0.25 in the mass number unit, hence the peaks are separated from their neighbors by 4σ.

[1]The atomic number Z is always physically an integer value. However, due to the experimental uncertainties particles appear to have non-integer atomic numbers

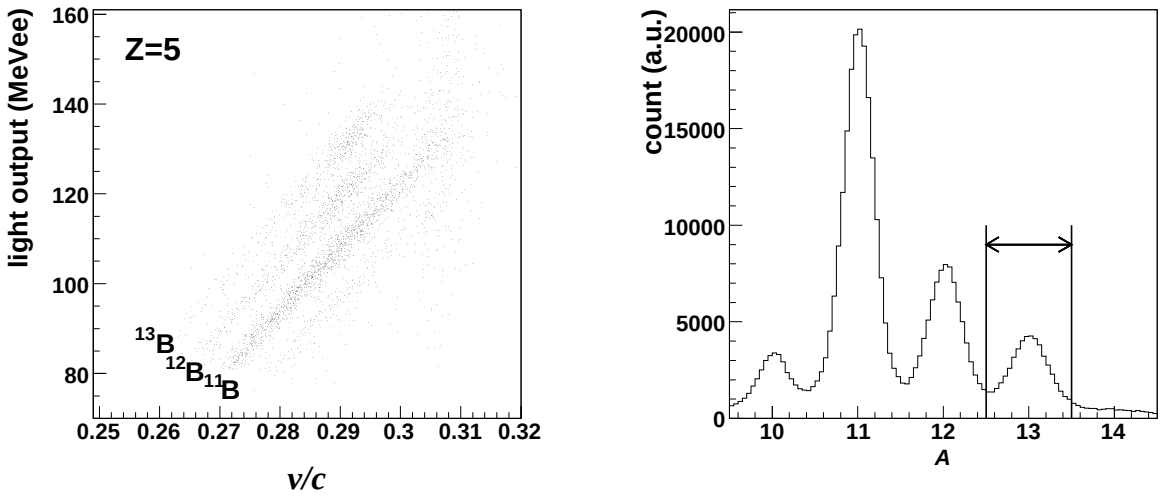

(a) velocity vs light output (b) mass distribution for $Z = 5$

Figure 3.7: (a) Correlation between velocity and energy deposition in E plastic scintillators of outgoing particles. The velocity is extracted from the TOF between F2 and F3, and from F3 to the plastic scintillator hodoscope. (b) Mass number distribution of outgoing boron isotopes is deduced from the correlation between the velocity and energy deposition by using Eq. (3.29).

3.4.3 Position of Outgoing Particles

The position information of the outgoing particle is extracted from the time difference between signals of two photo-multiplier tubes attached to both ends of each plastic scintillation bar. The horizontal (X) and vertical (Y) position is deduced by using ΔE and E bars, respectively, from the formula below,

$$X = (T_1 - T_2 - c_1)/c_2 + X_{offset}, \tag{3.30}$$

where $c_{1,2}$ are calibration coefficients for each scintillation bars and X_{offset} is common correction constant for each layer. The calibration coefficient is deduced from the geometrical relation between ΔE and E bars. A bar in ΔE layer can be divided into 16 sections corresponding to 16 E bars and a bar in E layer can similarly be divided into 13 sections. Focusing on one pair of ΔE and E bars, the time difference of each bar is limited by the width of the paired bar. The position of E bars are well known geometrically. The centroid of the time difference distribution of the ΔE bar, therefore, corresponds to the location of E bar, and the same for the E bar. The centroid is approximately obtained by fitting with a Gaussian distribution. The correlation between the centroids and locations is fitted

with a linear function, and then the calibration coefficients $c_{1,2}$ are obtained. The common correction constant is deduced by comparing the position extracted by hodoscope with the position extrapolated by the PPACs. In the run with no secondary target, the trajectory after the last quadruple magnet is straight since the effect of multiple scattering in mylars is ignorable.

3.4.4 Velocity of Outgoing Particles

The velocity of an outgoing particle is deduced from the timing information measured with hodoscope and plastic scintillators at F2 (F2PL) and F3 (F3PL) with a correction for the energy deposited in the secondary target. The timing from the hodoscope is extracted as the average of the two timings $T_{1,2}$ of the fired E bar. The velocity before the correction is calculated from the time-of-flight from the secondary target and the hodoscope $TOF_{Tgt-Hodo}$. The $TOF_{Tgt-Hodo}$ is obtained from the time difference between F3PL and the hodoscope ($TOF_{F3PL-Hodo}$) by subtracting the time-of-flight between F3PL and the secondary target ($TOF_{F3PL-Tgt}$). The $TOF_{F3PL-Tgt}$ is estimated from the time-of-flight between F2PL and F3PL, taking the effect of the energy deposits in the F3PL and PPACs into account. The intrinsic resolution of the velocity is deduced from the experimental data and the resolution to the velocity $\delta\beta/\beta$ is 0.23% (one standard deviation). The calculated velocity is corrected for the energy loss in the secondary target. The correlation is approximated as the second order polynomial. In the correction the reaction position along the beam axis is assumed to be the center of the secondary target. Th effect of the ambiguity of this reaction position to the Doppler correction is discussed in Sec. 2.4.3.

A window was set on difference between the velocities of incident and outgoing particles in order to select the two-body reaction and reduce the background events since there were events where the α particles broke up, rather than the α particles went to the ^{3}H particles. Figure 3.9 shows a scatter plot of the scattering angle of the outgoing particles vs. the difference of the velocities between the incident and outgonig particles. Since the velocities of the ougoing particles depend on the scattering angle of them due to the kimatics, the velocity difference was corrected with a second-order polynomial for the easy selection. The selected region as the two-body reaction events is indicated by two (red) solid lines.

3.4.5 Detection efficiency of Hodoscope

Acceptance of the experimental setup for the scattering particle will be described. The acceptance was simulated including the angular and the position distribution of the incident beam, the size of the target cell and the position resolution of the hodoscope. In the simulation, the acceptance ϵ for a certain angular range between θ_1 and θ_2 was defined as

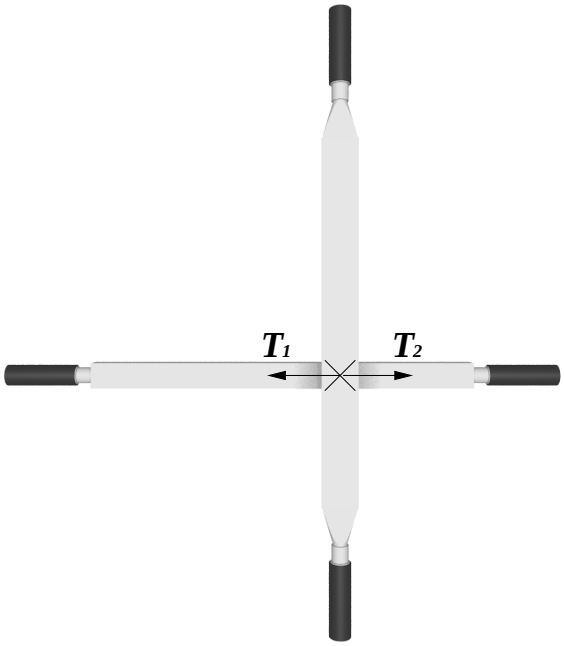

(a) A pair of ΔE and E bars

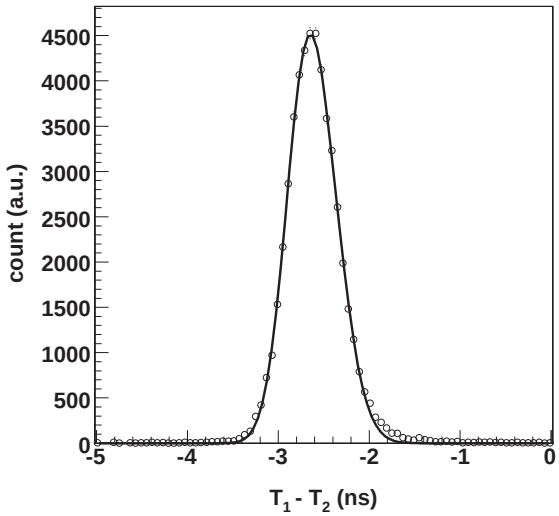

(b) Typical plots of timing difference

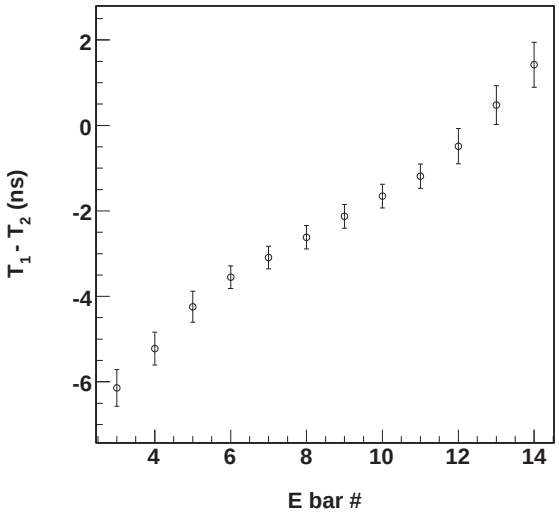

(c) Typical correlation

Figure 3.8: (a) A pair of ΔE and E bars is selected. The emitted light in ΔE bar reaches at the both ends and fires the photo-multiplier tubes. (b) Typical timing difference of ΔE bar in coincidence with certain E bar. The centroid is approximately obtained by fitting with Gauss distribution. (c) Typical correlation between the time difference of ΔE bar and bars in E layer. The horizontal axis is just an ordering of bars, *i.e.*, the time difference is not on a straight line.

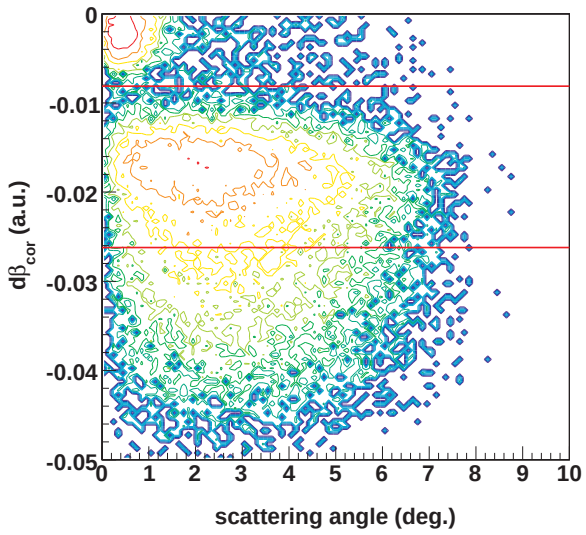

Figure 3.9: Scatter plot of the scattering angle of the outgoing particles vs. the difference between the velocities of incident and outgoing particles. The velocity difference is corrected with a second-order polynomial for the easy cutting. The (red) solid lines show the upper and lower limit for the selection of the two-body reaction.

below:

$$\epsilon_{Acc.} = \frac{N_{measured}}{N_{generated}}, \tag{3.31}$$

where $N_{measured}$ and $N_{generated}$ are the numbers of measured and generated in the angular range, respectively. The simulation procedure is listed below:

- Generate the incident beam with angular and position distribution at the middle of the target. Each distribution was deduced to be approximately a Gaussian distribution from the experimental results.

- Calculate the reaction point with an assumption that the reaction occurs uniformly belong the beam direction. In this step, the horizontal and vertical reaction points are also re-calculated.

- Generate the scattering angle and calculate the momentum vector of a outgoing particle. The scattering angle is generated to be isotropic in center-of-mass frame and converted to one in the laboratory frame with the mean velocity of ∼30% light speed. This assumption works enough to simulate the acceptance. The scattering angle is limited up to 8 degrees.

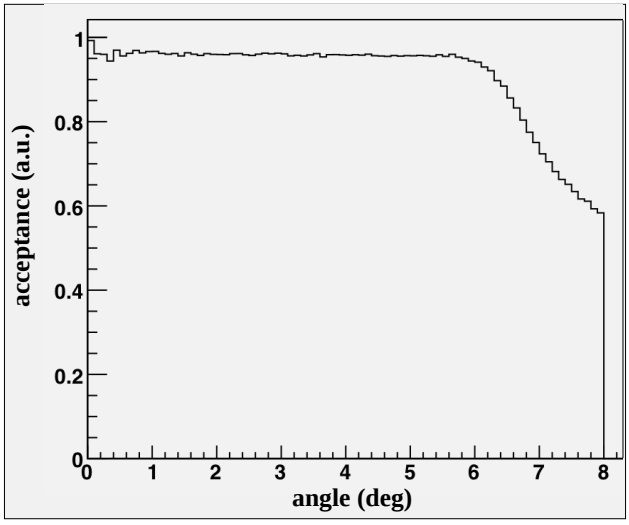

Figure 3.10: Acceptance of the hodoscope deduced from a Monte Carlo simulation. The spacial and angular distribution of incident particle were taken from the experimental data. The count in each bin is divided by the number of generated events corresponding to each bin. The distribution is flat in the angular region below six degrees, which are reduced from unity. The rejected component in flat region, however, has been excluded from the analysis. See the text for the detail.

- Check if the outgoing particle can go out of the target cell.
- Check if the outgoing particle stops in the 400×400 mm^2 rectangle region at the hodoscope. For this check the position resolutions deduced from the experimental data are used.

Figure 3.10 shows the simulated acceptance of hodoscope in the laboratory frame. The count in each bin is divided by the number of generated events. The distribution is flat in the angular region below six degrees, which are reduced from unity, and it decreases in the larger angular region. The rejected component in flat region has been excluded from the analysis, by setting the cut on the spacial distribution as shown in Fig. 3.5. The angular differential cross sections are deduced up to six degrees in the laboratory frame as described in section 3.7.

3.5 Analysis of De-excitation γ Rays

This section describes the analysis of the de-excitation γ rays detected with GRAPE. The energy calibration is done using the experimental data taken with the standard sources (Sec. 3.5.1). To improve signal to noise ratio the timing of the germanium detector is measured

with an ARC method. The walk correction is done in Sec. 3.2.1. The selection of the timing information for the rejection of accidental coincidence event is described in Sec. 3.5.2. The pulse-shape analysis and the Doppler correction of γ-ray energies are described in Sec. 3.5.3 and Sec. 3.5.4, respectively.

3.5.1 Energy Calibration

The energy deposition of the emitted γ ray is obtained by summing the energies deposited in two crystals packed in a detector. The energy deposition in each crystal can be obtained in two ways. One is the add-back of the energies obtained from the cathodes' outputs (digital sum), the other is the energy obtained after correcting the net-charge signal (analog sum). The advantage of the digital sum is better energy resolution, while the one of the analog sum is better full-energy peak efficiency. In the present analysis, the analog sum is chosen since the dominant contribution to the energy resolution for the γ-ray energy after the Doppler-shift correction is not intrinsic energy resolution but the Doppler width. The comparison between the digital and analog sum is described in Appendix B.

The procedure to deduce the analog sum consists of four processes: (1) conversion from channel to energy (usual energy calibration); (2) correction for the gain difference of the pre-amplifiers among the segments; (3) correction for the induced-charge-like effect; (4) correction for the temporal gain drift.

The pulse-height data taken with V785 analog to digital conversion (ADC) modules are calibrated to the reference energies of γ rays emitted from a ^{152}Eu standard source. In the ideal case, since the AD conversion is performed with a linear function, the energy is a linear function of the output channel of the ADC module. In the realistic case, however, a linear function is not suitable for the calibration since the linearity of the V785 module is guaranteed only in the range from 10% to 90% of dynamic range. A parabolic function is usually used as a calibration function since the second-order term acts a correction for the non-linearity. Although the deviation between the calibrated energy and its reference becomes smallest for the interpolation using a parabolic function, the deviation is not trivial for the extrapolation. In the present experiment the dynamic range of the ADC module is set up to 5 MeV while the reference exists at most 1.5 MeV. From this point of view, the discrepancy for the extrapolation with linear function is smaller than that with parabolic function. Hence, the combination of the parabolic and linear functions seems better for the calibration of the present data. The parabolic and linear functions are used for the low and high energy region, respectively. For the analog sum, the hit segment is limited to the segment nearest to the target in order to reject the effect of the gain difference in the analog adder.

The gains of the pre-amplifiers are roughly tuned in the analog adder before summing the segment signals. In this process the gains are precisely tuned not only for single segment

hit but also for many segments hit.

The charge collected by each cathode is added by the analog adder module to form the net-charge signal as below,

$$Q_\Sigma = \sum_{i=1}^{9} \epsilon_i Q_i, \tag{3.32}$$

where Q_Σ and Q_i are the net-charge signal and charge collected by i-th segment, respectively. The coefficient ϵ_i is the total gain factor of the pre-amplifier and analog adder for i-th segment signal. The relation between the real total charge induced in a crystal Q_c and Q_Σ is represented by using eq. (3.32) as below,

$$Q_c = \sum_i Q_i = Q_\Sigma \frac{\sum_i Q_i}{\sum_i \epsilon_i Q_i}. \tag{3.33}$$

As seen in eq. (3.33), the observed charge should be corrected by the charge from each segment in order to obtain the real charge. Since it is difficult to deduce the gain factor ϵ itself, we define the relative gain factor $\epsilon'_i = \frac{\epsilon_i}{\epsilon_6}$, taking the 6-th segment as reference. In fact, the ϵ_6 is already renormalized into the channel-to-energy (charge) conversion function if the function is obtained under the condition that only 6-th segment is hit. By replacing the charge Q by the energy E and using the charge-to-energy conversion function f_i and f_Σ for i-th segment and net-charge signal, respectively, the total energy deposition in a crystal is obtained from eq. (3.33) as below,

$$E_c = E_\Sigma \frac{\sum_i E_i}{\sum_i \epsilon'_i E_i} \tag{3.34}$$

$$= f_\Sigma(N_\Sigma) \frac{\sum_i f_i(N_i)}{\sum_i \epsilon'_i f_i(N_i)}, \tag{3.35}$$

where N_Σ and N_i is the ADC channels for the net-charge and i-th segment signal, respectively. The relative gain coefficient is obtained under the condition that the i-th segment is hit as shown below,

$$\epsilon'_i = \left. \frac{f_\Sigma(N_\Sigma)}{E_c} \right|_{hit=i} \tag{3.36}$$

Even if the E_i is small below the threshold, the total energy E_c contains the information of E_i since the charge from i-th segment is added to the total energy before digitization. On the other hand, the digital sum is smaller by E_i than the true energy deposition. That is why the full-energy-peak efficiency of the analog sum is larger than that of the digital sum.

The induced-charge-like effect is found in the case of two crystals firing in a detector. This effect is corrected by multiplying the obtained energy by a constant, which has been determined by comparing the obtained energy with the γ-ray energy of 1408-keV from the ^{152}Eu standard source. The correction for the temporal drift is performed by also multiplying

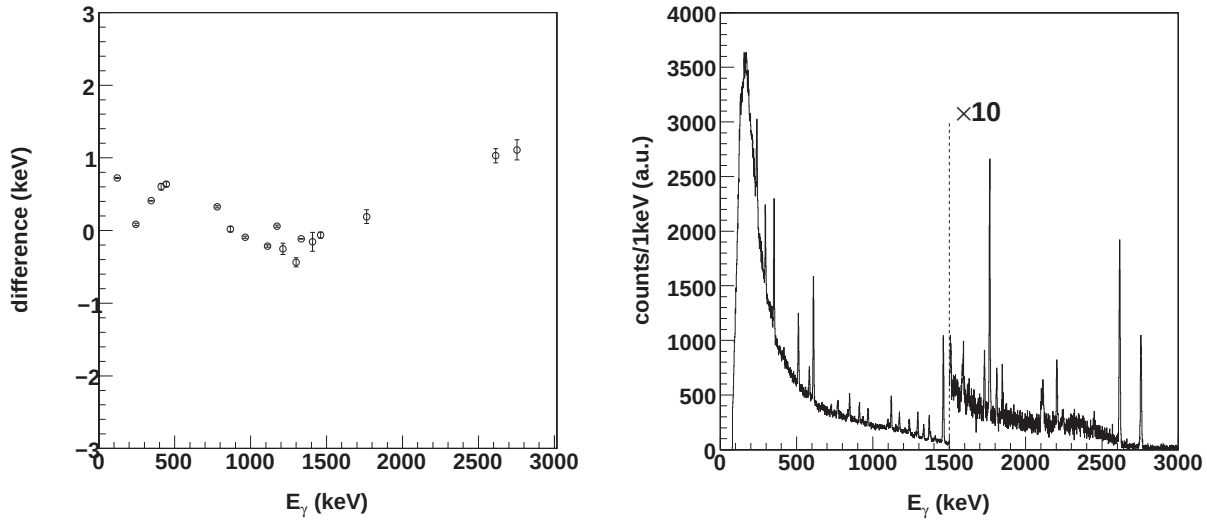

(a) Energy deviation (b) natural background γ rays

Figure 3.11: (a) The energy deviation after the energy calibration of GRAPE. The references are taken from the data with ^{152}Eu, ^{60}Co, ^{137}Cs standard sources and without any source. (b) Background γ-ray energy spectrum. Above 1500 keV, the scale is ten times larger than the one below.

the obtained energy by a constant on an event-by-event basis. All the events are separated into several tens groups based on the event number. The constant has been obtained for each group by referring the 511-keV γ ray.

The deviations between the calibrated energies and their reference are obtained by comparing the calibrated and referred energies taken with ^{152}Eu, ^{60}Co, ^{137}Cs, and without any source, *i.e.* with background γ rays. Figure 3.11 shows (a) the energy deviations and (b) the background γ-ray energy spectrum. The deviations are small enough and within ± 1 keV up to 3 MeV. The energy dependence of the resolution is shown in Fig. 3.12(a). The resolution is not as good as those of other germanium detectors, since noises of segment signals are also added. The contribution of in-phase noises to the analog sum is expected to be nine times larger than to the digital sum, and the contribution of random noises three times larger. However the resolution of around 2.5 keV is good enough to measure the in-flight decay γ rays. The energy dependence is approximated by a empirical function as below,

$$\sigma(E_\gamma) = \sqrt{\sigma_0^2 + \sigma_E E_\gamma}, \tag{3.37}$$

where σ_0 is a constant contribution such as the electric noise of the circuit and the thermal noise in the crystal, σ_E is a energy dependence, and E_γ is the γ-ray energy in MeV. The values of σ_0 and σ_E are 2.35 and 1.32, respectively, were obtained by fitting to the experimental

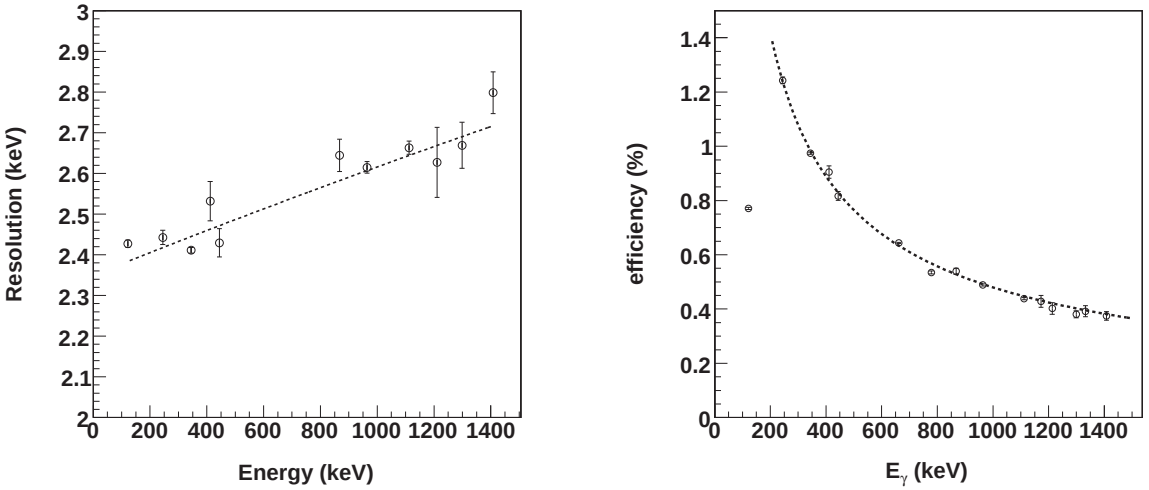

(a) Energy resolution (b) Full-energy-peak efficiency

Figure 3.12: The energy resolution in one standard deviation and full-energy-peak efficiency of GRAPE with statistical errors. The curves show approximate functions.

data. The energy dependence of full-energy-peak efficiency is shown in Fig. 3.12(b). Below around 200 keV, the efficiency is rapidly decreased since the low energy γ rays are absorbed in the beam pipe, chassis of the detector, cooler ring and the insensitive area of germanium crystal itself. The energy dependence is well approximated by a empirical function of aE^b with $a = 74.5$ and $b = -0.689$ shown in Fig. 3.12(b). These tendency are well reproduced by the simulations using GEANT4 code described in section 3.6.

3.5.2 Timing Information

The γ-ray detectors are sensitive not only to the γ rays from reaction products but also to charged particles, neutrons, γ rays from detectors, and the natural background. The timing of the germanium detector is used for checking and reducing the amount of such background γ rays.

Figure 3.13(a) shows a correlation between the timing and the γ-ray energy measured with GRAPE in coincidence with ^{13}B. The timing is obtained as the time difference between the arrival timings of γ-ray to the germanium detector and of the incident particle to the secondary target. The latter timing is almost same as the timing of γ-ray emission. The arrival timing of the secondary beam at the secondary target is estimated from the time information of F2PL and F3PL. The horizontal axis is shifted with arbitrary offset for convenience. The true coincident events are located at around 300 ns. Figure 3.13(b) is a projection to the

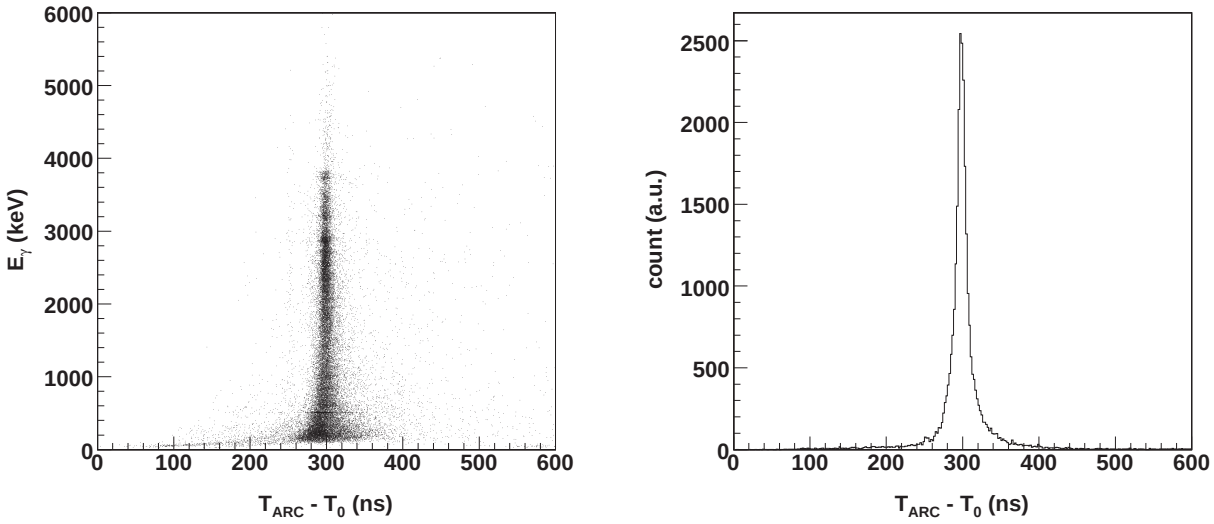

(a) energy vs timing (b) timing distribution

Figure 3.13: (a) Typical scatter plot of γ-ray energy and timing difference after walk correction. The timing difference is between γ-ray detection timing and time when the nuclear reaction occurred. The prompt peak is adjusted to be zero. (b) The timing distribution of γ-ray detectors. The prompt timing window is set to the hatched region and the pre- and post-prompt timing window is set to the region indicated by arrows.

horizontal axis of Fig. 3.13(a). As seen in Fig. 3.13, there are small amount of accidentally coincident events pre- and post-prompt region. To estimate the accidentally coincident events, the timing spectrum for ^{12}Be is obtained. The pre- and post-prompt events are select by setting the 100 ns timing window before 350 ns and after 450 ns region on the projected timing spectrum. The obtained energy spectrum for the background events are modified in the same manner for the Doppler correction of the energy spectrum for ^{13}B.

3.5.3 Extraction of γ-ray Interaction Position

The depth is extracted from the correlation between the zero-cross timing of the $(\mathrm{CR})^2$-$(\mathrm{RC})^4$ shaped pulse of the net-charge (T_{sum}) and segment (T_{seg}) (see Sec 2.4.2). The experimentally obtained correlation in the center region is shown in Fig. 3.14(b). The T_{sum} is measured taking the timing when the incident particle arrives at secondary target as a starting point so as to reduce the timing deviation due to the momentum deviation of the incident particle. The offsets of T_{sum} and T_{seg} are tuned so as to minimize the distance of each experimental datum to the nearest simulated point. The distance D is the norm of the vector between

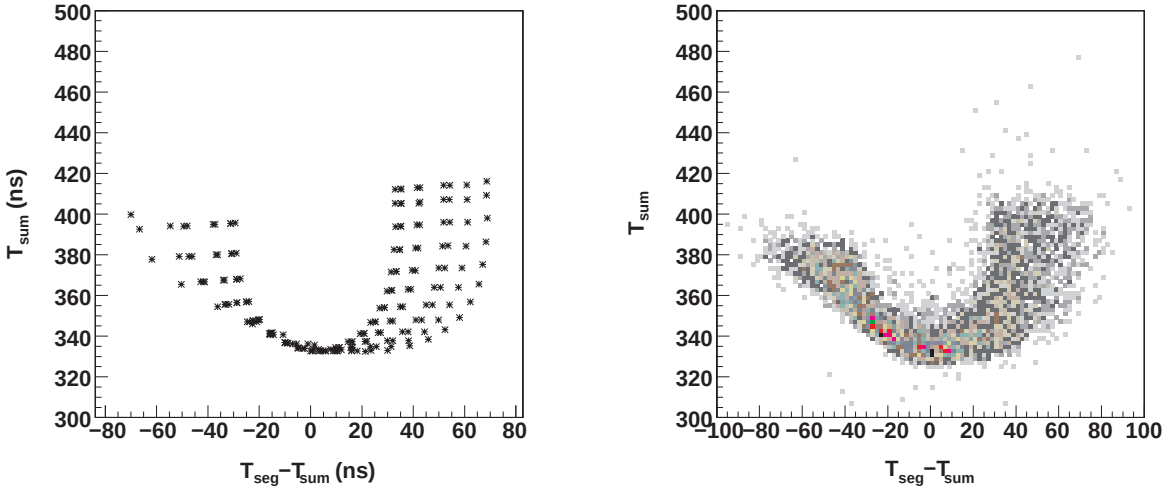

(a) Simulation (b) experiment

Figure 3.14: Correlation between T_{sum} and T_{seg}.

the experimental and simulated data calculated as below,

$$D = \sqrt{(T_{sum}^{exp} - T_{sum}^{sim})^2 + \{(T_{seg}^{exp} - T_{sum}^{exp}) - (T_{seg}^{sim} - T_{sum}^{sim})\}^2}. \tag{3.38}$$

The experimental data is well reproduced by the simulation (Fig. 3.14(a)). The depth is determined on an event-by-event basis by comparing the experimental datum with the simulated one. The simulated depth which gives the minimum D is referred as the depth of the interaction position. Figure 3.15 shows the distance distribution. When many segments are fired, the segment where maximum energy is deposited is assumed to be hit first since we cannot know which segment is hit first in the present setup.

3.5.4 Doppler Correction

The γ rays are emitted from reaction products moving at a velocity $v/c \sim 0.29$. Hence the measured γ-ray energy is shifted because of the Doppler effect. The Doppler shift is corrected for by using the angular information of the γ-ray emission and the velocity of the reaction product. The γ-ray energy in the laboratory frame E_γ^{lab} and the one in the rest frame $E_\gamma^{\rm cm}$ is connected by the velocity of the reaction product β and the gamma-ray emission angle with respect to the momentum vector of reaction product in the laboratory frame θ_γ^{lab} as follows,

$$E_\gamma^{\rm cm} = \gamma \left(1 - \beta \cos\theta_\gamma^{lab}\right) E_\gamma^{lab}, \tag{3.39}$$

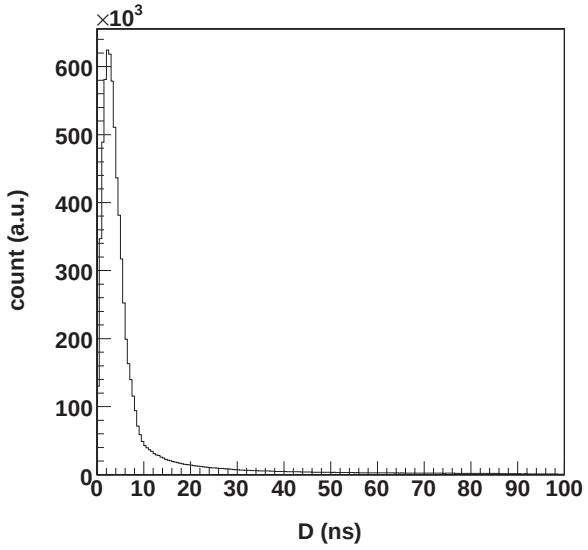

Figure 3.15: Distance between the simulation and experimental data in the correlation between T_{sum} and T_{seg}.

where γ is the Lorentz factor $1/\sqrt{(1-\beta^2)}$. The angle θ_γ^{lab} is determined by the geometrical information for each germanium detector and the pulse shape analysis described in Sec. 3.5.3.

A typical example of the Doppler-shift correction is shown in Fig. 3.16. Figure 3.16(a) shows the energy spectrum before the Doppler-shift correction. The broad peak at around 1600 keV corresponds to the γ decay of the 2.1-MeV excited state in ^{12}Be. The energy spectrum has been obtained by selecting the prompt region. The energy spectrum after Doppler-shift correction for the energy spectrum shown in Fig. 3.16(a) with the pulse-shape analysis is shown in Fig. 3.16(b). The correction has been performed on an event-by-event basis. Two peaks corresponding to the decay 2^+ and 1^- of ^{12}Be are seen in the Doppler-shift corrected spectrum. The energy resolution of 1.3% (FWHM) has been achieved after the Doppler-shift correction with the pulse-shape analysis.

Due to the finite resolutions of the emission angle and of the reaction product velocity, the γ ray energy peaks are broader compared to the intrinsic energy resolution of the detectors, which is called Doppler broadening. The Doppler broadening of $E_\gamma^{\rm cm}$ is approximated based on Eq. (3.39).

$$\left(\frac{\Delta E_\gamma^{\rm cm}}{E_\gamma^{\rm cm}}\right) = \left(\frac{\Delta E_\gamma^{lab}}{E_\gamma^{lab}}\right)^2 + \left(\frac{\beta\gamma^2(\beta-\cos\theta_\gamma^{lab})}{1-\beta\cos\theta_\gamma^{lab}}\right)^2 \left(\frac{\Delta\beta}{\beta}\right)^2 + \left(\frac{\beta\sin\theta_\gamma^{lab}}{1-\beta\cos\theta_\gamma^{lab}}\right)^2 \left(\Delta\theta_\gamma^{lab}\right)^2 \tag{3.40}$$

Three components contribute the energy resolution: the intrinsic resolution of the germanium detector $\Delta E_\gamma^{lab}/E_\gamma^{lab}$; the ambiguity of the velocity of the reaction product $\Delta\beta/\beta$; the

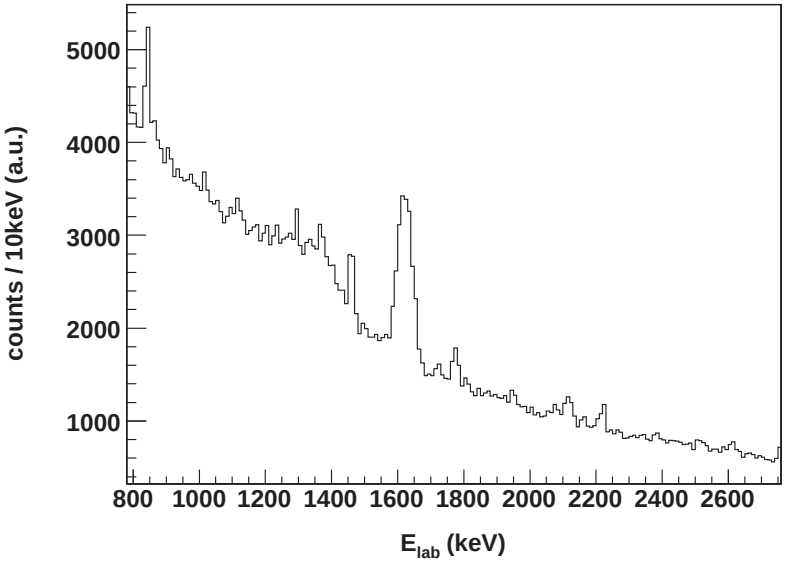

(a) Energy spectrum for ^{12}Be before Doppler correction

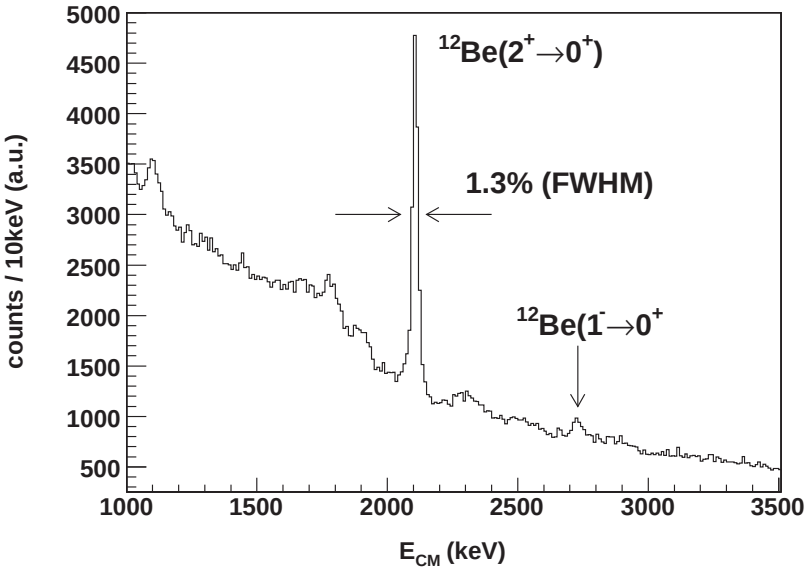

(b) Energy spectrum for ^{12}Be after Doppler correction

Figure 3.16: Typical example of the Doppler-shift correction with the GRAPE. (a) Energy spectrum for ^{12}Be before Doppler-correction. Around 1600 keV the broad peak corresponding to the γ decay of 2.1-MeV excited state in ^{12}Be is seen. (b) The high resolution energy spectrum for ^{12}Be nuclei after Doppler correction is obtained with the pulse-shape analysis. The energy resolution of 1.3% (FWHM) is achieved for the γ rays emitted from the fast moving ($\beta \sim 0.3$) nuclei. Not only the transition at 2.1 MeV from the first excited state but also the one at 2.7 MeV from the well known intruder state is clearly seen.

accuracy of the γ-ray emission angle $\Delta\theta_\gamma^{lab}$. For an estimation of the energy resolution, the realistic condition deduced from the experimental data is taken, *i.e.*, $\Delta E_\gamma^{lab}/E_\gamma^{lab} = 0.46\%$, $\Delta\beta/\beta = 0.52\%$. The angular resolution is assumed to be $\Delta\theta_\gamma^{lab} = 91$mrad which corresponds to the 10 mm ambiguity of the γ-ray interaction position while the resolution of the γ-ray position is assumed to be 3 mm in the simulation taking the position ambiguity of the incident particle into account. The estimated overall energy resolution is 1.5%, which is consistent with the experimental value 1.3%.

3.6 γ-ray Yield

This section describes a procedure for deducing the populations of excited states. The populations are calculated from intensities of transition γ rays deduced from a decomposition of the γ-ray energy spectrum with response functions of GRAPE. The decomposition is performed by fitting the response functions to the experimental energy spectrum with parameters of normalization factors. The response functions are obtained by means of Monte Calro simulation with a toolkit for the simulation, GEANT4 taking into account the actual configurations of germanium crystals and of the experimental equipments such as the γ-ray detector cases, the support materials of GRAPE, vacuum chambers, the secondary target cell, and the heat shield.

There is incomplete collection of the induced charge in germanium detector used in GRAPE so that a tail arises at the low energy side of the total energy peak. The shape of the tailing is approximated to be an exponential function of the γ-ray energy, and its probability is represented as follows,

$$P(E_\gamma^{sim}) \propto \exp\left(\frac{E_\gamma^{sim} - E_\gamma^0}{\alpha E_\gamma^0}\right), \tag{3.41}$$

where E_γ^0 and E_γ^{sim} indicate the original energy deposition, and the energy include the effect of the incomplete collection, respectively, and α is a scaling factor. The fraction of the modified events and scaling factor α are deduced by fitting the simulated response function to the experimental data taken with a standard source ^{137}Cs.

The simulated response function is folded with a Gaussian distribution with intrinsic resolution dependent on the γ-ray energy. The intrinsic resolution ΔE_γ^{lab} is approximated to be a function of the γ-ray energy as follows,

$$\Delta E_\gamma^{sim} = \sqrt{\sigma_0^2 + \sigma_{\rm E} E_\gamma^{sim}}, \tag{3.42}$$

where σ_0 is energy independent resolution due to the circuit noise and $\sigma_{\rm E}$ is energy dependent factor.

Figure 3.17(a) shows the comparison between the experimentally obtained and simulated response functions for 661-keV γ rays from a ^{137}Cs standard source. The experimentally

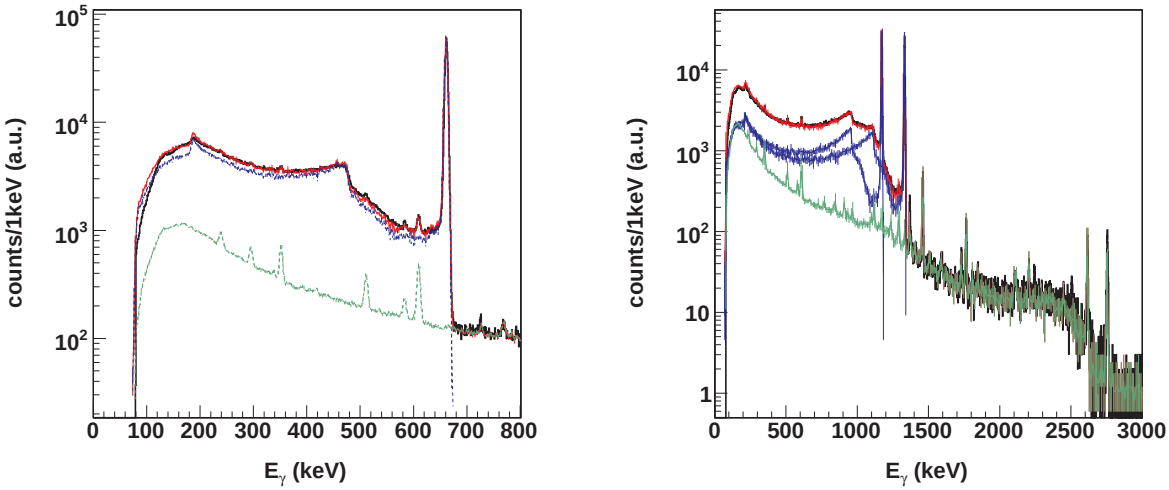

(a) ^{137}Cs (b) ^{60}Co

Figure 3.17: The experimental and simulated response functions of the GRAPE for the γ rays from ^{137}Cs standard source. The experimental response function is well reproduced by the simulated one. The (black) thick solid line shows the experimentally obtained response function including the background γ rays. The (blue) dotted line shows the simulated response function for 661-keV γ rays and the (green) dotted line shows the response function for the background γ rays. The (red) thin solid line shows the response function fitted to the experimental one. (b) The comparison for the standard source ^{60}Co. The (blue) dotted curves show the simulated response functions for 1173- and 1333-keV γ rays. The legends for the other curves are same as those of (a).

obtained response function indicated by the (black) thick solid line is well reproduced by the simulated one indicated by the (red) thin solid line for the whole energy region including the region between the full-energy peak and the Compton edge. Each response function includes the experimental response function for the natural background γ rays indicated by the (green) dotted line (the same spectrum shown in Fig. 3.11(b)). The intensity of the natural background γ rays is fixed to reproduce the response function above 680 keV. The (blue) dotted line shows the response function simulated with GEANT4 taking the energy-dependent energy resolution, threshold of the electric circuit, and effect of the insufficient charge collection discussed above into account. Figure 3.17(b) shows the comparison for the case of the standard source ^{60}Co. There are two simulated response functions for 1173- and 1333-keV γ rays indicated by (blue) dotted curves. The experimental energy spectrum is also well reproduced by the combination of the simulated response functions and that for

the natural background γ rays.

In the case of the simulation of the in-flight γ-ray measurement, the momentum and spacial distributions of the incident beam, the energy loss of the incident and the outgoing particles in the secondary target, the position resolutions of PPACs, GRAPE, and hodoscope, and the resolution of the velocity are taken into account.

In order to extract yields of the transition γ-rays, the γ-ray energy spectrum is decomposed into the simulated response functions and reasonable background with intensity parameters. The intensity parameters are deduced by means of maximum likelihood estimation. The Poisson distribution is adopted to the likelihood functions in order to be applicable to γ-ray energy spectra with low statistics, *i.e.*,

$$L(\boldsymbol{y};\boldsymbol{\nu}) = \prod_{i=1}^{N} \frac{y_i^{\nu_i} \exp(-y_i)}{\nu_i!}, \tag{3.43}$$

where L represents likelihood function, $\boldsymbol{y} = (y_1, y_2, \ldots, y_N)$ experimental yields, and $\boldsymbol{\nu} = (\nu_1, \nu_2, \ldots, \nu_N)$ simulated yields. The ν_i should be a sum of simulated response functions and reasonable backgrounds. When we involve the an intensity parameter α_j for the j-th simulated response function $f_{E_j}(x)$, the ν_i is written as

$$\nu_i = \sum_{j=1}^{n} \alpha f_{E_j}(x_i) + \beta_i, \tag{3.44}$$

where x_i is the mean energy of the i-th bin and β_i is the background contribution at x_i. As the backgrounds taken into account for the decomposition, contributions from contaminant γ-rays in accidental coincidences, such as natural background γ rays, and γ rays originated from the decay of isomeric state of ^{12}Be, and an exponential background represented as $\beta_1 \exp(-\beta_2 x_i)$. In the estimation the likelihood ratio $\lambda = L(\boldsymbol{y};\boldsymbol{\nu})/L(\boldsymbol{y};\boldsymbol{y})$ is maximized. This is equivalent to minimizing the quantity

$$\chi^2 = -2\ln\lambda = -2\ln L(\boldsymbol{y};\boldsymbol{\nu}) + 2\ln L(\boldsymbol{y};\boldsymbol{y}), \tag{3.45}$$

which is asymptotically obeys a χ-square distribution.

As the simplest case, the decompositions of the γ-ray energy spectra for standard sources, ^{137}Cs and ^{60}Co, are demonstrated in Fig. 3.17. Figure 3.17(a) and (b) shows the spectra taken with ^{137}Cs and ^{60}Co, respectively. In each figure, the thick solid line shows a sum of the response functions and backgrounds, the thin solid line response functions, and the dashed line a background γ-ray spectrum shown in Fig. 3.17(c). The background γ-ray spectrum is obtained after the experiment without any standard sources, where many significant γ lines are identified; from the decay of ^{40}K and the Pb group nuclei as natural background; from the decay of the Fe group nuclei produced during the experiment via the reaction on the nuclei in the vacuum chamber and in the secondary target cell; from the decay of ^{24}Na

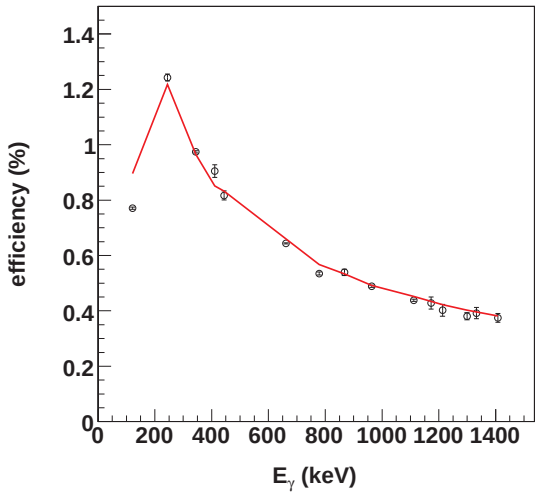

Figure 3.18: The comparison between the experimental and simulated efficiencies of the GRAPE. The open circles show the efficiencies obtained from the experimental data with the statistical errors. The details for the experimental data is described in section 3.5.1. The (red) solid curve shows the simulated efficiency curves. They are consistent within 10% errors.

in NaI(Tl) detector (not used in the present study) irradiated during the experiment. The exponential background, which comes usually from unspecified origin, is not needed for the decompositions. Comparing the γ-ray emission numbers of the sources in the literature and in the simulation, there is a 10% deviation between them as shown in Fig. 3.18. The extrapolation of the efficiency curve to the higher energy is valid based on the fact that the trend of the efficiency is well reproduced by the simulation for the whole energy region up to 1.4 MeV and the shape of the simulated response functions reproduce the experimental one well. Hence, the response function obtained from the simulations reasonably reproduce the experimental data of GRAPE and it enable estimation of the γ-ray yields by the decomposition of the experimental spectra into simulated response functions within 10% systematic uncertainty.

3.7 Angular Distribution and DWBA Analysis

The angular distribution of outgoing particles is essential for deducing angular momentum. The distribution is obtained by applying the decomposition analysis again. In this procedure, the spectra, which will be decomposed, are obtained under a restriction on the scattering

angle of the outgoing particles. After the decomposition of the spectra, deduced strengths of the response functions should indicate products of the differential cross section and the solid angle for the corresponding excited state. This method has the merit that the statistical error can be small even if the statistics under the total energy peak are small since the the total number of events in the spectrum is still large. The decomposition for each angle is performed through the same procedure as described in Sec. 3.6. The intensity of the γ ray from the j-th excited state, which is proportional to the population of the j-th excited state, at the scattering angle θ is obtained as below,

$$\nu_i(\theta) = \sum_{j=1}^{n} \alpha_j(\theta) f_{E_j}(x_i) + \beta_i(\theta), \tag{3.46}$$

where the $\alpha_j(\theta)$ is the the notation is same as Eq. (3.44). The f_{E_j} is the same response function for the de-excitation γ ray of the j-th excited state used in the decomposition to extract the γ ray yields.

In order to determine the transferred angular momentum in the reaction, a distorted wave Born approximation is applied to the analysis of the angular distribution. For this calculation, we used the phenomenological optical potentials deduced from the elastic scattering on the stable nuclei, since the elastic scattering data on ^{12}Be and ^{13}B has not been available. The optical potentials of entrance and exit channels are referred to Ref. [60] and Ref. [61], respectively, and their shape is assumed to be a Woods-Saxon shape:

$$f(x) = \frac{V}{1 + \exp\left[\frac{x-R}{a}\right]}, \tag{3.47}$$

where V, R, a is the depth, radius and diffuseness parameter. The R is calculated as $R = r \cdot A^{1/3}$ by using the reduced radius r. These potentials were obtained via α elastic scattering and ^{3}He elastic scattering on ^{12}C in the intermediate-energy range. Table 3.4 lists the optical potentials used in the DWBA calculations. The calculations are performed by using the computational code DWUCK5. The form factor was calculated from the single-particle wave function in a Woods-Saxon potential in which the potential depth was tuned to reproduce the binding energy of the transferred nucleon to the excited state. In Fig. 3.19, the calculated angular distributions are shown. In each figure, the dashed curve indicates the original angular distribution and the solid curve indicates the one calculated from the original one with consideration of the angular resolution for the scattering angle. Figure (a), (b) and (c) is DWBA predictions for the single-particle states, of which spectroscopic factors are set to unity, at 4.83-MeV excitation energy with the transferred angular momenta of $\Delta L = 0, 1, 2$, that is, by transferring a proton onto the $s_{1/2}$, $p_{1/2}$ and $d_{5/2}$ orbitals on ^{12}Be nucleus, respectively.

	V (MeV)	r_V (fm)	a_v (fm)	W (MeV)	r_W (fm)	a_W (fm)	
entrance	77.25	1.2765	0.801	13.97	1.8846	0.426	^{12}C + α
exit	69.36	1.2526	0.7598	17.17	1.7139	0.6738	^{12}C + ^{3}He

Table 3.4: Global optical model parameters used in DWBA calculation. The parameters are calculated from the formula including the energy dependence deduced in Ref. [60, 61].

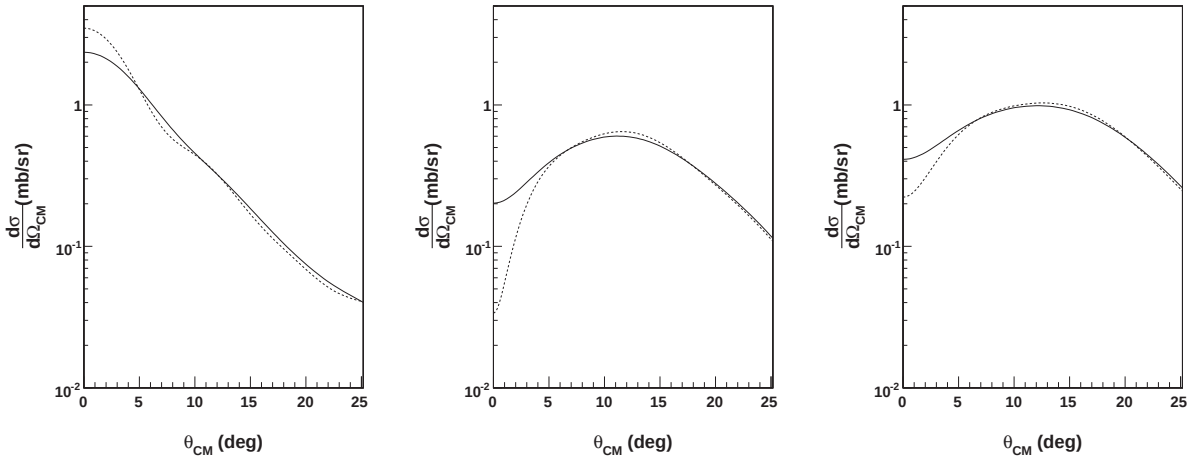

(a) $\Delta L = 0$ (b) $\Delta L = 1$ (c) $\Delta L = 2$

Figure 3.19: Three DWBA predictions with $\Delta L = 0, 1, 2$ in the center-of-mass frame. The solid lines show the angular distributions used for the analysis, which are obtained by folding the predicted distributions indicated dashed lines with angular resolution.

3.8 Single folding potential

In order to deduce the spectroscopic strength and to estimate its potential dependence, another optical potential was obtained in the framework of the folding model [62]. Since the inelastic scattering data of α particle on ^{12}Be is also obtained in the present experiment, the optical potential is obtained by optimize the parameters so as to reproduce the differential cross section of the excitation to the first 2^+ state in ^{12}Be. The real part of the folding optical potential is obtained by folding the nucleon-nucleon interaction by the ground state density distribution in the projectile and target nucleus.

A simple approach for this model, known as single folding model, is to perform the inte-

gration for one nucleus. In the present case, the integration for the α particle is assumed to be already done. Furthermore, the density dependence of the effective α-nucleon interaction in the target nuclei is taken into account according to the recipe proposed in Ref. [63]. Then the effective α-nucleon interaction is obtained as follows,

$$v(s, \rho(r')) = -(v + iw) \exp(-s^2/t^2)(1 - \alpha \{\rho(r')\}^{2/3}), \tag{3.48}$$

where $s = |\boldsymbol{r} - \boldsymbol{r'}|$ is the distance between the center of mass of the α particle and a target nucleon and $\rho(r')$ is the ground state density of the target nucleus, such as ^{12}Be. The parameters of v, t, α have been determined [63] by analyzing the experimental deferential cross section of alpha elastic scattering on ^{58}Ni at 240 MeV incident energy, and they are 36.15 MeV, 1.88 fm, and 1.9 fm^2, respectively. The parameter w, which is the imaginary part of the effective interaction, is determined by analysing the inelastic scattering on ^{12}Be measured in the present experiment, as described below.

The single folding optical potential is obtained by folding the effective α-nucleon interaction by the ground state density of the ^{12}Be nucleus as follows,

$$U(r) = \int v(s, \rho(r')) \cdot \rho(r') \mathrm{d}\boldsymbol{r'}, \tag{3.49}$$

where $\rho(r')$ is the ground state density same as that in Eq. (3.48).

The ground state density of the ^{12}Be nucleus is obtained from a relativistic mean-field calculation by using the computational code TIMORA. The calculated density is shown in Fig. 3.20(a). Figure 3.20(b) shows the real part of the obtained optical potential together with the approximate Woods-Saxon shape optical potential (Eq. (3.47)). The (black) solid line shows the single folding potential calculated using Eq. (3.49) and the (red) dashed line shows the approximate Woods-Saxon potential fitted to the single folding one. The depth (V), reduced radius (r_v), and diffuseness (a_v) of Woods-Saxon shape are -72.57 MeV, 1.088 fm, and 0.9351 fm, respectively, obtained by fitting to the calculated single folding potential. Although there are small discrepancies at the inner and surface region between two potentials, since they are almost the same as the general trend the Woods-Saxon potential is a good approximation to the single folding potential. The resultant Woods-Saxon potential is utilized for the DWBA calculation.

The imaginary part of the single folding potential is deduced so as to reproduce the differential cross section of the 2.1-MeV state in the ^{12}Be nucleus excited by inelastic scattering. The shape of the imaginary part is assumed to be the same as that of the real part based on Eq. (3.48), *i.e.*, the reduced radius r and diffuseness a is common for the real and imaginary part. A computational code, DWUCK4, is employed for the DWBA calculation. The calculated differential cross section is fitted to the experimental data with two parameters, the depth W of the imaginary part and the normalization of the intensity, so as to minimize the χ^2 value.

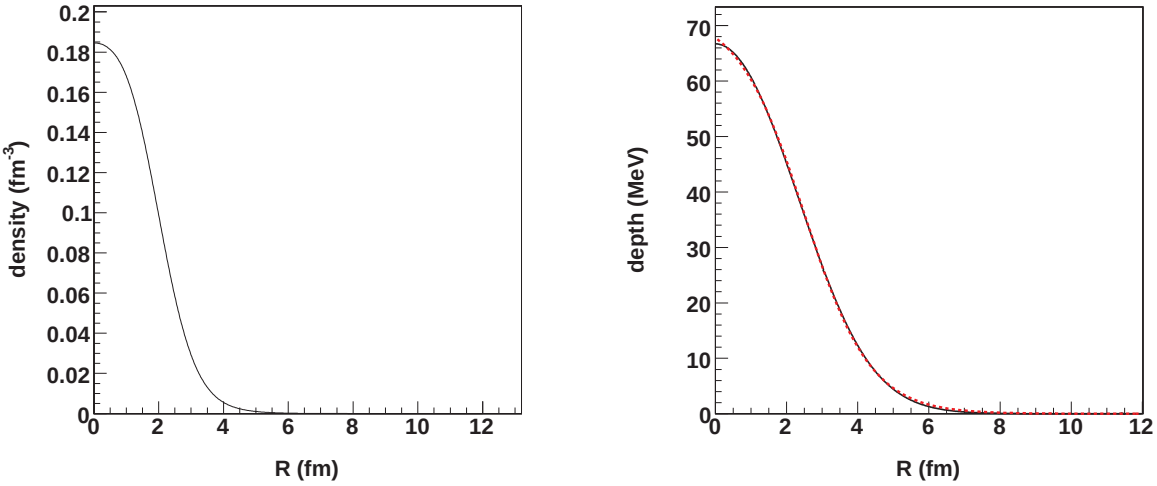

(a) Calculated density distribution of ^{12}Be (b) Single-folding and Woods-Saxon potential

Figure 3.20: (a) Calculated density distribution of ^{12}Be by using TIMORA computational code without further optimizing. (b) The real parts of single folding optical potential and approximate Woods-Saxon potential. The (black) solid line shows the single folding potential and the (red) dotted line shows the approximate Woods-Saxon potential. See the text for the detail.

Table 3.5 lists the parameters of the approximate Woods-Saxon optical potential deduced from the single-folding model. The first raw lists the parameters for the real and imaginary part of the optical potential for the entrance channel of ^{12}Be+^{4}He. The parameters of r and a for the exit channel are taken from the entrance channel by assuming the ground state density is same as that of ^{12}Be with $R(^{13}\mathrm{B})/R(^{12}\mathrm{Be}) = (13/12)^{1/3}$. The depths of the real and imaginary part for the exit channel are varied to estimate the statistical error of the spectroscopic factor. In the table 3.5, the best-fit parameters are listed. See Sec. 4.3.2 for the detail.

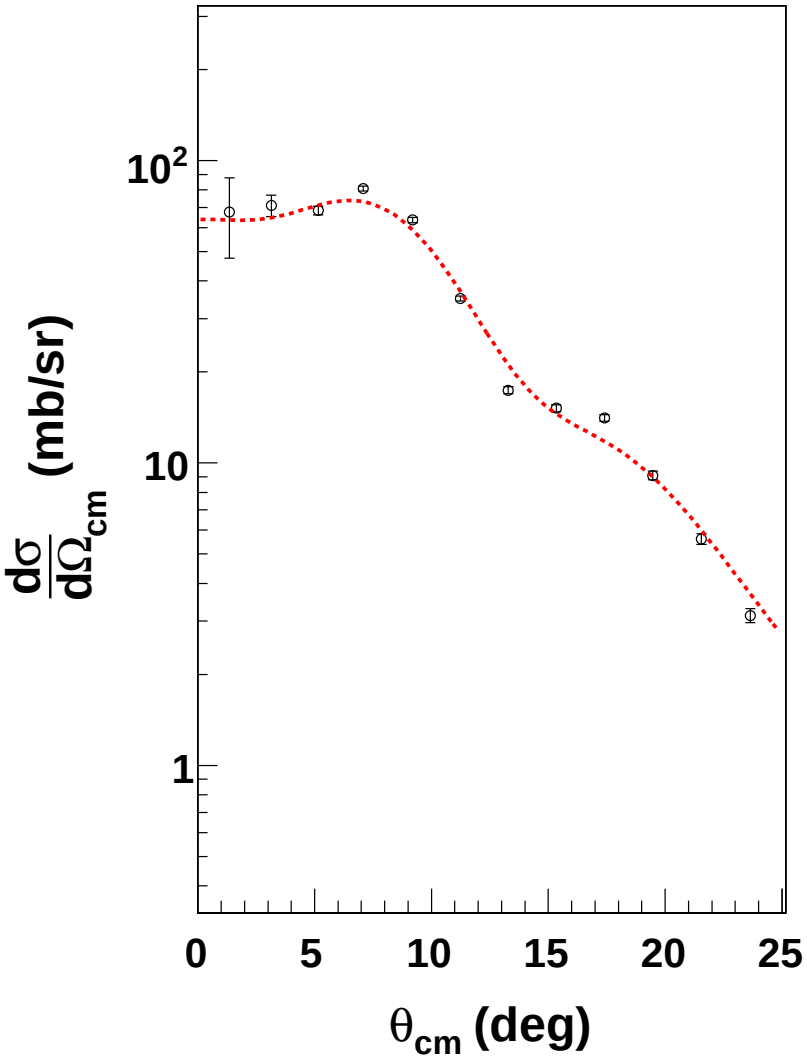

Figure 3.21: The differential cross section of the inelastic scattering on ^{12}Be exciting 2_1^+ state. The open circle shows the experimental data obtained by decomposition of the γ-ray energy spectrum measured in coincidence with ^{12}Be. The (red) dotted line shows the DWBA prediction for $\Delta L = 0$ with the single folding potential. The imaginary part of the potential is optimized so as to represent the experimental data. The details are in the text.

	V (MeV)	r_V (fm)	a_V (fm)	W (MeV)	r_W (fm)	a_W (fm)
^{12}Be+^{4}He	-72.57	1.09	0.94	-42.69	1.09	0.94
^{13}B+^{3}H	-113.6	1.09	0.94	-32.6	1.09	0.94

Table 3.5: Optical potential parameters obtained in the frame work of the single folding model. First and second rows show the potential parameters for the entrance and exit channels, respectively. The reduced radius and diffuseness are common for the two channels. The depth of the imaginary part for the entrance channel is adjusted so as to reproduce the inelastic scattering data. The depths for the exit channel is the best-fit value. See the text for the detail.

Chapter 4

Experimental Results

This chapter descries the experimental results concerning the excited states of ^{13}B. In section 4.1, the energy spectrum of ^{13}B is obtained by applying the window of the atomic number and the mass number on the reaction products. We have found several peaks corresponding to the de-excitation gamma rays from ^{13}B. In order to obtain the transition strength of each excited state to the ground, the energy spectrum is decomposed with response functions simulated with GEANT4 and experimentally obtained backgrounds (Sec. 4.2). The angular distributions of the differential cross sections are extracted as the yield of γ rays obtained in every 0.5 degree angular regions to which ^{13}B is scattered (Sec. 4.3). The distributions are analyzed with DWBA, and the spin information and the spectroscopic strength are deduced in Sec. 4.3.1 and Sec. 4.3.2, respectively.

4.1 Energy Spectrum after Doppler Correction

The γ-ray energy spectrum of ^{13}B via the proton stripping reaction is obtained. The windows of the atomic number Z and that of the mass number A are set as $4.5 \leq Z \leq 5.5$ and $12.5 \leq A \leq 13.5$, respectively. The Doppler shift is corrected on an event-by-event basis by using the γ-ray emission angle to the scattered ^{13}B deduced from the positions measured with PPACs, hodoscope and GRAPE, and the velocity of the scattered ^{13}B deduced from the timings measured with F2PL, F3PL and hodoscope. In order to select the two-body reaction, the difference between the volocities of the incident and outgoing particles are limitted by setting the window on the velocity difference spectrum. We have found three peaks at around 3.7, 4.1 and 4.8 MeV, corresponding to the excitation energy (3.68, 3.73), 4.13, and 4.83 MeV. A doublet of 3.68- and 3.73-MeV γ rays has not been resolved by the present energy resolution of GRAPE. There is very few events above 5 MeV, which represents that no γ line having more than 5 MeV energy exists, since the neutron separation energy of ^{13}B is 4.88 MeV. At the low energy region around 1–1.5 MeV, there seems to be relatively wide peak, which is found also in energy spectra for the other boron isotopes such as ^{10,11,12}B

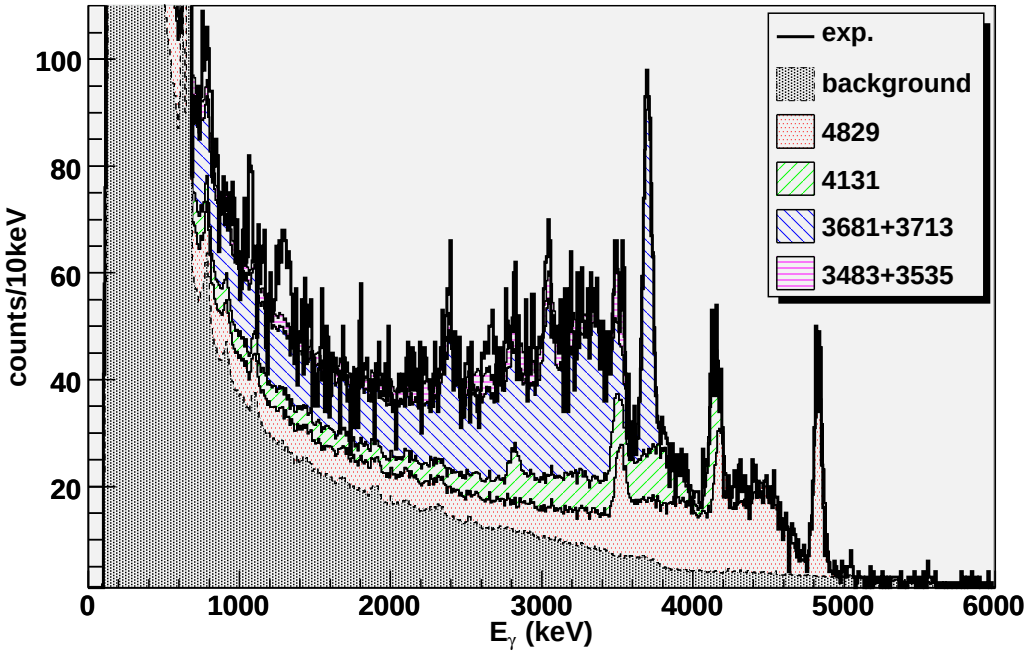

Figure 4.1: Doppler corrected γ-ray spectrum in coincidence with ^{13}B particles. The spectrum is decomposed with the sum of response functions of the GRAPE for the de-excitation and background γ rays. The resulting response functions are shown with hatched areas. The response functions for two doublets around 3.5 and 3.7 MeV are summed. The response function for the background includes the natural background and the decay of the ^{12}Be isomer (see the text).

shown in Fig. 4.2. The wide peak, therefore, seems to be background γ rays in coincidence with the beam particles although the origin has not been unspecified.

4.2 Cross Sections for Excited States in ^{13}B

The cross sections for the excited states in ^{13}B are deduced by the decomposition analysis described in section 3.6. The γ-ray spectrum shown in Fig. 4.1 is decomposed into the response functions and backgrounds. The histogram shows the experimental spectrum. The simulated response functions for the de-excitation γ rays and the response function for the background γ rays are shown by the color and shade in the legend. The decomposition is performed in the energy region above 700 keV since there is no significant peak in the region below 700 keV. From the decomposition of the experimental spectrum, the number of the emitted γ rays are obtained. The number of the γ rays corresponds to the the number of

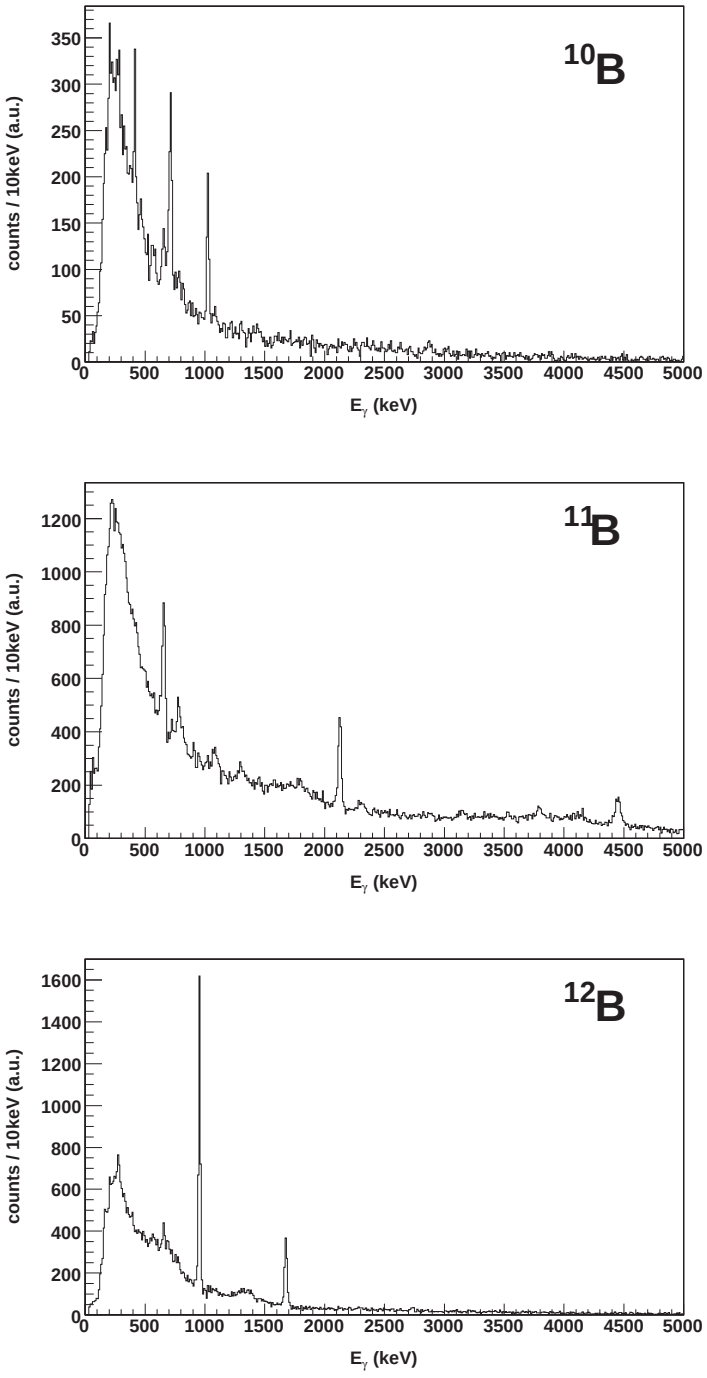

Figure 4.2: Doppler corrected γ-ray spectrum in coincidence with ^{10,11,12}B particles. The known γ lines are observed.

Ex (keV)	$\sigma(< 6^\circ)$ (mb)
3483	0.16 ± 0.04
3535	0.17 ± 0.04
3681	0.65 ± 0.06
3713	0.60 ± 0.06
4131	0.43 ± 0.04
4829	0.88 ± 0.03

Table 4.1: List of the cross sections for the excited states in ^{13}B via the proton transfer reaction on ^{12}Be. The cross sections are obtained as the integration up to ??? degrees of scattered ^{13}B in laboratory frame. The errors are statistical only. The energies of the excited states are values from (see, *e.g.*, Ref. [64] [NNDC]).

the ^{13}B excited to the corresponding energy since the γ-ray transitions between the excited states are small within the statistical errors based on the fact that the no γ-line between the excited states is observed. The cross sections are calculated in combination with the number of the γ rays, beam particles and target thickness.

The obtained cross sections are listed in Table 4.1, with the statistical errors evaluated in the decomposition. The cross sections are obtained by the angular integration of ^{13}B up to the scattering angle of 6 degrees in the laboratory system. The systematic error for the absolute magnitude due to the geometrical condition of the GRAPE is estimated to be 10% as described in Sec. 3.6. The two doublets at 3.5 and 3.7 MeV could not be resolved within the present energy resolution. The strengths in the doublet have strong correlation and more systematic errors. In the present study of the proton transfer reaction, the population of 4.83 MeV excited state is strongly populated, which may indicate the 4.83 MeV excited state is of a proton single particle nature.

4.3 Angular Distributions for Excited States in ^{13}B

The angular differential cross sections for each excited state is extracted via the decomposition analysis of the energy spectra for every 0.5-degree angular region up to 6 degrees in laboratory frame, as described in Sec. 3.7. The angular acceptance of the hodoscope is almost 100% for every angular region so that the correction is not necessary. Figure 4.3 shows the deduced differential cross sections of each excited state converted to the ones in the center-of-mass frame. The errors are statistical only. The angular differential cross sections of the 4.83-MeV excited state shown in Fig. 4.3(f) has the forward peak, which indicates the transfer angular momentum is zero. In Sec. 4.3.1, the spin and parity of each excited state is assigned based on the DWBA analysis of the differential cross section. Section 4.3.2 describes the spectroscopic strength and its statistical error deduced from the DWBA analysis

E_{ex}	reduced χ^2 for $\Delta L =$			J^π
(keV)	0	1	2	
3483	1.88	2.31	2.30	
3535	1.31	1.80	1.79	
3681	2.01	5.38	4.91	$(1/2, 3/2, 5/2)^+$
3713	2.54	2.74	2.44	$(1/2, 3/2)^-$
4131	3.99	2.55	2.26	$(1/2, 3/2)^-$
4829	0.68	46.88	43.75	$1/2^+$

Table 4.2: List of the reduced χ^2 obtained by fitting the each DWBA prediction using the single folding model to the experimental data and the deduced spins and parities ($J^\pi s$). The first column lists the excitation energy and the second, third and forth column list the reduced χ^2 for the transferred angular momentum $\Delta L = 0, 1$, and 2, respectively. The last column lists the spin and parity assigned only to the 4.83-MeV excited state and the candidate given to the other states with parenthesis.

using the single folding potential described in section 3.8.

4.3.1 Spin and Parity Assignment

The DWBA calculations are performed with the transferred angular momenta (ΔL) of 0, 1, and 2. The ^{13}B has five protons and eight neutrons while the core of ^{12}Be has for protons. In the present reaction of proton transfer, the low-lying states have a configuration of ^{12}Be $\otimes$ $(\pi psd)^1$ so that the last proton is expected to be transferred to one of the orbits in psd shell with $\Delta L = 0, 1, 2$, *i.e.* to the $p_{1/2}(\Delta L = 1)$, $s_{1/2}(\Delta L = 0)$, and $d_{5/2}(\Delta L = 2)$. The strength of each predictions is normalized be minimize the χ^2 value.

Figure 4.4 shows the differential cross section and the DWBA prediction with the global optical potential for the 4.83-MeV excited state. The experimental data are reproduced by the $\Delta L = 0$ DWBA prediction very well. Since the spin and parity of the core nucleus ^{12}Be is 0^+, the spin and parity of 1/2+ is assigned to the 4.83-MeV excited state for the first time.

The DWBA predictions for the 4.83-MeV excited state using the single folding potential is shown in Figure 4.3(f). The potential parameter set is deduced from the inelastic scattering data of ^{12}Be as described in section 3.8. The experimental data is well reproduced by the DWBA calculation again. The spectroscopic strength is $0.20 \pm 0.02(stat.) \pm 0.1(syst.)$ as described in the next section. The other excited states are analyzed using the single folding potential with the best-fit parameters. The DWBA predictions for all the excited states are shown in Fig. 4.3. The minimized χ^2 values are listed in Table 4.2. The second, third, and forth columns list the χ^2 values for each excited state with the ΔL =0, 1, and 2, respectively.

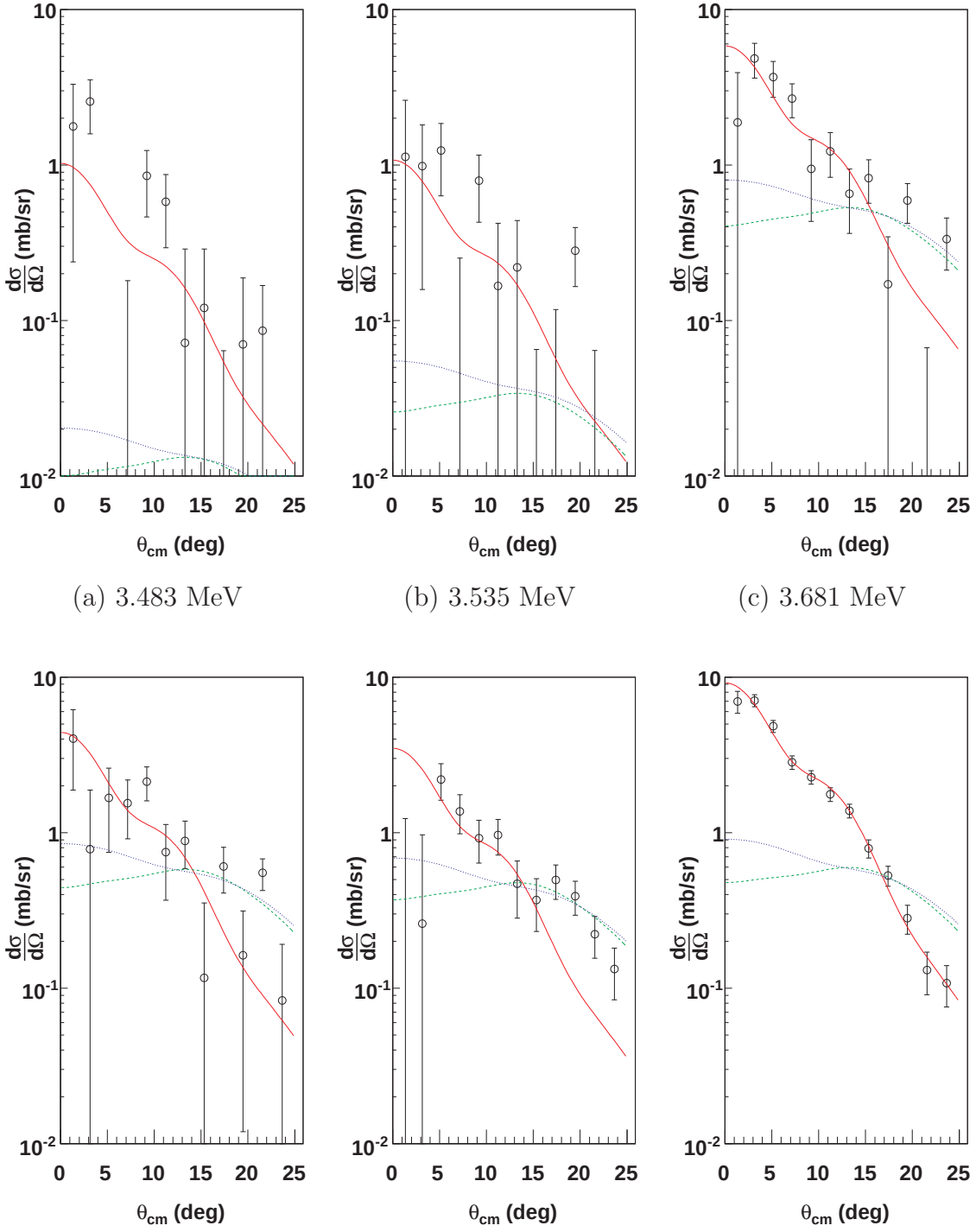

(a) 3.483 MeV (b) 3.535 MeV (c) 3.681 MeV

(d) 3.713 MeV (e) 4.131 MeV (f) 4.829 MeV

Figure 4.3: Differential cross section of each excited state in ^{13}B. The errors are statistical only. The (red) solid, (green) dashed, and (blue) dotted line shows the DWBA prediction using the single folding optical potential with the transferred angular momentum $\Delta L = 0, 1$, and 2, respectively. See the text for the detail.

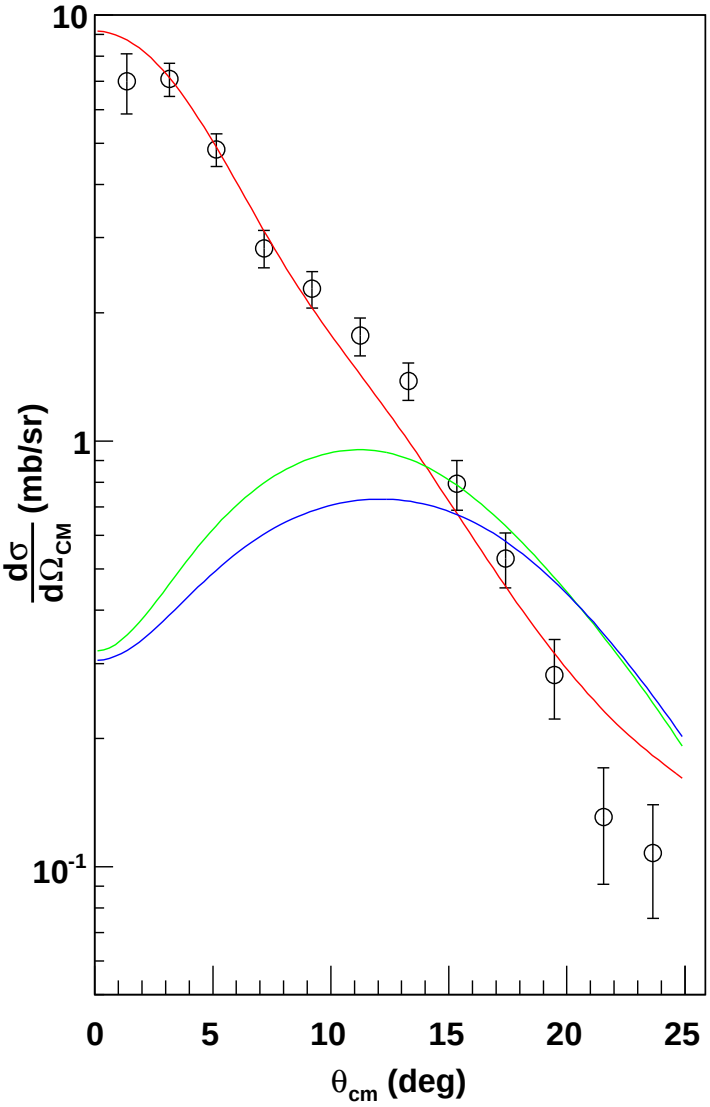

Figure 4.4: The angular distribution of ^{13}B for the 4.83-MeV excitation via the proton transfer reaction ^{4}He(^{12}Be,^{13}B*). The open circle shows the experimentally obtained angular distribution and the (red) solid, (green) dashed, and (blue) dotted curves show the DWBA predictions with $\Delta L = 0, 1, 2$, respectively, with global optical potentials. The DWBA predictions are folded by the angular resolution measured in the present experiment.

Figure 4.3(c) shows the differential cross section and the DWBA prediction for the 3.68-MeV state. The experimental data seem to be reproduced by the $\Delta = 0$ DWBA calculation. However, the finite energy resolution of the GRAPE, the 3.68-MeV exited state is not discriminated well from the 3.71-MeV excited state. The spin and parity of $1/2^+$ is a candidate, but the other spins are not rejected in this experiment. The candidates are obtained as described below.

The DWBA analysis for the other states cannot determine due to the statistical errors. However, the possible assignments of the spins of the other several excited states are obtained, where the parities known from the previous experiment in Ref. [43]. In the reference, the parities were determined from the transferred angular momentum deduced from the angular differential cross sections in the two neutron transfer reaction. The 3.54-, 3.71-, and 4.13-MeV excited states have negative parities and the 3.48- and 3.68-MeV excited states have positive parities. Since the 4.13-MeV excited state has negative parity, the transferred angular momentum $\Delta L = 1$ satisfies parity conservation. Then the candidates for the 4.13-MeV excited state are limited to $1/2^-$ and $3/2^-$. The 3.73-MeV excited state has also the negative parity, then the candidates are $1/2^-$ and $3/2^-$. The 3.68-MeV excited state has positive parity. Then the candidates are $1/2^+$, $3/2^+$ and $5/2^+$ assuming $\Delta L = 0$ or $\Delta L = 2$. The 3.48- and 3.53-MeV excited states may not be of a proton-single-particle nature since the populations of the 3.48- and 3.53-MeV excited states are very small. The spins for these states cannot be, therefore, not suggested by the present study. The possible spin assignments given by the present experiment are listed in the last column of Table 4.2.

4.3.2 Spectroscopic Strength

In the previous section, the experimental angular distribution is compared with the DWBA predictions obtained from the phenomenological optical potentials and the transferred angular momenta are deduced. In this section, the result of the spectroscopic strength for each excited state is described.

The spectroscopic strength has a strong dependence in a choice of optical potentials. For a qualitative evaluation of the spectroscopic strength, one needs to estimate how much the spectroscopic strength depends on the optical potentials. For this purpose, in addition to the phenomenological optical potential, a set of single-folding optical potentials for the entrance channel ^{12}Be+^{4}He and the exit channel ^{13}B+^{3}H are used. The single-folding potential is made based on the density-dependent effective interaction, which is described in Sec. 3.8. The radii of the real and imaginary part are the same values for the entrance channel. The density distribution of ^{13}B is assumed to be same as one of ^{12}Be with $R(^{13}B)/R(^{12}Be) = (13/12)^{1/3}$. All the diffusenesses are same. The depth of the real part for the entrance channel is obtained from the single-folding model. The depth of the imaginary part is determined so as to represent the angular differential cross section data of the inelastic scattering on ^{12}Be,

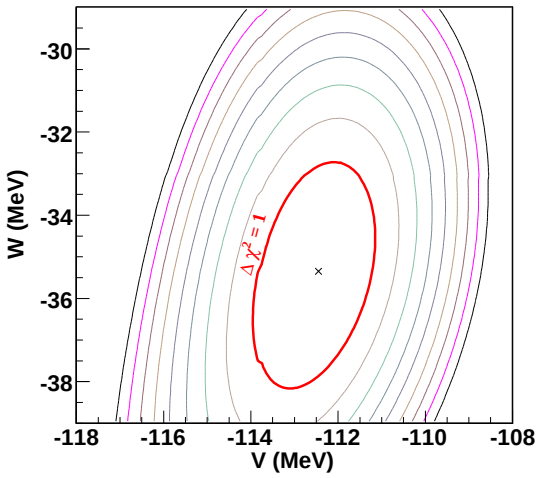

Figure 4.5: The contour plot of χ^2 distribution. Horizontal and vertical axes indicate the depth of the real and imaginary part for the exit channel. The cross indicates the minimum point of the χ^2 value. The closest contour corresponds to the curve where $\Delta\chi^2 = 1$.

populating the 2^+_1 in ^{12}Be. The depths of the real and imaginary part for the exit channel is searched in order to estimate the statistical error for the spectroscopic strength. The search is performed in a energy range from -108.0 to -117.9 MeV and from -29.0 to -38.9 with 0.1 MeV step for the real and imaginary part, respectively. Figure 4.5 shows the χ^2 map as a function of the potential depths for the exit channel. The horizontal and vertical axes indicate the real (V) and imaginary (W) potential depths of the exit channel, respectively. The χ^2 minimum is found at $(V, W) = (-113.6, -32.6)$ in units of MeV. Using these potentials the spectroscopic strength is determined to be 0.20. Its error is estimated to be 0.02 by comparing with the spectroscopic strength obtained using the potential parameter set at $\Delta\chi^2 = 1$ (shown in Fig. 4.5 with a red thick contour). The systematic error is determined to be 50% by comparing with the spectroscopic strength of 0.10 obtained by using the global optical potential. The deduced spectroscopic strength for the 4.83-MeV excited state is $0.20 \pm 0.02(stat.) \pm 0.1(stat.)$.

Chapter 5

Discussion

The γ transitions from the 4.83 MeV excited state and other excited states are observed in the ^{4}He(^{12}Be,^{13}B) reaction, and the 4.83 MeV excited state is found to have the spin and parity of $1/2^{+}$ state. In this chapter, the properties of the excited states, in particular the proton intruder state, and the structure of excited ^{13}B are discussed. In section 5.1, the populations are compared with the previous experimental studies. In section 5.2 and 5.3, the theoretical interpretations of the proton intruder state at 4.83 MeV are discussed. A shell model calculation is demonstrated with the interaction which represent the intruder state in ^{11,12}Be. The calculation in *psd* model space with maximum $3\hbar\omega$ excitation cannot reproduce the experimentally obtained proton intruder state (section 5.2). In Sec. 5.3, the effect of a deformed ^{12}Be core is studied. In this case the proton intruder state is simply expressed to have a configuration of $(\pi sd)^{1}\otimes^{12}$Be. The Nilsson orbital of $[220\frac{1}{2}]$ provides a possible configuration and explains the low excitation energy of the proton intruder state.

5.1 Comparison with the Previous Works

In this section, the previous works are summarized and the properties of the excited state of ^{13}B are characterized based on the reaction selectivity and the present result.

The previous works which are compared with the present study are listed below.

(a). Two neutron transfer reaction on ^{11}B [43] – expected to populate two neutron particle state.

(b). Neutron knockout reaction on ^{14}B [44] – expected to populate one neutron hole state.

(c). β decay of ^{14}Be followed by neutron emission [46] – expected to populate one proton particle one neutron hole state.

(d). Multi-nucleon transfer reaction of ^{16}O [50] – expected to populate one or more proton excited state

E_x	present		(a)	(b)	(c)	(d)	
(MeV)	populations	J^π		populations			J^π
3.48	0.19±0.05		0.06	0.60±0.14			$(3/2^+)$
3.53	0.20±0.05		0.19		1		
3.68	0.74±0.07	$(1/2,3/2,5/2)^+$	0.38	1			$(5/2^+)$
3.71	0.68±0.07	$(1/2,3/2)^-$	0.25				
4.13	0.49±0.04	$(1/2,3/2)^-$	1	0.04±0.04			
4.83	1	$1/2^+$	0.03			1	$(1/2^-)$

Table 5.1: List of the relative populations of the excited states. In the relative populations, intensities are normalized by the most intense population. The errors are statistical only. In the last column, the spins and parities which have been assigned or suggested (with the curry bracket) in the present and previous studies are listed. See the text for the meaning of the label (a), (b), (c) and (d). For the reaction (b) the relative intensity is at $\theta_{\rm lab} = 10^\circ$ and for the reaction (d) at $\theta_{\rm c.m.} = 5.4^\circ$.

The relative populations of the present and these reactions are listed in Table 4.1.

The 4.83 MeV excited state is strongly populated in the present reaction and reaction (d) while is is hardly populated in the other reactions. The present reaction and reaction (d) are expected to populate proton excited state, and the present reaction, in particular, is expected to populate proton single particle states. The reaction (a), (b) and (c) are expected to populate the excited states related to the neutron excitation. The proton single particle nature of the 4.83 MeV excited state is indicated by these comparison. The spin and parity of this state has been assigned to be $1/2^+$ by the DWBA analysis of the angular differential cross sections. The spin and parity of $1/2^-$ was suggested to this state by the reaction (d) in Ref. [50], which is different from the assignment of $1/2^+$ by the present study. In Ref. [50] discussed the spin and parity based on the reaction mechanism and the ground state configuration of ^{16}O. However, the spin and parity was not uniquely determined.

The 4.13 MeV excited state is populated most strongly in reaction (a) and somewhat strongly in the present reaction. Concerning the selectivity of reaction (a), the 4.13 MeV excited state is a two neutron excited state. The transferred angular momentum of two neutrons is reported to be $\Delta L = 2$ in the reaction (a), and the state has negative parity, suggesting the possible spins of $1/2, 3/2, 5/2, 7/2$. To form negative parity, two neutrons should be transferred to the same shell such as $(\nu p)^2$ or $(\nu sd)^2$. Since the two neutrons transferred to p-shell is expected to form the ground state, the 4.13-MeV excited state may have a configuration of $(\nu sd)^2 \otimes ^{11}$B. In the present reaction the proton should be transferred to the p-shell in order to produce negative parity, forming the configuration of $(\pi p)^1 \otimes ^{12}$Be(0+). Concerning the existence of the neutron $2\hbar\omega$ configuration in the ground state of the ^{12}Be

nucleus, the proton transfer to the $p_{3/2}$ orbit allows the configuration of $(\nu sd)^2 \otimes {}^{11}$B forming the spin and parity of $3/2^-$. Based on this discussion, the $3/2^-$ assignment may be more likely although the $1/2^-$ assignment can not be excluded.

The 3.71 MeV excited state is reported to have negative parity via the reaction (a). In the present reaction the transferred angular momentum is non-zero according to the angular distribution. Assuming the possible transferred momentum $\Delta L = 1$, the possible spins are 1/2 and 3/2. The relatively large population shows this excited state is of the single particle nature. The second lowest proton single particle state in ^{13}B is expected to have the spin and parity of $1/2^-$, which is populated by the proton transferred to the $\pi p_{1/2}$ orbital.

5.2 Comparisons with Shell Model Calculation

There are few theoretical predictions for the excited states in ^{13}B. In Ref. [44], the result of a shell model calculation for ^{13}B has been shown, however, the calculation is performed from the viewpoint of the neutron structure. In order to compare with the shell-model predictions, a shell model calculation is performed focusing on the proton shell structure with the calculation code, OXBASH [65]. The model space is *psd*-shell considering the maximum excitation of $3(2)\hbar\omega$ for ^{13}B(^{12}Be). The interaction includes the effect of the tensor force and reproduces intruder states in the neutron-rich nuclei such as ^{11,12}Be [15]. The spectroscopic factor is calculated as the overlap between each excited state of ^{13}B and the ground state of ^{12}Be. The predicted energy, spin, parity and spectroscopic factor of the states in ^{13}B are shown in Fig. 5.1 with the experimental ones.

Focusing on the first six predicted excited states, the excitation energies seem to be predicted in 2 MeV energy difference. However, the shell model cannot predict the spectroscopic strength.

The shell model calculation predicts four $1/2^+$ states below 10 MeV excitation energy. Three lower states are predicted at 3.7, 6.5 and 9.1 MeV with spectroscopic strengths of 0.01, 0.03 and 0.003, respectively. These strengths are too small to explain the experimental result. The fourth $1/2^+$ state with a spectroscopic strength of 0.30 is close to the experimental spectroscopic strength; however its excitation energy is 9.5 MeV. These results of the shell model calculation may indicate that the theoretical approach based on the effect of the tensor force does not explain the experimental result, or the model space consisting of the *psd* shell and the excitation of $3\hbar\omega$ are not large enough.

5.3 Property of $1/2^+$ Intruder State

A simple expression for the observed $1/2^+$ state with proton single particle nature is $(\pi sd)^1 \otimes {}^{12}$Be. Figure 5.2 shows the proton orbitals in the deformed potential of ^{13}B. The deformed poten-

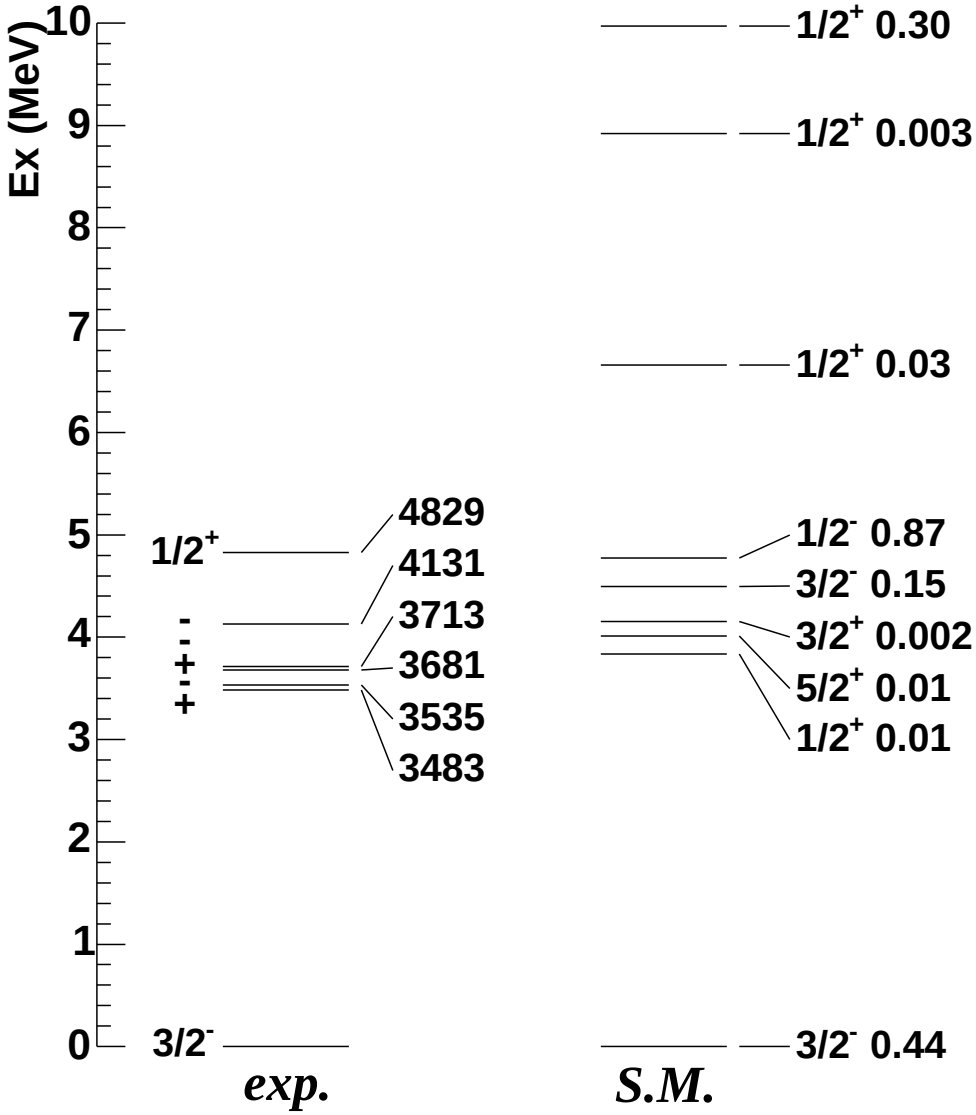

Figure 5.1: The experimental result is shown at the left with each adopted excitation energy, spin, and parity. The shell model predictions are shown at the right with each predicted spin, parity and spectroscopic strength. For the predictions, only four lower $1/2^+$ excited states and the lowest $1/2^-$, $3/2^\pm$, $5/2^+$ excited states are shown. See text for the detail.

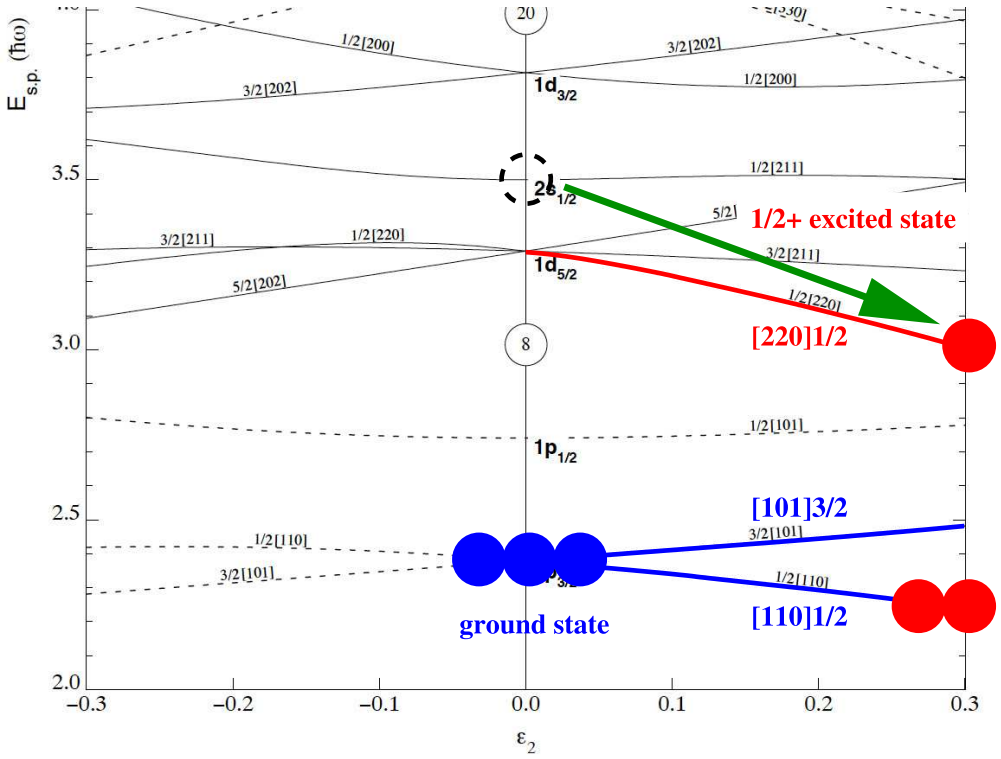

Figure 5.2: Proton orbitals in deformed potential of ^{13}B provided by deformed ^{12}Be core, essentially same as Fig. 1.1. The [220]1/2 orbital indicated by red curve comes down with large deformation parameter and [110]1/2 orbital (the lowest one) comes down too.

tial is provided by the deformed core of ^{12}Be. At the large deformation, the orbitals having the spin and parity of $1/2^+$ in the *sd*-shell are represented by an asymptotic quantum number [220]1/2, [211]1/2, and [202]1/2. In case of a spherical nucleus, the lowest $1/2^+$ state has a configuration of $s_{1/2} \otimes {}^{12}$Be(g.s.), while the lowest one arises with a configuration of $(\pi[220\frac{1}{2}])^1$ to the ^{12}Be(g.s.) core in case of a deformed nucleus.

As described above, at large deformation, the $\pi[220\frac{1}{2}]$ orbital gains energy. The energy gain of the deformed system to the spherical system is estimated. The energy gain of the orbital itself is estimated to be 11.8 MeV from the Nilsson diagram where $\hbar\omega_{deformed} \sim \hbar\omega_{spherical} \sim 41\dot{A}^{-1/3}$ is ∼17.4 MeV at $\delta \sim 0.5$ (recently calculated to be 0.7 [66]). The energy difference estimated from the semi-empirical mass formula consists of the difference of the surface energy and the Coulomb energy, since the volume should be conserved under the change of the shape, and the symmetry and paring energies do not depend on the nuclear shape. The Coulomb energy itself is much smaller than the orbital energy and surface energy and is ignored in this estimation. The surface area of a spheroid is described as below,

$$S = 2\pi[b^2 + ab\sin^{-1}\sqrt{1-(b/a)^2}/\sqrt{1-(b/a)^2}], \tag{5.1}$$

where a represents the length of the symmetry axis, b the one of the axis perpendicular to the symmetry axis, and volume conservation requires the equation of $ab^2 = R_0^3$, where R_0 is the radius when the nucleus is spherical. The spherical surface energy is represented by $-17.2A^{2/3}$ with the surface area $S_0 = 4\pi R_0^2$ in empirical mass formula. Then the energy difference of the surface energy is estimated to be $-17.2A^{2/3}(S/S_0 - 1) \sim -3.4$ MeV for $A = 13$ at $\delta \sim 0.5$. The total energy gain of $1/2^+$ orbital is calculated to be $\sim$8 MeV, which explains the low excitation energy of $1/2^+$ state at 4.83 MeV. The experimentally obtained spectroscopic factor can be compared with the spherical $2s_{1/2}$ component in the deformed $[220\frac{1}{2}]$ orbital, since the proton is transferred by an s-wave ($\Delta L = 0$), which is assumed in the DWBA analysis. The spectroscopic factor of the spherical $2s_{1/2}$ component in the deformed $[220\frac{1}{2}]$ orbital is $S \sim 0.3$ at $\delta = 0.4$ [18], which also explains the experimental result of $C^2S = 0.20$

Based on the discussion above, the $1/2^+$ intruder state at 4.83 MeV is a signature of a deformed field and indicates the importance of a deformation in this nuclei.

Recently the excited states of ^{13}B were studied with a method of antisymmetrized molecular dynamics (AMD) [66]. A proton intruder state having the spin and parity of $1/2^+$ were predicted as the first $1/2^+$ state and found to be largely deformed ($\beta \sim 0.7$) state. Although the excitation energy of $\sim$8 MeV is larger than the experimental result the proton intruder configuration and the deformation of the state explain the present result.

Chapter 6

Conclusion

The in-beam γ-ray spectroscopy of neutron-rich unstable nucleus ^{13}B was performed with the proton transfer reaction on the ^{12}Be in order to investigate proton single-particle states in ^{13}B nucleus. The new γ-ray detector array GRAPE was developed to perform the high-resolution in-beam γ-ray spectroscopy. The typical energy resolution was 1.3% (FWHM) for the Doppler-shift corrected γ rays emitted from the fast-moving ($\beta \sim 0.3$) ^{12}Be. The corresponding position resolution was less than 10 mm (FWHM). The experiment was performed at RIPS course in RIKEN. The secondary beam of ^{12}Be was produced and selected from the fragments of the ^{18}O beam particles bombarding the ^{9}Be target. The ^{12}Be beam bombarded the thick liquid helium target of 143 mg/cm^2. The incident and outgoing particles were measured with two plastic scintillation counters and plastic scintillator hodoscope, respectively. They were identified on an event-by-event basis by using $TOF - \Delta E$ and $TOF - \Delta E - E$ method, respectively.

The γ decay of the 4.83-MeV excited state to the ground state was observed. The spin and parity of $1/2^+$ has been uniquely assigned for this state by DWBA analysis of the angular differential cross section for the first time. The spectroscopic strength has been $0.20 \pm 0.02(stat.) \pm 0.10(syst.)$. The other γ decays of the 3.68-, 3.73-, and 4.13-MeV excited states were also observed. The transferred angular momenta for these excited state cannot be uniquely determined. The comparison among the present and previous works, however, gives the qualitative information and possible spin assignments. The $3/2^-$-assignment for the 4.13-MeV excited state has been suggested based on the comparison with the present reaction and two neutron transfer reaction, considering the configuration of this state. The spin of 1/2, however, has been also a candidate for this state. The $1/2^-$-assignment for the 3.73-MeV excited state has been suggested based on its negative parity, considering the strong population and configuration of this state. The spin of 3/2, however, is also a candidate for this state. The possible assignment of $(1/2, 3/2, 5/2)^+$ has been given for the 3.68-MeV excited state.

The comparison with a shell model calculation using OXBASH has been performed.

There are four $1/2^+$ states predicted, however, none of them can explain the observed $1/2^+$ state from the point of view of the excitation energies and/or spectroscopic strengths. The effect of the deformed mean field was qualitatively examined considering a deformed potential provided by the deformed core of ^{12}Be. The spin and parity of $1/2^+$ is characterized by the asymptotic orbitals of [220]1/2, [211]1/2, and [202]1/2. The [220]1/2 orbital gains the energy at the large deformation. Its energy is around 7 MeV calculated from a the change of asymptotic single particle orbital energy and effect of the deformation in empirical mass formula. The observed $1/2^+$ state at 4.83-MeV excitation energy is well represented by the configuration of $(\pi[220]1/2)^1 \otimes ^{12}$Be.

For the disappearance of the magic number, there are three theoretical interpretations, such as the tensor force, weakly bound system, and nuclear deformation. From the present study, the importance of nuclear deformation is pointed out especially for the proton intruder state in the neutron-rich nucleus ^{13}B.

We can also investigate the effect of the deformation in '*island of inversion* region. There is a well known deformed nucleus ^{32}Mg. Then ^{33}Al is expected to have a proton intruder state like ^{13}B. In the ^{33}Al case, these will exist negative parity intruder state from pf-shell. In this region, the effects of tensor force and weakly bound nature succeeds to represent the experimental results. The effect of nuclear deformation in these region needs to be studied in order to clarify the relationship among these effect and to expand our knowledge of the nuclear structure in unstable nuclear.

Acknowledgments

I would like to take this opportunity to place on record my sincere thanks to many people without whom this thesis would not have been at all possible.

I would like to express my sincere gratitude to my thesis adviser Prof. S. Shimoura, for his continuous encouragement and supports through my research career. He has given me good opportunities to study the structure of unstable nuclei using proton transfer reactions but also many experimental nuclear physics. I have learned from him not only knowledge of nuclear physics but also attitudes to solve scientific problems. I am deeply grateful to my supervisor Prof. T. Murakami for his encouragement and helpful discussion. I would like to thank to Prof. K. Imai for his guidance to the field of nuclear physics and for his encouragement and proofreading of this thesis.

I would address my thanks to all the member of R337n-1 collaboration: Prof. S. Shimoura, Dr. H. Iwasaki, Dr. M. Kurokawa, Dr. S. Michimasa, Dr. N. Aoi., Dr. H. Baba, Mr. K. Demichi, Prof. Z. Elekes, Dr. T. Fukuchi, Dr. T. Gomi, Dr. S. Kanno, Prof. S. Kubono, Prof. K. Kurita, Mr. H. Hasegawa, Prof. E. Ideguchi, Prof. N. Iwasa, Mr. Y.U. Matsuyama, Dr. K.L. Yurkewicz, Dr. T. Minemura, Prof. T. Motobayashi, Prof. T. Murakami, Dr. M. Notani, Prof. A. Odahara, Dr. A. Saito, Prof. H. Sakurai, Dr. E. Takeshita, Dr. S. Takeuchi, Mr. M. Tamaki, Prof. T. Teranishi, Dr. Y. Yanagisawa, Dr. K. Yamada, and Prof. M. Ishihara for their great contributions and collaborations to complete this work, successfully. I am also grateful to the staff member of RIKEN Ring Cyclotron for their operation of the accelerator during the experiment. I would like to appreciate variable discussion for theoretical calculations with Prof. T. Suzuki and Prof. Y. Kanada-En'yo. I thank to Dr. S. Bishop for the proofreading of the published paper and to Mr. D. Kahl for the proofreading of this thesis.

I would like to thank Dr. Y. Fukao, Dr. K. Miwa, Mr. T. Nakura, Dr. H. Okada, Dr. S. Terashima, and Dr. M. Togawa. I spent my fruitful and enjoyable time with them in my graduate school days in Kyoto. I also express my thanks to Prof. N. Saito, Prof. N. Nakamura, Prof. H. Funahashi, and Prof. M. Yosoi, for their guidance.

I spent much time in Center for Nuclear Study, University of Tokyo, in my graduate school days. I would like to appreciate fruitful discussions and enjoyable talks, singing, playing softballs, and drinking with all the researchers and students in CNS. I would like to

thank Prof. T. Kawabata, Dr. H. Baba, Dr. S. Michimasa, Dr. A. Saito, Dr. Y. Wakabayashi, Dr. F. Kajihara, Dr. K. Nakanishi, Dr. M. Niikura, and Dr. T. Gunji for many fuitful discussion and advices. I am also grateful to secretaries of CNS, Ms. M. Hirano, Ms. I. Yamamoto, Ms. Y. Endo, Ms. Y. Kishi, Ms. K. Takeuchi, Ms. Y. Otsu, Ms. Y. Sohma, Ms. Y. Fujiwara, Ms. M. Yamaguchi and Ms. N. Teranishi for their kind help for my research life.

I would like to express my grate thanks to my parents, brother, sister, grand mothers (one passed away in December, 2008) for their continuous encouragements, patience and supports.

Finaly, I would like to address my heartfelt acknowledgment to Miwa for her cheering and respect on my studies and life.

References

[1] W.M. Elsasser, J. Phys. Radium **5**, 635–639 (1934).

[2] Maria Goeppert Mayer, Phys. Rev. **75**, 1969–1970 (1949).

[3] Maria Goeppert Mayer, Phys. Rev. **78**, 22–23 (1950).

[4] Maria Goeppert Mayer, Phys. Rev. **78**, 16–21 (1950).

[5] Otto Haxel, J. Hans D. Jensen, and Hans E. Suess, Phys. Rev. **75**, 1766 (1949).

[6] A. Bohr and B.R. Mottelson, Mat. Fys. Medd. Dan. Vid. Selsk. **27**, 1 (1953).

[7] H. Iwasaki, T. Motobayashi, H. Akiyoshi, Y.Ando, N. Fukuda, H. Fujiwara, Zs. Fülöp, K. I. Hahn, Y. Higurashi, M. Hirai, I. Hisanaga, N. Iwasa, T. Kijima, A. Mengoni, T. Minemura, T. Nakamura, M. Notani, S. Ozawa, H. Sagawa, H. Sakurai, S. Shimoura, S. Takeuchi, T. Teranishi, Y. Yanagisawa, and M. Ishihara, Phys. Lett. **B481**, 7–13 (2000).

[8] S. Shimoura, A. Saito, T. Minemura, H. Baba, H. Akiyoshi, N. Aoi, T. Gomi, Y. Higurashi, K. Ieki, N. Imai, N. Iwasa, H. Iwasaki, S. Kanno, S. Kubono, M. Kunibu, S. Michimasa, T. Motobayashi, T. Nakamura, H. Sakurai, M. Serata, E. Takeshita, S. Takeuchi, T. Teranishi, K. Ue, K. Yamada, Y. Yanagisawa, M. Ishihara, and N. Itagaki, Phys. Lett. **B 560**, 31 (2003).

[9] S. Shimoura, S. Ota, K. Demichi, N. Aoi, H. Baba, Z. Elekes, T. Fukuchi, T. Gomi, K. Hasegawa, E. Ideguchi, M. Ishihara, N. Iwasa, H. Iwasaki, S. Kanno, K. Kurita, M. Kurokawa, Y.U. Matsuyama, S. Michimasa, K. Miller, T. Minemura, T. Motobayashi, T. Murakami, M. Notani, A. Odahara, A. Saito, H. Sakurai, E. Takeshita, S. Takeuchi, M. Tamaki, T. Teranishi, K. Yamada, Y. Yanagisawa, and I. Hamamoto, Phys. Lett. **B 654**, 87–91 (2007).

[10] Y. Kanada-En'yo and H. Horiuchi, Phys. Rev. C **68**, 014319 (2003).

[11] D. Guillemaud-Mueller, C. Detraz, M. Langevin, F. Naulin, M. de Saint-Simon, C. Thibault, F. Touchard, and M. Epherre, Nucl. Phys. A **426**, 37–76 (1984).

[12] T. Motobayashi, Y. Ikeda, K. Ieki, M. Inoue, N. Iwasa, T. Kikuchi, M. Kurokawa, S. Moriya, S. Ogawa, H. Murakami, S. Shimoura, Y. Yanagisawa, T. Nakamura, Y. Watanabe, M. Ishihara, T. Teranishi, H. Okuno, and R.F. Casten, Phys. Lett. B **346**, 9–14 (1995).

[13] D.H. Wilkinson and D.E. Alburger, Phys. Rev. **113**, 563 (1959).

[14] H. Iwasaki, T. Motobayashi, H. Akiyoshi, Y.Ando, N. Fukuda, H. Fujiwara, Zs. Fülöp, K. I. Hahn, Y. Higurashi, M. Hirai, I. Hisanaga, N. Iwasa, T. Kijima, A. Mengoni, T. Minemura, T. Nakamura, M. Notani, S. Ozawa, H. Sagawa, H. Sakurai, S. Shimoura, S. Takeuchi, T. Teranishi, Y. Yanagisawa, and M. Ishihara, Phys. Lett. **B491**, 8–14 (2000).

[15] Toshio Suzuki, Rintaro Fujimoto, and Takaharu Otsuka, Phys. Rev. **C 67**, 044302 (2003).

[16] T. Otsuka, T. Suzuki, R. Fujimoto, H. Grawe, and Y. Akaishi, Phys. Rev. Lett. **95**, 232502 (2005).

[17] I. Hamamoto, Nucl. Phys. A **731**, 211 (2004).

[18] A. Bohr and B. R. Mottelson. *Nuclear Structure*. World Scientific, (1998).

[19] I. Hamamoto and S. Shimoura, J. Phys. G: Nucl. Part. Phys. **34**, 2715 (2007).

[20] S. T. Butler, Phys. Rev. **80**, 1095–1096 (1950).

[21] S. T. Butler, Proc. Roy. Soc. A **208**, 559–579 (1951).

[22] H. A. Bethe and S. T. Butler, Phys. Rev. **85**, 1045–1046 (1952).

[23] J.R. Holt and T.N. Marsham, Proc. Phys. Soc. A **66**, 249–257 (1953).

[24] J.R. Holt and T.N. Marsham, Proc. Phys. Soc. A **66**, 467–476 (1953).

[25] J.R. Holt and T.N. Marsham, Proc. Phys. Soc. A **66**, 565–571 (1953).

[26] JR Holt and TN Marsham, Proc. Phys. Soc. A **66**, 258–267 (1953).

[27] J.R. Holt and T.N. Marsham, Proc. Phys. Soc. A **66**, 1032–1040 (1953).

[28] J. Horowitz and A. M. L. Messiah, Phys. Rev. **92**, 1326–1327 (1953).

[29] S. Fernbach, R. Serber, and T. B. Taylor, Phys. Rev. **75**, 1352–1355 (1949).

[30] M. H. Macfarlane and J. B. French, Rev. Mod. Phys. **32**, 567–691 (1960).

[31] P.G. Hansen and J.A. Tostevin, Annual Reviews in Nuclear and Particle Science **53**, 219–261 (2003).

[32] K. E. Rehm, F. Borasi, C. L. Jiang, D. Ackermann, I. Ahmad, B. A. Brown, F. Brumwell, C. N. Davids, P. Decrock, S. M. Fischer, J. Görres, J. Greene, G. Hackmann, B. Harss, D. Henderson, W. Henning, R. V. F. Janssens, G. McMichael, V. Nanal, D. Nisius, J. Nolen, R. C. Pardo, M. Paul, P. Reiter, J. P. Schiffer, D. Seweryniak, and R. E. Segel, Phys. Rev. Lett. **80**, 676–679 (1998).

[33] J.S. Thomas, D.W. Bardayan, J.C. Blackmon, J.A. Cizewski, U. Greife, C.J. Gross, M.S. Johnson, K.L. Jones, R.L. Kozub, J.F. Liang, et al., Phys. Rev. C **71**, 21302 (2005).

[34] S. Michimasa, S. Shimoura, H. Iwasaki, M. Tamaki, S. Ota, N. Aoi, H. Baba, N. Iwasa, S. Kanno, S. Kubono, K Kurita, M Kurokawa, T Minemura, T Motobayashi, M Notani, H.J. Ong, A Saito, H Sakurai, E Takeshita, S Takeuchi, Y Yanagisawa, and A Yoshida, Phys. Lett. B **638**, 146–152 (2006).

[35] A. Bonaccorso and D. M. Brink, Phys. Rev. C **46**, 700–706 (1992).

[36] D.M. Brink, Phys. Lett. B **40**, 37–40 (1972).

[37] H. de Vries, C.W. de!Jager, and C de Vries, Atomic Data and Nuclear Data Tables **36**, 495 (1987).

[38] A. Marques, A.J.P.L. Policarpo, and W.R. Phillips, Nucl. Phys. **36**, 45–55 (1962).

[39] K.W. Jones, W.R. Harris, M.T. McEllistrem, and D.E. Alburger, Phys. Rev. **186**, 978–983 (1969).

[40] E. Norbeck, Jr, Phys. Rev. **105**, 204–209 (1957).

[41] R. R. Carlson and E. Norbeck, Phys. Rev. **131**, 1204–1211 (1963).

[42] R. MIDDLETON and D.J. PULLEN, Nucl. Phys. **51**, 50–62 (1964).

[43] F. Ajzenberg-Selove, E. R. Flynn, and Ole Hansen, Phys. Rev. **C 17**, 1283–1293 (1978).

[44] V. Guimarães, J. J. Kolata, D. Bazin, B. Blank, B. A. Brown, T. Glasmacher, P. G. Hansen, R. W. Ibbotson, D. Karnes, V. Maddalena, A. Navin, B. Pritychenko, B. M. Sherrill, D. P. Balamuth, and J. E. Bush, Phys. Rev. **C 61**, 064609 (2000).

[45] N. Aoi, K. Yoneda, H. Miyatake, H. Ogawa, Y. Yamamoto, E. Ideguchi, T. Kishida, T. Nakamura, M. Notani, H. Sakurai, T. Teranishi, H. Wu, S. S. Yamamoto, Y. Watanabe, A. Yoshida, and M. Ishihara, Z. Phys. **A 358**, 253–255 (1997).

[46] N. Aoi, K. Yoneda, E. Ideguchi, T. Kishida, T. Nakamura, M. Notani, H. Sakurai, T. Teranishi, Y. Watanabe, H. Wu, A. Yoshida, H. Miyatake, Y. Yamamoto, H. Ogawa, S. S. Yamamoto, and M. Ishihara, Phys. Rev. C **66**, 014301 (2002).

[47] R.L. Williams, Jr and L. Madansky, Phys. Rev. C **3**, 2149–2150 (1971).

[48] T. Nagatomo et al., Nucl. Phys. **A 746**, 505c (2004).

[49] T. Nagatomo, K. Matsuta, K. Akutsu, T. Iwakoshi, Y. Nakashima, T. Sumikama, M. Ogura, M. Mihara, H. Fujiwara, S. Kumashiro, et al., Nucl. Phys. A **746**, 509–512 (2004).

[50] R. Kalpakchieva, H.G. Bohlen, W. von Oertzen, B. Gebauer, M. von Lucke-Petsch, T. N. Massey, A. N. Ostrowski, Th. Stolla, M. Wilpert, and Th. Wilpert, Eur. Phys. J. **A 7**, 451–461 (2000).

[51] M.J. Throop, Phys. Rev. **179**, 1101–1033 (1969).

[52] H. Sagawa and K. Asahi, Phys. Rev. **C 63**, 064310 (2001).

[53] H. T. Fortune and R. Sherr, Phys. Rev. **C 68**, 024301 (2003).

[54] H. Ryuto et al., Nucl. Instr. and Meth. **A 555**, 1 (2005).

[55] H. Kumagai, A. Ozawa, N. Fukuda, K. Sümmerer, and I. Tanihata, Nucl. Instrum. Meth. **A470**, 562–570 (2001).

[56] S. Shimoura, Nucl. Instrum. Meth. **A525**, 188–192 (2004).

[57] M. Kurokawa et al., IEEE TRANSACTIONS ON NUCLEAR SCIENCE **50**, 1309 (2003).

[58] T. Kubo, M. Ishihara, N. Inabe, H. Kumagai, I. Tanihata, K. Yoshida, T. Nakamura, H. Okuno, S. Shimoura, and K. Asahi, Nucl. Instrum. Meth. B **70**, 309–319 (1992).

[59] W. R. Leo. *Techniques for Nuclear and Particle Physics Experiments*. Springer Verlag, (1987).

[60] A. Ingemarsson, J. Nyberg, P. U. Renberga, O. Sundberg, R. F. Carlson, A. J. Cox, A. Auce, R. Johansson, G. Tibell, Dao T. Khoa, and R. E. Warnere, Nucl. Phys. **A676**, 3–31 (2000).

[61] A. Ingemarsson, G. J. Arendsec, A. Auce, R. F. Carlson, A. A. Cowley, A. J. Cox, S. V. Förtsche, R. Johansson, B. R. Karlson, M. Lantz, J. Peavy, J. A. Stander, G. F. Steyn, and G. Tibell, Nucl. Phys. **A696**, 3–30 (2001).

[62] G.R. Satchler and W.G. Love, Phys. Rep. **55**, 183–254 (1979).

[63] G. R. Satchler and Dao T. Khoa, Phys. Rev. C **55**, 285–297 (1997).

[64] NNDC. http://www.nndc.bnl.gov/.

[65] B. A. Brown, A. Etchegoyen, and W. D. M. Rae, MSU-NSCL report **524**, (1986).

[66] Y. Kanada-En'yo, Y. Kawanami, Y. Taniguchi, and K. Kimura, Prog. Theor. Phys. (Kyoto) **120**, 917–935 (2008).

Appendix A

Data Table of Angular Differential Cross Section

θ_{CM} (deg.)	$d\sigma/d\Omega$ (mb/sr)	error (mb/sr)
1.36	6.98	1.13
3.16	7.07	0.63
5.15	4.84	0.42
7.17	2.83	0.29
9.20	2.28	0.22
11.2	1.77	0.18
13.3	1.38	0.14
15.3	0.793	0.105
17.4	0.529	0.078
19.4	0.282	0.059
21.6	0.131	0.040
23.6	0.108	0.032

Table A.1: Data table of angular differential cross section for 4.83-MeV excited state.

Appendix B

Comparison between analog and digital sum of GRAPE

We used the analog sum for deducing the γ-ray energy in this thesis. In this chapter, we compare the properties of analog and digital sum. Before going into details, we remember the definition of the analog and digital sum. Those of a crystal are obtained using the equations below,

$$E_a = E_\Sigma \frac{\sum_i E_i}{\sum_i \epsilon'_i E_i}, \tag{B.1}$$

$$E_d = \sum_i E_i, \tag{B.2}$$

where, $E_{a(d)}$ is the analog (digital) sum, E_i is a measured energy in segment i, and ϵ'_i is a gain correction factor (see Sec. 3.5.1). In the analysis, the threshold at 80 keV has been set for all the segments so as to align the thresholds among them. Although the energy deposition below 80 keV is not included in the digital sum, it is included in the analog sum since the add-back is performed before the digitization. The correction factor for E_Σ in Eq. (B.1) is not exactly correct, however, the effect is small, especially when the total energy deposition is large. Then the full-energy peak efficiency of the analog sum is larger than that of the digital sum. Figure B.1(a) shows the comparison of the full-energy peak efficiencies between the analog and digital sum. The data of the analog and digital sum are shown by (red) open circle and (blue) crosses, respectively. The efficiencies of the analog sum is 20% larger than those of the digital sum.

On the other hand the energy resolution of the analog sum is worse than that of the digital sum, since the noise of each segment is coherently added when the noise is in-phase. Figure B.1(b) shows the comparison of the energy resolutions between the analog and digital sum, which are shown by (red) open circles and (blue) crosses, respectively. The resolution of the digital sum strongly depends on the γ-ray energy due to the deviation of the energy calibration.

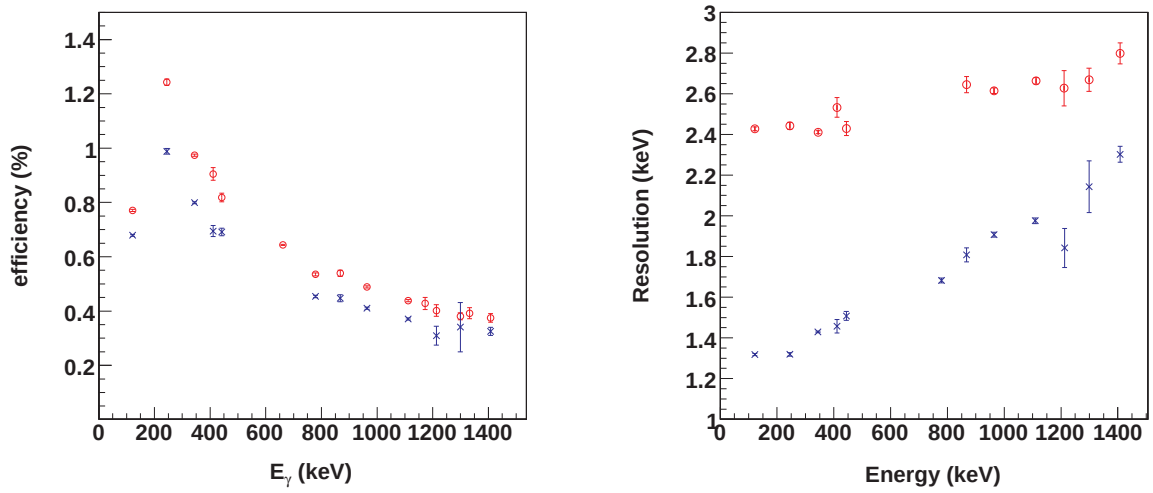

(a) efficiencies

(a) energy resolutions (1σ)

Figure B.1: Comparison between the analog and digital sum. The data of the analog and digital sum are shown by (red) open circles and (blue) crosses, respectively. (a) Comparison of the full-energy peak efficiencies. (b) Comparison of the energy resolution (one standard deviation).

Appendix C

Tailing function of Full Energy Peak in Germanium Detector

A treatment of the γ-ray energy obtained by the simulation is described. Figure C.1(a) shows the measured response function (black histogram) and fitted response functions taken with ^{60}Co standard source. In the measured response function, the tail at the low energy side of each full-energy peak is observed. Such tails are not found in the original simulated response function (blue lines), which causes an overestimation of the full-energy peak efficiencies since the response functions are not fitted correctly. Therefore, we need to modify the simulated response functions.

The modification has been performed by using a probability distribution described below.

$$P(E) \propto \exp\left[\alpha \frac{(E_c - E_0)}{E_0}\right] \quad (E \leq E_0), \tag{C.1}$$

where E_0 is a energy deposition of γ ray obtained by the simulation, E_c is the modified energy deposition, and α is a constant determined by fitting the modified response function to the experimental one. The E_c is randomly generated from the probability distribution $P(E)$ in the range from 0. to E_0. This modification is applied to a certain fraction ϵ of the events. Figure C.1(b) shows a energy spectrum obtained by the modification of the energy spectrum in Fig. C.1(a), where $\alpha = 2.094$[1] and $\epsilon = 5.900 \times 10^2$ are used. These parameters are obtained by fitting a modified response function to the experimental one for the γ-ray energy spectrum of ^{137}Cs standard source. The modified responses function reproduce the experimental one for ^{60}Co standard source well.

The probability function is obtained assuming the insufficient collection of the charge in a germanium crystal. A probability that charge Q is collected at a given timing t, is assumed to be an exponential function as:

$$P(t) \propto \exp\left(-\frac{t}{\tau}\right), \tag{C.2}$$

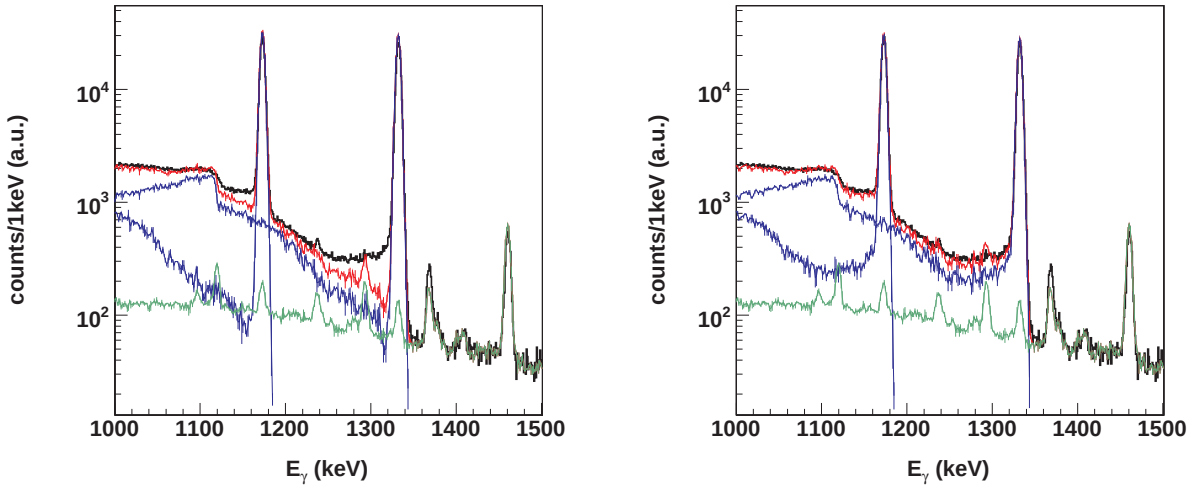

(a) before modification (b) after modification

Figure C.1: Demonstration of the treatment of the tailing. The energy spectrum for the ^{60}Co is fitted with two types of simulated response functions (blue lines); before (a) and after (b) modification for the tailing. The green lines show the response function for the background γ rays.

where τ is a time constant. An average time of the charge collection $\bar{t}$ for the charge Q is obtained as below,

$$\bar{t} = \frac{Q}{v_Q}, \tag{C.3}$$

where v_Q is an average velocity of the charge collection. The velocity is approximated to be Q_0/T_Q for the induced charge Q_0 with an average collection time T_Q for Q_0. Now, since v_Q is assumed to be constant for a given charge Q_0, the probability of the charge collection obeys Eq. (3.28) by replacing t by $\bar{t} = Q/v_Q$. Then we obtained the probability distribution of the collected charge Q_c as below,

$$P(Q) \propto \exp\left[-\frac{T_Q}{\tau} \cdot \frac{Q_0 - Q_c}{Q_0}\right]. \tag{C.4}$$

Since the charges Q_0 and Q_c is proportional to the energy E_0 and E_c, respectively, we obtain Eq. (3.33) by defining $\alpha \equiv T_Q/\tau$. Eq.